

CHIRAL RECOGNITION AND SUPRAMOLECULAR SELF-ASSEMBLY OF ADSORBED AMINO ACIDS AND DIPEPTIDES AT THE SUBMOLECULAR LEVEL

THÈSE N° 3920 (2007)

PRÉSENTÉE LE 13 DÉCEMBRE 2007

À LA FACULTÉ DES SCIENCES DE BASE

LABORATOIRE DE SCIENCE À L'ÉCHELLE NANOMÉTRIQUE

PROGRAMME DOCTORAL EN PHYSIQUE

ÉCOLE POLYTECHNIQUE FÉDÉRALE DE LAUSANNE

POUR L'OBTENTION DU GRADE DE DOCTEUR ÈS SCIENCES

PAR

Magalí LINGENFELDER

Licenciada en Química, Universidad Nacional de Córdoba, Argentine
et de nationalité argentine

acceptée sur proposition du jury:

Prof. R. Schaller, président du jury

Prof. K. Kern, directeur de thèse

Prof. J. I. Pascual, rapporteur

Prof. H. Vogel, rapporteur

Prof. H. Zandvliet, rapporteur



ÉCOLE POLYTECHNIQUE
FÉDÉRALE DE LAUSANNE

Suisse
2008

And Alice had jumped lightly down into the Looking glass room...

Lewis Carrol, 1872.



*Yo que sentí el horror de los espejos
no sólo ante el cristal impenetrable
donde acaba y empieza, inhabitable,
un imposible espacio de reflejos.*

*Sino ante el agua especular que imita
el otro azul en su profundo cielo
que a veces raya el ilusorio vuelo
del ave inversa o que un temblor agita.*

*Y ante la superficie silenciosa
del ébano sutil cuya tersura
repite como un sueño la blancura
de un vago mármol o una vaga rosa.*

*Hoy, al cabo de tantos y perplejos
años de errar bajo la varia luna,
me pregunto qué azar de la fortuna
hizo que yo temiera los espejos.*

*Espejos de metal, enmascarado
espejo de caoba que en la bruma
de su rojo crepúsculo disfuma
ese rostro que mira y es mirado.*

*Infinitos los veo, elementales
ejecutores de un antiguo pacto,
multiplicar el mundo como el acto
generativo, insomnes y fatales.*

*Prolonga este vano mundo incierto
en su vertiginosa telaraña;
a veces en la tarde los empaña
el hálito de un hombre que no ha muerto.*

*Nos acecha el cristal. Si entre las cuatro
paredes de la alcoba hay un espejo,
ya no estoy solo. Hay otro. Hay el reflejo
que arma en el alba un sigiloso teatro.*

*Todo acontece y nada se recuerda
en esos gabinetes cristalinos
donde, como fantásticos rabinos,
leemos los libros de derecha a izquierda.*

*Claudio, rey de una tarde, rey soñado,
no sintió que era un sueño hasta aquel día
en que un actor mimó su felonía
con arte silencioso, en un tablado.*

*Que haya sueños es raro, que haya espejos,
que el usual y gastado repertorio
de cada día incluya el ilusorio
orbe profundo que urden los reflejos.*

*Dios (he dado en pensar) pone un empeño
en toda esa inasible arquitectura
que edifica la luz con la tersura
del cristal y la sombra con el sueño.*

*Dios ha creado las noches que se arman
de sueños y las formas del espejo
para que el hombre sienta que es reflejo
y vanidad. Por eso nos alarman.*

Los Espejos, Jorge Luis Borges.

Abstract

This thesis deals with the supramolecular organization of chiral aminoacids and dipeptides on metal surfaces. The emergence of homochirality in biomolecular systems is one of the most intriguing open questions of Nature. The self-assembly and amplification of chiral subunits into higher-order species is crucial in understanding the development of homochirality in biological function. Apart from being related to the very first organic molecules synthesized on earth, understanding the basics of chiral recognition and discrimination is of high technological relevance. In fact, the chemistry and technology of production and separation of enantiomers has evolved into a branch of materials science under the name of *Chirotechnology*.

Even before the concept of *molecule* existed, Pasteur pointed out that the asymmetry of the crystals of tartaric acid he observed was related to the asymmetry of the *components* of which they were made. Nowadays, we can assess the landscape of these *components* even at the submolecular level by means of Scanning Tunneling Microscopy (STM).

The aim of this thesis is twofold: primary to get an insight into the fundamental aspects of chiral recognition, under the main inspiring question: How does chiral recognition take place at the single molecule level? and secondly: How can we tune the expression of chirality on a metal surface to achieve global templation?

The first part of this thesis presents a comprehensive study of the basic requirements for amino acid chiral templation of metal surfaces. By comparatively studying the adsorption behaviour of L-Phenylalanine (L-Phe) and L-Tyrosine (L-Tyr) on Cu(110) we show that conformational rigidity is a key parameter for the expression of footprint homochirality on metal surfaces. This parameter can be tuned by the appropriate choice of the amino acid residue. The molecular structure of the adsorbed molecules is studied by a combination of reflection absorption infrared spectroscopy (RAIRS), STM and molecular dynamics simulations (MD).

The second part of the thesis focuses on the transfer of molecular chirality to supramolecular structures of Di-Phenylalanine (Phe-Phe) on Cu(110). We have followed the chiral recognition and discrimination among individual Phe-Phe enantiomers by STM and rationalized it using first principles and classical molecular dynamics simulations. The geometrical parameters of the final supramolecular structures are studied

by near edge absorption fine structure (NEXAFS). Our results show that molecules whose static structure is not optimized for specific binding can selectively recognize each other and link through mutually induced conformational changes. The general idea of induced molecular fit in biomolecular recognition was introduced by Linus Pauling more than 50 years ago. We now report direct evidence of this dynamic scenario at the single molecule level.

The last part of this thesis deals with the adsorption phase diagram of Phe-Phe on Cu(110). The encountered adsorption motifs and the chemical processes involved in the phase transitions are investigated by a combination of STM, X-ray photoelectron spectroscopy (XPS), low energy electron diffraction (LEED) and thermal programme desorption (TPD). The resulting supramolecular assemblies expose chiral cavities that can potentially be used as enantioselective adsorption sites.

Keywords: Chirality, Molecular Recognition, Self-assembly, Scanning Tunneling Microscopy, Amino Acids, Peptides

Version abrégée

Cette thèse traite de l'organisation supramoléculaire d'acides aminés et dipeptides chiraux sur des surfaces métalliques. L'émergence de l'homochiralité dans les systèmes biomoléculaires reste l'une des questions de la nature les plus intrigantes et encore non résolue. L'auto-assemblage et l'amplification des sous-unités chirales en espèces d'ordre supérieur sont cruciaux pour la compréhension du développement de l'homochiralité dans les fonctions biologiques. Outre la relation aux toutes premières molécules organiques synthétisées sur Terre, la compréhension des fondements de la reconnaissance et de la discrimination chirales est d'un haut intérêt technologique. La chimie et la technologie de la production et de la séparation des énantiomères se sont développées en une branche de la science des matériaux sous le nom de chirotechnologie.

Avant même que le concept de « molécule » n'existe, Pasteur avait déjà noté que l'asymétrie des cristaux d'acide tartrique était liée à l'asymétrie des « composants » dont ils sont formés. Aujourd'hui, il est possible d'établir le paysage de ces « composants » à l'échelle submoléculaire au moyen du microscope à effet tunnel (STM).

L'objectif de cette thèse est double : premièrement obtenir une idée des aspects fondamentaux de la reconnaissance chirale, à l'aune de l'idée directrice : comment la reconnaissance chirale prend-elle place au niveau de la molécule unique? et deuxièmement : comment peut-on ajuster l'expression de la chiralité sur une surface métallique afin d'obtenir un ordonnancement global?

La première partie de cette thèse présente une étude complète des conditions requises pour l'ordonnancement d'acides aminés chiraux sur des surfaces métalliques. En étudiant par comparaison l'adsorption de la L-Phénylalanine (L-Phe) et la L-Tyrosine (L-Tyr) sur Cu(110), nous avons montré que la rigidité de conformation est le paramètre clé pour l'expression d'une empreinte d'homochiralité sur les surfaces métalliques. Ce paramètre peut être ajusté par le choix approprié d'un résidu aminoacide. La structure moléculaire des molécules adsorbées est étudiée par la combinaison de mesures RAIRS et STM, et de simulations moléculaires dynamiques.

La deuxième partie de cette thèse se concentre sur le transfert de la chiralité moléculaire aux structures supramoléculaires de di-phénylalanine. Nous avons suivi la reconnaissance et la discrimination chirales parmi des énantiomères individuels de di-phénylalanine par STM et nous avons justifié ce comportement en utilisant des cal-

culs quantiques ab-initio et des simulations de dynamique moléculaire classique. Les paramètres géométriques des structures supramoléculaires finales ont été étudiés par NEXAFS. Nos résultats montrent que les molécules dont la structure statique n'est pas optimisée pour une liaison spécifique peuvent se reconnaître sélectivement entre elles et se lier grâce à des changements de conformation induits mutuellement. L'idée générale d'ajustement moléculaire induit dans la reconnaissance biomoléculaire fut introduite par Linus Pauling il y a plus de cinquante ans. Nous apportons maintenant la preuve directe de ce scénario dynamique au niveau de la molécule individuelle.

La dernière partie de cette thèse dresse le diagramme de phase d'adsorption de la Diphénylalanine sur Cu(110). Les motifs d'adsorption trouvés et les processus chimiques impliqués dans les transitions de phase sont étudiés par la combinaison de mesures STM, LEED, TPD et XPS. Les assemblages supramoléculaires résultants montrent des cavités chirales qui peuvent être potentiellement utilisées comme site d'adsorption énantio-sélectif.

Mots-clés : Chiralité, Reconnaissance moléculaire, Auto-assemblage, Microscope à effet tunnel, Aminoacides, Peptides

Contents

Abstract	i
Version abrégée	iii
1 Introduction	1
1.1 Through the looking glass	1
2 Experimental and Theoretical Methods	5
2.1 STM	6
2.1.1 The basic principle of STM	6
2.1.2 The theory of STM	8
2.2 Complementary techniques	12
2.2.1 X-ray Absorption Techniques	12
2.2.2 TPD	16
2.2.3 RAIRS	17
2.2.4 LEED	19
2.2.5 Theoretical simulations	20
2.3 Experimental setup	22
2.3.1 The STM system	22
2.3.2 Sample preparation	25
2.3.3 Molecular deposition	25
3 Supramolecular Organization of Amino acids on Cu(110)	27
3.1 Sample Preparation	29

3.2	Reflection-Absorption Infrared Spectroscopy measurements	29
3.3	STM measurements and footprint chirality	37
4	On the Mechanism of Chiral Recognition	45
4.1	The molecule-substrate system	46
4.2	Integrated Experimental and Theoretical analysis	47
4.2.1	STM measurements	47
4.2.2	Computational methods	48
4.2.3	Stereoselectivity	57
4.2.4	Further growth of the supramolecular chains	60
4.3	Discussion	60
5	Adsorption Phase Diagram of Phe-Phe on Cu (110)	67
5.1	L-Phe-L-Phe deposition at low substrate temperatures	69
5.1.1	C and S pairs at 90-290K	69
5.2	Phe-Phe deposition at high substrate temperatures	71
5.2.1	Phase I: 315-360K	71
5.2.2	Phase II: 400K	75
5.2.3	Phase III: 450K	81
5.3	Conclusions	84
	Abbreviations and Common Symbols	87
	Bibliography	89
	Supporting Information	97
	Publications	99
	Personal Notes	103
	Curriculum vitae	105

Chapter 1

Introduction

1.1 Through the looking glass

Most of the molecules that mediate the processes of life like enzymes, hormones, antibodies and receptors are chiral. That means, they present exactly the same chemical formula and atomic connectivity but their atomic arrangement in space exists in two mirror-image forms (enantiomers) that cannot be superimposed.

Probably one of the most exciting mysteries of Nature is why the building blocks of life, i.e. amino acids (that form proteins) are almost exclusively present in the chiral L form and sugars (that constitute DNA) are all in the D form. The origin of this uniform chirality (homochirality) in biology is the subject of much debate. Many scientists believe that current life forms could not exist without the homochirality of these elementary units, because biological processes need the efficiency in recognition that can only be achieved with homochiral substances [1].

From a practical perspective, the importance of molecular chirality arises from the fact that the two mirror images of a chiral molecule can have vastly different physiological impacts when ingested by living organisms [2]. This is particularly important for medicinal chemistry. For example, while one enantiomer of ethambutol is used to treat tuberculosis, the other causes blindness. Even if the enantiomer of a given drug is not dangerous but simply not effective, a patient has to take a double dose of medicine if this is a racemate (a mixture of equal amount of both enantiomers). As a consequence, there is a strong need to produce many chiral compounds as pharmaceuticals and agro-

chemicals in enantiomerically pure form. Catalytic processes used for their synthesis are primarily carried out in homogeneous phase. Such catalysts often contain heavy metal centers, which must be removed from the product prior to use, a problem which is avoided by the use of heterogeneous catalysts [3]. However, a typical drawback of heterogeneous catalysts is that they must be modified to become enantioselective. One common approach is the use of solid surfaces which become enantioselective by the adsorption of organic chiral modifiers. The precise mechanisms by which chiral selectivity is transferred to the substrates are still not known. However, many observations seem to indicate that a major role is played by the formation of ordered supramolecular structures having void spaces which act as enantioselective adsorption sites [4]. In connection with this idea, the adsorption of tartaric acid, amino acids and other chiral organic molecules on metal single-crystal surfaces has recently received particular attention for being an ideal model system [5]. As a first step, many studies have focused on the characterization of the molecular overlayers trying to precisely identify the molecule-surface and molecule-molecule binding motifs [6]. A number of recent experiments came to the conclusion that there is a need for at least two anchoring adsorption points for chiral templation to work [3]. Other reports have shown that the acquired enantiospecificity can be directly probed with a second chiral molecule [5]. For instance, it has been observed that enantiopure propylene oxide prefers to adsorb on Pd(111) [5] surfaces modified by 2-butoxide of the same chirality. However, this research field is still on its infancy and a level of knowledge that would allow rational design of enantiopure covered surfaces for enantioselective catalytic processes is still far to be reached.

A main objective of this thesis has been to investigate the self-assembly mechanisms of amino acids and dipeptides on metal surfaces. Special attention has been given to the process of chiral recognition that leads to supramolecular enantiopure structures. The bonding, ordering and dynamics of these systems are not only relevant for the design of enantioselective catalysts but also for several technological applications that require biological interfaces, as sensors and medical implants [7].

In order to gain atomically resolved morphological information, most of the measurements were performed by Scanning Tunneling Microscopy (STM). These measurements were complemented by a large variety of other experimental and theoretical investigations which allowed us to obtain a very detailed picture of the structural and chemical

properties of the various systems. All these techniques, together with a brief description of the main experimental set-up and sample preparation methods employed in this thesis are introduced in Chapter 2.

STM studies have shown that two main aspects determine the final chirality of molecular adsorbed motifs on metal surfaces: the intrinsic chirality of the adsorbate (molecular chirality) and the chirality of the bonding geometry, i.e. of the positions at which the molecules are binding to the surface (footprint chirality) [6]. For example, it is generally accepted that the amino and carboxylic groups bind preferentially to ‘on top’ sites on Cu surfaces. This preferential binding determines at least two molecule-substrate anchoring points and results in a chiral footprint. But, how does the ‘chiral footprint’ affect the expression of chirality at the global level? How many contact points are needed to express a single ordered supramolecular motif on the surface? What is the role of the conformational flexibility and how can this parameter be tuned by the appropriate choice of the amino acid residue? All these questions are addressed for the study of the amino acids L-Phe and L-Tyr on Cu(110) in Chapter 3 of this thesis.

Apart from the mechanisms responsible for the chirality transfer between molecules and surfaces, a further fundamental issue is represented by the microscopic process that allows an adsorbed molecule to selectively interact only with molecules of the same chirality. In biology the first theoretical efforts to understand the basis of chiral discrimination introduced the recognition picture of the *lock and key* model based on a *three-point interaction* [8], Figure (1.1). In this model, an enzyme or receptor sur-

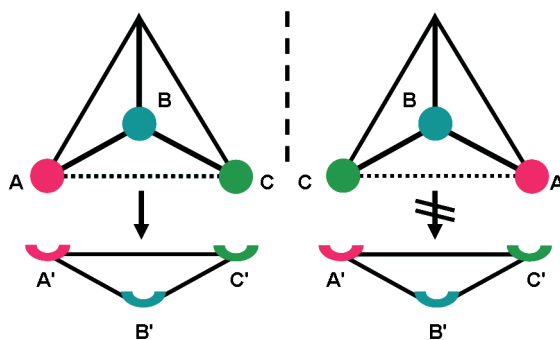


Figure 1.1: Schematic representation of the *three-point interaction* interaction model for chiral recognition proposed by Easson and Stedman [8].

face had to possess three non equivalent binding sites in order to distinguish between

enantiomers. Discrimination occurs when one enantiomer could simultaneously interact with all of the sites while its mirror form could bind only at one. After Ogston used this model to explain the enzymatic decarboxylation of L-Serine to Glycine [9], by the mid-1950's the *three-point interaction* became generally accepted as the source of biological enantioselectivity, spreading quickly to other disciplines. However, more recent theoretical studies [10] have pointed out that dynamic mutual conformational adjustments should also be important in chiral recognition.

Similar model descriptions have been applied for explaining how the chiral information is transferred from the first adsorbed molecule to the supramolecular level. While the static *three-point interaction* was recently used to explain the stereoselective formation of Cysteine superstructures on Au [11], the question of how the molecular conformational flexibility affects the recognition process is still open. In Chapter 4 we analyze adsorbed dipeptides as a model system able to stand internal conformational changes. In particular we investigate the interaction between two di-D-Phenylalanine (D-Phe-D-Phe) molecules and of D-Phe-D-Phe with its enantiomer L-Phe-L-Phe on Cu(110). Our results demonstrate that the stereoselective assembly of adsorbed di-Phenylalanine enantiomers into molecule pairs and chains occurs through mutually induced conformational changes.

Finally, the effect of the adsorption temperature on the creation of enantiopure supramolecular assemblies of L-Phe-L-Phe and D-Phe-D-Phe is studied in Chapter 5. A variety of adsorption motifs are encountered in the 90-600 K temperature range and rationalized via a thorough structural, spectroscopic and theoretical investigation. The results presented in this chapter show that the molecular footprint chirality can be tuned by the adsorption temperature to express only one chiral motif over the entire surface. The resulting ordered supramolecular structures expose chiral cavities that could be potentially used as enantioselective adsorption sites.

Chapter 2

Experimental and Theoretical Methods

To understand the nature of the physical and chemical interactions of the systems discussed in this thesis, a large variety of experimental techniques and theoretical simulation methods have been employed. Local submolecular characterization and insight into the dynamics is obtained by scanning tunneling microscopy (STM). As a complement, the overall geometry is evidenced by low-energy electron diffraction (LEED) that provides a fast overview over structural periodicities and allows to connect the STM measurements acquired in our setup with the data taken at different UHV chambers. Structural information averaged over large surface areas and details on the oxidation state and orientation of the functional groups is obtained by x-ray photoemission spectroscopy (XPS), near edge absorption fine structure (NEXAFS) and reflection adsorption infrared spectroscopy (RAIRS). The thermal chemistry of the adsorbates and the entity of the desorbed products is studied by temperature programmed desorption (TPD). Furthermore, molecular dynamics and density functional theory (DFT) simulations provide an atomistic description of the encountered adsorption motifs. In the present chapter we will mainly discuss the principles and theory of STM, which is the main experimental technique employed in this thesis. Furthermore, a brief description of the complementary techniques is also provided here. Finally, we give an overview of the STM setup and sample preparation procedures.

2.1 STM

"I could not stop looking at the images. It was like entering a new world"

G. Binnig, joint Nobel lecture with H. Rohrer, December 8, 1986.

Since the advent of STM in the early eighties, *using an exsiccator as vacuum chamber and lots of Scotch tape* [12], an atom by atom trip to the geometric and electronic properties of matter has begun. Originally intended by Binnig and Rohrer *for the performance of a local experiment, at a preselected position and on a very small spatial scale down to atomic dimensions* [12, 13], STM has revolutionized the fields of surface and materials science over the past 25 years. Many disputed surface structural models have been resolved by the direct imaging capability of STM. Furthermore, the visualization of dynamic processes in real space has led to unprecedented new insight into, for example, diffusion, reaction, nucleation and growth phenomena on surfaces [14]. Nowadays, STM can even probe single molecules with atomic resolution and reveal their quantum properties [15]. Significantly, the capability of the tunneling probe to operate in liquid and gaseous environments, as well as in vacuum, allows direct analysis of processes at liquid-solid interfaces and of biological structures and processes in vivo [16, 17]. This always more exciting adventure into the nanoworld is bound to continue and the closer look provided by STM, together with the possibility of the tip to induce conformational modifications and reactions, will continue to reveal fundamental properties in the land of atoms and adsorbed molecules.

2.1.1 The basic principle of STM

STM is performed by bringing a sharp conducting tip, typically made of W or PtIr, close ($< 1\text{nm}$) to a conductive sample surface (Figure 2.1). The proximity is such that an overlap between the electron wave functions of the tip and the sample occurs. If a bias voltage V is applied to the sample, a current in the nanoampere range passes between the tip and the sample (or vice versa, depending on the polarity of V) due to electron tunneling through the energy barrier in the vacuum gap region. The tunnel current decreases exponentially as the gap distance increases. Therefore corrugations in a sample surface will give rise to significant current variations as the tip is scanned across the surface [16].

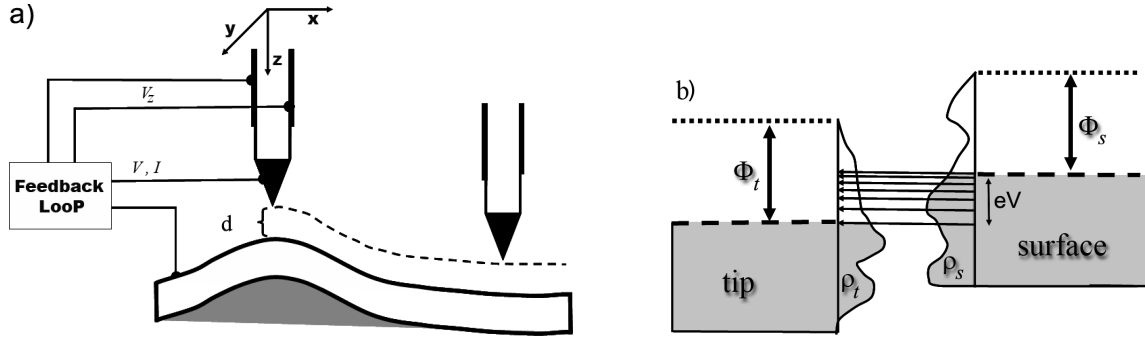


Figure 2.1: STM Tunneling scheme.(a) Schematic illustration of the STM principle, adapted from [12] (b) Corresponding potential energy diagram.

As it is shown in Figure 2.1a the lateral tip position (x and y axes), as well as the tip-sample distance d are controlled by means of voltage signals applied to piezoelectric transducers. A bias of ~ 1 V across a typical piezoelectric element may cause an expansion or contraction of ~ 10 Å so that sub-atomic movement of the tip (with picometer precision) can easily be obtained [16].

All the STM images presented in this thesis are taken in the so-called *constant current mode*, that means a voltage is applied between the tip and the sample and the height of the tip is continuously adjusted to keep the tunnel current constant as the tip is scanned across the surface. This situation is reached by comparing the I at each x - y position with a preset value (I_0), typically 0.5–5 nA [18], in a feedback circuit (Figure 2.1). The feedback signal, proportional to the difference between I and I_0 , provides a correction voltage to the z transducer and thus causes the distance d between the tip and the surface to change when a protrusion is traversed. Recording the feedback signal or z voltage as a function of the lateral tip position during raster scanning yields a map of the surface topography. Since the transmission of electrons through a barrier is exponentially sensitive to the width d , it mainly flows through the few atoms at the very apex of the tip. Thus the tunneling current is highly localized, leading to the atomic-scale resolution of STM. In the case of a negatively biased sample (as in Figure 2.1b) the net current comes from electrons tunneling from occupied states in the sample to unoccupied states of the tip. The current per energy unit, is represented by the density of horizontal arrows in Figure 2.1b. As can be seen it decreases with decreasing energy since the energetically lower lying states decay steeper in the vacuum

barrier region.

2.1.2 The theory of STM

Several tunneling theories are based on the 'perturbative transfer Hamiltonian' formalism introduced by Bardeen in 1961 [19]. Here the interaction between the two electrodes is sufficiently weak to be neglected and the tunnel current can be evaluated from the eigenfunctions ψ_s and ψ_t , with eigenenergies E_s and E_t , of the separate sample and tip electrodes, respectively. In this formalism, the tunnel current is calculated from the overlap of the tails of ψ_s and ψ_t in the region of the tunnel barrier, and the following is obtained:

$$I(V) = \frac{2\pi e}{\hbar} \sum_{s,t} \left(f(E_s) [1 - f(E_t + eV)] |M_{st}|^2 \delta(E_s - E_t) \right), \quad (2.1)$$

here the tunnel matrix element is given by:

$$M_{st} = \frac{\hbar^2}{2m} \int d\mathbf{S} \cdot (\psi_s^* \nabla \psi_t - \psi_t \nabla \psi_s^*) , \quad (2.2)$$

where the integral is over the whole surface \mathbf{S} . The delta function in equation (2.1) implies that the electron does not lose energy during tunneling (elastic tunneling), whereas the Fermi-Dirac function $f(E)$ takes into account that tunneling occurs, for instance, from a filled sample state into an empty tip state. The energy shift eV is the result of the tunnel bias voltage V . For small tunneling voltages (e.g. ~ 10 meV) and low temperatures, eq. (2.1), $f(E)$ can be expanded to obtain:

$$I(V) = \frac{2\pi e^2 V}{\hbar} \sum_{s,t} |M_{st}|^2 \cdot \delta(E_s - E_F) \cdot (E_t - E_F) , \quad (2.3)$$

where we have introduced the Fermi energy E_F . A further simplification is given by the Tersoff-Hamann model [20], where the tip is modeled as a local spherical potential (represented by an s orbital) centered on the tip apex. Tersoff and Hamann (TH) were the first to apply the transfer Hamiltonian approach to STM. The summation over the absolute squares of the wavefunctions together with energy δ functions in (2.3) can be

evaluated to yield the local density of states (LDOS) of the sample ρ_s at the position (x, y) below the tip and the LDOS ρ_t of the tip. This allows to write (2.3) as

$$I(V) \propto \int_0^{eV} \rho_s(E, x, y) \cdot \rho_t(E - eV) \cdot \mathcal{T}(E, V, d) dE, \quad (2.4)$$

where the Fermi level is at $E_F = 0$ V and \mathcal{T} is the transition matrix describing the tunneling probability. Equation (2.4) shows that the tunneling depends on the density of states of the tip at the applied bias voltage V , on the density of states of the surface at the Fermi-level, and on the transition matrix \mathcal{T} . \mathcal{T} can be written in the following form [21],

$$\mathcal{T}(E, V, d) = e^{\left(-2d\sqrt{(m_e/\hbar^2) \cdot (\Phi_s + \Phi_t - 2E + eV)}\right)}, \quad (2.5)$$

where $\Phi_{s,t}$ are the work functions of the sample and tip. For deriving this expression it has been assumed, that the tunneling is purely vertical. As a further approximation, all surface state contributions other than of s or p_z symmetry have been disregarded (only surface states of quantum number $m = 0$ have been used). A further simplification to (2.5) is to neglect the contribution of the term $(-2E + eV)$ in comparison to the work functions which allows to take \mathcal{T} in front of the integral in (2.4).

$$I(V) \propto e^{-2\kappa \cdot d} \int_0^{eV} \rho_s(E, x, y) \cdot \rho_t(E - eV) dE, \quad (2.6)$$

where $\kappa = \sqrt{(m_e/\hbar^2) \cdot (\Phi_s + \Phi_t)}$ depends now only on the work functions $\Phi_{t,s}$ of the tip and the surface. Equation (2.6) is the final result of the approach. The first factor of (2.6) describes the exponential z -dependence of the tunneling current, which is commonly called “topography” information, while the integral factor depends on the density of states of the tip and the sample.

Several implications for the interpretation of STM images can be seen from (2.6). From the integral factor of (2.6) it is clear, that the STM does not show a real geometrical surface contour as it reflects electronic configurations rather than the positions of nuclei. Instead of measuring “heights” with the STM it is thus more appropriate to speak of “apparent heights” which are influenced by the LDOS. It is important to

realize that the STM does neither map contours of constant electron density (as would be given e. g. by orbital plots). As elastic tunneling only occurs for electrons at energies between E_F and $E_F + eV$, where V is the applied bias voltage, only the LDOS in this energy window contributes to the I signal. This can be seen from the integration limits of (2.6) and it is also graphically shown in Figure 2.1. The observed STM images are therefore also not plots of constant LDOS, instead they are plots of constant LDOS windows at the Fermi level. The LDOS (and therefore also such LDOS windows) can be computed using e. g. density functional theory which will be introduced in section 2.2.5. In principle this provides means to simulate STM images on the basis of a structural model. It should be noted, though, that the current or height signal of the STM is not dependent on the LDOS of the sample alone, as even in this crude approximation it also depends also on the LDOS of the tip, see (2.6).

The effect of adsorbates: Lang's Theory

Adsorbates on metal surfaces generally induce pronounced changes in the LDOS near E_F by electronic resonances derived from the interaction of the adsorbate states with the surface electron states. To investigate the degrees to which STM images of chemically different atoms vary, Lang [22, 23, 24, 25, 26] modeled the STM tunnel gap region as two planar metal electrodes on which adsorbates are chemisorbed; for simplicity, the metal electrodes were described by the so-called jellium model in which the ionic lattice of each metal is smeared out into a uniform, positive background. Lang [22] used the Bardeen tunneling formalism to calculate the current-density distributions from the wave functions that are calculated self-consistently within the local-density approximation for each electrode in the absence of the other [25]. It is seen that the Na 3s resonance and the S 2p resonances generate an increase in the LDOS at E_F , whereas for the electronegative C and O atoms, the 2p resonances lead to a depletion of the LDOS at E_F . In the constant-current STM mode, the adsorbates will therefore appear either as protrusions (Na, S) or as holes (C, O), depending on whether the adsorbates add to or deplete the LDOS at E_F . Thus Lang's results confirm the TH prediction for low V , that is, the STM images reflect the LDOS at E_F of the sample at the tip position rather than reflecting the geometrical position of the adsorbates.

Lang's STM formalism demonstrated the importance of adopting realistic atomic

potentials for the surface adsorbates. In general, more elaborate and detailed models may be required for a more detailed and even quantitative simulation of the experimental STM images. Tsukada et al. [27, 28] have formulated a method for theoretical simulations of STM images based on a first principles local density approach to the calculations of the electronic states of the tip and the surface. As the Bardeen perturbation formalism for the tunnel current is adopted, the electronic structures for the tip and the surface are calculated separately, using a slab model for the surface and a cluster model for the tip. The wave functions are represented by a linear combination of atomic-orbital (LCAO) numerical basis. Tsukada and co-workers studied, among many other things, the effect of the microscopic structure of the tip and found that 90% of the tunnel current is concentrated at the tip apex atom and that the tunnel current does not seem to depend crucially on the chemical identity of the apex atom. In order to incorporate tip-sample interactions, Doyen [29] and Sautet [30] have calculated the tunnel current in 'exact' scattering approaches going beyond the Bardeen transfer Hamiltonian formalism. In scattering approaches, the electron originates from the interior of the tip base, scatters from the tunnel junction, and has a certain probability for penetrating into the sample surface. Doyen et al. [31] have pointed out that, at small tip-sample distances, the strong tip-sample interaction may cause the interstitial regions between the atoms of a clean metal surface to appear as maxima in the variation of the tunnel current, an effect referred to as *image inversion* [32, 33, 34].

Organic molecules typically have only a small number of states at the Fermi level as this falls into their usually broad gap between the highest occupied and the lowest unoccupied molecular orbital (HOMO-LUMO). Non-resonant tunneling or inelastic tunneling can thus have a significant contribution to the current in these systems [35]. As the overall molecular tunneling contributions can be low, they can even be of comparable size to the direct tunneling to the surface although the surface is further away from the tip than the molecule. Tunneling can thus happen either via tip-molecule-surface or directly from tip to surface, which creates two competing current channels. The interaction of these channels can create interference effects which can completely change the observed apparent heights [36]. Although these limits have to be kept in mind when analyzing STM data, the STM is in general able to provide fast and in-depth information on the structure of adsorbates on surfaces. We have made good experiences in obtaining significant molecular tunneling contributions scanning in the so-called "filled

state imaging” with tunneling from the sample to the tip (see Figure 2.1b) which create realistic apparent height values.

2.2 Complementary techniques

We present here a short introduction to the complementary techniques employed to get a deeper understanding of the molecule/substrate systems discussed in this thesis. The NEXAFS and XPS data were taken at the HE-SGM beamline at BESSY II in Berlin in collaboration with Dr. Thomas Strunkus and Prof. Christian Wöll. RAIRS measurements were performed in group of Dr. Sam Haq and Prof. Rasmita Raval at the Surface Science Center of the University of Liverpool, UK. The RAIRS setup also contained a LEED and a TPD system.

2.2.1 X-ray Absorption Techniques

XPS

Deep-core electrons have binding energies corresponding to the energies of photons that lie in the X-ray region. In XPS analysis, the sample is placed in an ultrahigh vacuum environment and exposed to a low-energy, monochromatic X-ray source. X-ray excitation causes the emission of photoelectrons from the atomic shells of the elements present on the surface, Figure 2.2. The energy of these electrons is characteristic of the element from which they are emitted. By counting the number of electrons as a function of energy, a spectrum representative of the surface composition is obtained. The area under the peaks in the spectrum is a measure of the relative amount of each element present, and the shape and position of the peaks reflect the chemical state for each element. XPS is a surface sensitive technique because only those photoelectrons generated near the surface can escape and become available for detection. Due to collisions within the sample’s atomic structure, those photoelectrons originating much more than about 20 to 100Å below the surface are unable to escape from the surface with sufficient energy to be detected.

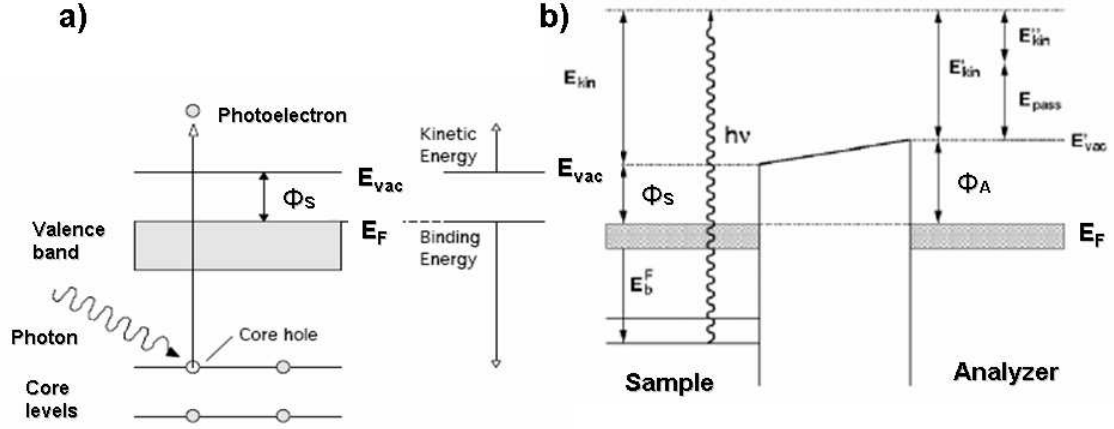


Figure 2.2: Schematic XPS energy diagram. (a) Schematic illustration of the photoemission principle (b) The electrons leaving the sample with kinetic energy E_{kin} enter the analyzer with energy E'_{kin} and are detected with energy E''_{kin} . The Fermi levels of the two systems have been equalized by an electrical contact between sample and analyzer.

Photoemission principle

The photoemission principle is illustrated in Figure 2.2a. By absorbing a photon, an atom gains an energy amount equal to $h\nu$. It then releases an electron to regain its original stable energy state. The released electron retains all the energy from the striking photon. With XPS, incident photons usually carry an energy ranging from 1 to 2 KeV. For example, usual X-ray sources as magnesium and aluminium emit at 1253.6 and 1486.6 eV respectively. The relative high level of the incident energy causes the sample to release an electron from an atom internal shell. Consequently, there will be some atoms lacking electrons in the internal shells from which photoelectrons have been released. To recover from this ionized state the atom can emit another photon (fluorescence) or undergo an Auger transition. On the low energy side of the spectrum secondary electrons and inelastic scattered electrons are detected, leading to the characteristic step-like shape of the spectrum. The principle of the conservation of energy allows us to write the energy balance equation, valid for the absorption of a photon carrying an energy of $h\nu$:

$$h\nu = E_{kin} + E_B + \Phi_S, \quad (2.7)$$

where E_B is the binding energy of the electron, Φ_S denotes the work function of the sample and E_{kin} is the kinetic energy of the electron leaving the sample(2.7). The photoelectrons enter the analyzer with the kinetic energy E'_{kin} and are detected with energy E''_{kin} (Figure 2.2b). The determination of the binding energy requires the values of the work functions of the analyzer Φ_A and sample Φ_S . However, it is sufficient to know the work function of the analyzer because the fermi level of the two systems have been equalized by an electrical contact. The spectrometer is then calibrated by measuring the binding energy of a well-known reference sample. Since the position of the orbitals in a particular atom is sensitive to the chemical environment of the atom, the chemical shift information is a very powerful tool for determining functional groups, chemical environment and oxidation states. It is intuitively clear that a reduced charge on the atom would increase the binding energy. The chemical groups are usually identified by comparison with reference peak positions compiled in literature.

NEXAFS

Opposite to the related x-ray photoemission spectroscopy (XPS) technique, where the photon energy is fixed and the electron intensity is measured as a function of electron kinetic energy, in Near Edge X-Ray Absorption Fine Structure (NEXAFS) the x-ray energy is scanned and the absorbed x-ray intensity is measured. This spectroscopic method refers to the absorption fine structure close to an absorption edge, at about the first 30 eV above the actual edge. This region usually shows the largest variations in the x-ray absorption coefficient and is often dominated by intense, narrow resonances. NEXAFS has particular application to chemisorbed molecules on surfaces. The spectra are frequently dominated by intra-molecular resonances of π or σ symmetry. The energy, intensity and polarization dependence of these resonances can be used to determine the orientation and intramolecular bond lengths of the molecule on the surface.

NEXAFS spectra can be recorded in different ways. The most common methods are transmission and electron yield measurements. The transmission technique requires thin foils while the electron yield technique, often called total electron yield (TEY) detection, can be used for conventional samples. The absorbed x-ray intensity is not measured directly in TEY measurements, but rather the photoelectrons that are created by the absorbed x-rays. X-rays are absorbed through excitations of core electrons

to empty states above the Fermi level. The created holes are then filled by Auger decay. The intensity of the emitted primary Auger electrons is a direct measure of the x-ray absorption process and is used in so called Auger electron yield (AEY) measurements, which are highly surface sensitive, similar to XPS. As they leave the sample, the primary Auger electrons create scattered secondary electrons which dominate the total electron yield (TEY) intensity. The TEY cascade involves several scattering events and originates from an average depth, the electron sampling depth L . Electrons created deeper in the sample lose too much energy to overcome the work function of the sample and therefore do not contribute to the TEY. The sampling depth in TEY measurements is typically a few nanometers, while it is often less than 1 nm for AEY measurements. NEXAFS is element specific because the x-ray absorption edges of different elements

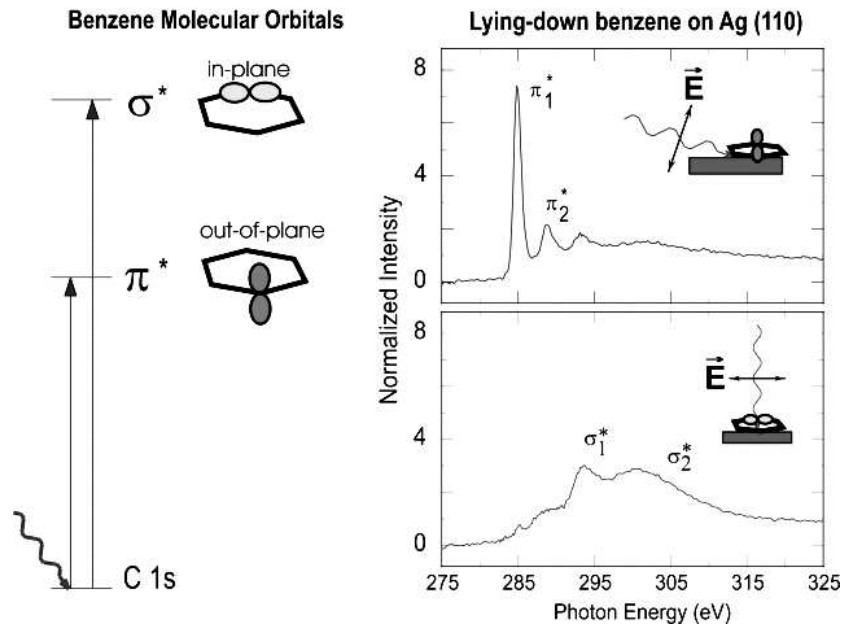


Figure 2.3: Polarization dependent NEXAFS spectra of benzene chemisorbed on Ag(110), illustrating the capability to determine molecular orientations, adapted from [37].

have different energies. NEXAFS is also very sensitive to the bonding environment of the absorbing atom. The NEXAFS spectrum exhibits considerable fine structure above each elemental absorption edge. This fine structure arises from excitations into

unoccupied molecular orbitals. In a related picture one can also think of the resonances arising from scattering of the excited low-energy photoelectron by the molecular potential. NEXAFS is dominated by multiple scattering of a low-energy photoelectron in the valence potential set up by the nearest neighbors. Often one can use a spectral "fingerprint" technique to identify the local bonding environment. The spectra exhibit chemical shifts within each group similar to XPS spectra but more importantly considerably different fine structure for carbon in different molecular groups. This clearly illustrates the power of NEXAFS to distinguish chemical bonds and local bonding. In many ways it is superior to XPS, which does not provide local structural information.

Another great asset of NEXAFS spectroscopy is its polarization dependence. Linearly polarized x-rays are best suited for covalent systems like macromolecules, which possess directional bonds. In this case the directional electric field vector of the x-rays can be viewed as a "search light" that can look for the direction of chemical bonds of the atom selected by its absorption edge. An example is shown in Figure 2.3 for the benzene molecule. Benzene, C_6H_6 , has unoccupied orbitals of σ and π symmetry which are oriented in and perpendicular to the ring plane, respectively. Polarization dependent NEXAFS spectra for benzene chemisorbed on Ag(110) are shown on the right. When the electric field vector \mathbf{E} is aligned along the surface normal, peaks due to the out-of-plane π orbitals are seen and when \mathbf{E} is parallel to the surface resonances due to the in-plane σ orbitals are dominant. This shows that benzene lies down on the Ag surface. In fact, benzene is only relatively weakly chemisorbed on Ag. For stronger chemisorption bonds (e.g. C_6H_6 on Mo or Pt) the π resonances broaden significantly, because the π orbitals are involved in the bond to the surface [37].

2.2.2 TPD

TPD could be defined as *"the beauty and the beast"* of surface science. It is a conceptually very simple technique but the interpretation and mathematical treatment of data can be easily misapplied. The TPD experimental procedure is straightforward. Molecules are adsorbed on a surface at a given temperature. The probability that molecule will desorb at any one temperature, to produce an equilibrium vapor pressure, is governed by Boltzmann statistics. By monitoring the partial pressures of species desorbed due to a linear increase in surface temperature, key information is obtained. The

amount and number of different kinds of surface species, the kinetics of the desorption process, the enthalpy of desorption, and differentiation between simple desorption and chemical reaction-desorption. Moreover, TPD recognizes the different adsorption conditions of the same molecule from the differences between the desorption temperatures of molecules desorbing from different sites at the surface, e.g. terraces vs steps. The monitoring of the desorbed molecules is usually done by a quadrupole mass spectrometer positioned in front of the sample. If the mass spectrometer collected and ionized all (a fraction) the adsorbates, the area under TPD $I(T)$ ¹curve would be equal (proportional to) the molecular coverage. The shape of the $I(T)$ curve and its dependence with different starting coverage contains information about the desorption kinetics. The principle of microscopic reversibility demands that a reaction passes through exactly the same states irrespective of whether it proceeds forward or backward. Adsorption and desorption can therefore be described by the same set of rate equations. The desorption rate is usually expressed by a rate law of n^{th} order. If the rate constant k_n is described by the Arrhenius equation, then the rate law is usually referred to as the Polanyi-Wigner equation, which defines the activation energy of desorption ΔE_{des} [38].

A kinetic analysis requires extensive experimental investigation and is beyond the scope of this thesis. Here TPD was only performed to get an insight into the chemical state of the adsorbed molecules at different temperatures, as a complement to XPS experiments.

2.2.3 RAIRS

For adsorbed molecules, molecular vibrations can be studied by shining infrared light onto the surface. If the molecule has a dipole moment, it can absorb infrared light, but only at certain fixed frequencies. Hence, an infrared spectrum of light reflected from the surface will show absorption peaks which are characteristic of the molecule and its adsorption geometry on the surface. This is the basis of Reflection absorption infrared spectroscopy (RAIRS), where an IR beam is specularly reflected from the front face of a highly-reflective sample, such as a metal single crystal surface. It can be shown theoretically that the best sensitivity for IR measurements on metallic surfaces is obtained using a grazing-incidence reflection of the IR light [39]. The reflected light is

¹ I refers to the intensity of the signal

recorded by a spectrometer outside the UHV chamber using IR transmitting windows. The signal for a surface with a molecular adsorbate is analyzed relative to a background signal obtained on the pristine surface.

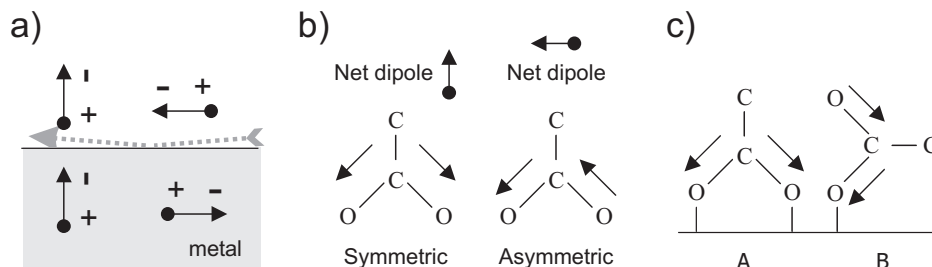


Figure 2.4: Principle of RAIRS. RAIRS at surfaces: a) dipoles and mirror dipoles; b) dipole moments of the symmetric and asymmetric vibration of the carboxylate group; c) vibration modes detectable with RAIRS [39].

The observation of vibrational modes of adsorbates on metallic substrates is subject to the *surface dipole selection rule*. This states that only those vibrational modes which give rise to an oscillating dipole perpendicular to the surface are IR active and give rise to an observable absorption band. Further information on the selection rules for surface IR spectroscopy can be found in the review by Sheppard and Erkelens [40]. It is important to notice that even if a transition is allowed it may still be very weak if the transition moment is small. Electric dipoles as generated by vibrating molecules in front of a metallic surface induce mirror dipoles (see Figure 2.4a). For dipoles oriented parallel to the surface, real and mirror dipole cancel each other, while for dipoles oriented perpendicular to the surface an increased overall dipole-moment exists. As an example, Figure 2.4b shows the asymmetric and symmetric stretch modes of the carboxylate group. As can be seen from Figure 2.4c, the symmetric mode can only be detected if the molecular group is oriented vertical on the surface. In an inclined orientation the signal strength will be reduced, for flat orientation no absorption will be detected. The asymmetric stretch, on the other hand, is only observed for a flat orientation of the group, as only in this case a vertical dipole moment exists. RAIRS can thus provide double information: it shows which functional groups exist on the surface (if they are detectable). And in the ideal case it allows to deduce the orientation of the molecule from a combined analysis of the observed oscillation modes.

2.2.4 LEED

The demonstration that the electron has a wavelike behavior was a milestone in the development of modern physics. In 1927 Davisson and Germer published the first LEED pattern from Ni single-crystals, demonstrating the original prediction of de Broglie [16]. The wavelength λ associated with an electron of energy E is given by

$$\lambda = \frac{h}{\sqrt{2m_e \cdot E}} . \quad (2.8)$$

Using electrons with energies between 10 eV and 100 eV this wavelength can be tuned between ≈ 0.4 nm and 0.1 nm. Electrons in this energy window interact strongly with the solid state lattice and have a mean free path of only 0.5-1 nm in the solid. When incident onto a surface, most of the electronic wave is thus scattered by the top 3-4 surface layers. Out of these, low energy electron diffraction (LEED) analyzes the elastically diffracted electrons [41]. They carry the reciprocal space information of the surface lattice and of overlayer structures, such as a molecular adlayer. The backscattered electrons are focussed by means of electrostatic optics onto a fluorescent screen where they show spots representing the 2D reciprocal lattice of the surface structure. From measuring the unit-cell vectors of the surface, one can reconstruct the real-space lattice. When analyzing an overlayer structure, the most straightforward way is to measure the extra spots of the overlayer vectors \mathbf{a}_O^* , \mathbf{b}_O^* with respect to the spots of the substrate lattice \mathbf{a}_S^* , \mathbf{b}_S^* of the reciprocal lattice. Using a matrix notation

$$\begin{pmatrix} \mathbf{a}_O^* \\ \mathbf{b}_O^* \end{pmatrix} = \mathbf{M}^* \cdot \begin{pmatrix} \mathbf{a}_S^* \\ \mathbf{b}_S^* \end{pmatrix} , \text{ with } \mathbf{M}^* = \begin{pmatrix} m_{11}^* & m_{12}^* \\ m_{21}^* & m_{22}^* \end{pmatrix} . \quad (2.9)$$

The real matrix \mathbf{M} is then the inverse transpose of \mathbf{M}^* [41]. This allows to construct the overlayer lattice vectors in real space \mathbf{a}_O , \mathbf{b}_O in terms of the real space substrate lattice vectors \mathbf{a}_S , \mathbf{b}_S [42, 6]

$$\begin{pmatrix} \mathbf{a}_O \\ \mathbf{b}_O \end{pmatrix} = \mathbf{M} \cdot \begin{pmatrix} \mathbf{a}_S \\ \mathbf{b}_S \end{pmatrix} . \quad (2.10)$$

Integer components of \mathbf{M} signify commensurate overlayers. For an orthogonal overlayer lattice which is parallel to the substrate lattice the off-diagonal entries of \mathbf{M} vanish and the compact $(m_{11} \times m_{22})$ notation can be used for describing the primitive unit cell. The case of a centered unit cell can also be described by a similar short notation as $c(n \times m)$.

2.2.5 Theoretical simulations

All the theoretical simulations reported in this thesis have been performed by Giulia Tomba, under the supervision of Dr. Lucio Colombi Ciacchi and Prof. Alessandro De Vita from the King's College London (UK) the Center of Excellence for Nanostructured Materials (CENMAT) and INFM-DEMOCRITOS National Simulation Center in Trieste (Italy). As many of the results in this thesis are based on a comparison between STM measurements and DFT calculations, here we present a very brief and conceptual introduction to the theoretical foundations. A more rigorous mathematical treatment can be found in [43]. Specific details about calculations on the systems informed here, such as model schemes, pseudopotentials, etc, can be found on a recent publication [44].

Molecular dynamics

Molecular dynamics is a computer simulation technique which aims to understand the structural and physical properties of matter in all its forms: solid, liquid and gas. The basic concept is very simple: once the system of interest has been modeled as a set of interacting particles, its time evolution can be followed by first calculating the forces acting on each particle, and subsequently integrating the corresponding equations of motion. After having collected enough information on the motion of the single particles, it is possible to reconduct the time averages calculated on the time of observation to statistical averages. In this way, it is possible to gain important information on the equilibrium properties of the system. Beyond this use, molecular dynamics can also be applied to other purposes, such as the study of non-equilibrium processes, or the optimization of structures overcoming local energy minima (simulated annealing). In principle, the description of a system of nuclei and electrons would require the solution

of the Schrödinger equation:

$$H\Psi(\mathbf{r}, \mathbf{R}) = E\Psi(\mathbf{r}, \mathbf{R}). \quad (2.11)$$

Such a task is unaffordable, except for very simple systems. It is therefore necessary to introduce some approximations. Since the electrons are several times lighter than the nuclei and therefore move much faster, Born and Oppenheimer proposed that the electrons could be considered to follow instantaneously the motion of the nuclei, still remaining very close to their ground state. This approximation, which is also known as the adiabatic approximation, allows to decouple the electronic and ionic dynamics, giving two separate equations. The first of these equations describes the motion of the electrons and depends only parametrically on the nuclear positions, which are considered fixed. Its solution leads to the ground state energy $E_0(\mathbf{R})$, which defines the potential for the motion of the nuclei. The correct evaluation of E_0 is still very complicated, and the problem can be approached in different ways. Ab initio methods try to solve the motion equation directly, introducing some further approximations in order to make the task affordable. Classical molecular dynamics, instead, simply replace the potential E_0 with an appropriate empirical fit $V(\mathbf{r}, t)$ which tries to mimic the true potential through a series of parameters. [44]

AMBER

All the classical molecular dynamics simulations which will be referred to from this point on were performed using the AMBER 8 suite of programs [45] and the forcefields therein provided (gaff - Generalized AMBER Force Field, and *ff03* in particular [46, 47]). This software package is particularly devoted to the study of biological molecules such as proteins and nucleic acids. The potential energy function has into account the bond, angular, dihedral, van der Waals and electrostatic contributions. The positions of single atoms can be restrained using a harmonic potential, while the temperature of the system can be controlled applying the weak-coupling to a thermal bath. In this case coupling either removes or adds energy to the system to maintain the temperature constant [48].

Density Functional Theory (DFT)

Density functional theory (DFT) is a parameter-free theoretical method which is built only on physical laws and thus is “ab-initio”. Using DFT, it is possible to calculate the electronic structure of a set of atoms (typically less than about 100) with high precision. Periodic boundary conditions are mostly employed when used for a surface where the periodicity in z -direction is maintained by treating the surface as a slab with vacuum on-top and by periodically repeating both slab and vacuum in a supercell.

As introduced in the previous section, DFT is based on the Born-Oppenheimer approximation which exploits the fact that electrons move much faster than atomic cores. A full calculation can thus be split into two nested calculation loops. In the inner one, DFT determines the electronic distribution for a given set of atomic nuclei positions, while in the outer loop this electronic distribution is used to calculate the forces between the atoms [49, 50]. The so-called relaxation of the atomic positions is then a step-wise movement of the nuclei according to these forces until the forces become smaller than a predefined value. Due to the loop nesting, each relaxation step includes a full inner loop of self-consistent calculation. The final configuration is then the energetically optimal configuration both for nuclei and electrons.

It is clear that important input parameters of DFT are the number and the type of the atoms of a structure as well as the periodicity of the structure as this is needed to build the initial supercell. A possibly crude model of the atomic position is also extremely helpful as input. Such a model can be build using the results of STM, LEED or similar structure-resolving experimental techniques.

2.3 Experimental setup

2.3.1 The STM system

The setup consists of two chambers, the preparation chamber for sample cleaning and deposition and the analysis chamber comprising the STM. A photography of the whole system is shown in Figure 2.5.

The preparation chamber is equipped with the following standard components: firstly, an ion gun which is used for sputter cleaning of the sample substrates. For

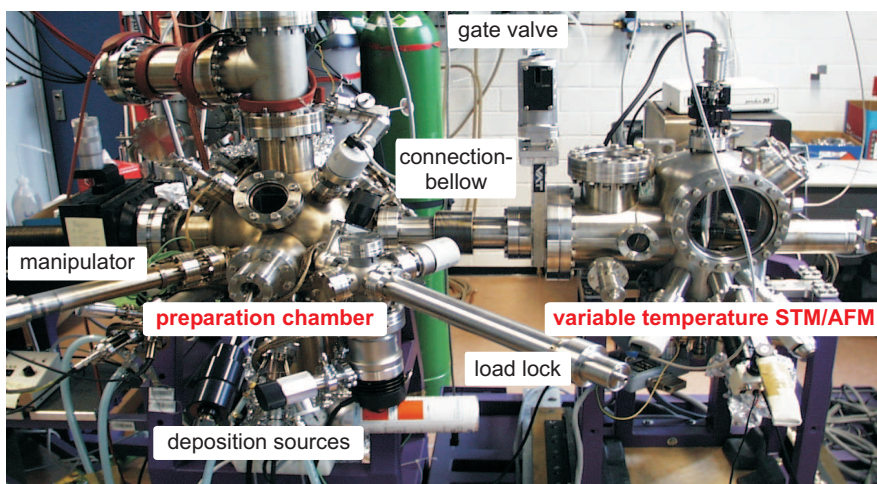


Figure 2.5: STM-Setup consisting of the preparation chamber and the analysis chamber comprising the STM.

the Cu(110) surface we typically have applied a high voltage of 900 V with a sputter current of 12-15 μA for a sample surface of about 13 mm². For this a filament current of 2.7 A for a new filament and about 1.5 A for an old filament was necessary with an almost linear degradation in between. The Ar pressure during sputtering was about $6 \cdot 10^{-6}$ mbar. Secondly, a quadrupole mass-spectrometer for analyzing residual gases. Thirdly, a standard molecular beam epitaxy source (MBE, Omicron Nanotechnology GmbH) for depositing metals such as Fe.

Next, organic molecular beam epitaxy sources for evaporating molecules, namely two single commercial sources and two home-built double sources. Both contain ceramic crucibles made of boron nitride or aluminium oxide. Heating is achieved by a metallic filament and the crucible temperature is read by a thermocouple. The temperature reading offset between the two source types turned out to be significant: when calibrating to obtain the same molecular flux with the same molecule, the commercial source showed a 35 K lower reading (at 460 K) than the home-built one. The home-built sources have been installed on retractable load mechanisms which allow a molecule change without breaking the vacuum of the chamber. This also prevents a total evaporation of the molecules which might occur when baking the whole setup at high temperatures. Fine dosing valves for dosing gases (especially oxygen for deposition and Ar for sputtering) are also mounted onto the preparation chamber.

The vacuum in this chamber is maintained by a turbo pump (Leybold, 360 l/sec) which allows to reach a base pressure of $1 \cdot 10^{-10}$ mbar. An ion pump (Meca 2000, 400 l/sec) is able to keep this vacuum when the turbo pump is shut off and isolated from the system by a plate valve to avoid vibrational noise during STM measurements. The preparation chamber also contains a load lock for fast sample and tip transfer from outside. Finally, the chamber comprises a home built sample preparation stage mounted on a manipulator. The manipulator is also used to transfer the samples to and from the STM chamber without breaking the vacuum. The connection is made via a bellow to reduce vibrations on the STM chamber and via a gate valve to separate the vacua.

The STM chamber is pumped by a smaller ion pump (Varian, 150 l/sec). The base pressure in this chamber is in the low 10^{-11} mbar region, which allows to measure even reactive metal surfaces such as Cu over periods of several days or even a week without significant surface contamination. The chamber contains a sample carousel in which 12 samples or tip holders can be stored. No deposition sources were mounted to the chamber, only a fine dosing valve for in-situ deposition of oxygen. The STM itself is a commercial variable temperature STM/AFM (Omicron Nanotechnology) which is designed to work in the nominal temperature range of 25 K to 750 K. The lower temperature limit applies only for specific low temperature sample holders which prevent sample heating and were thus not used in this work. With the commercial resistive heating type sample holder, the nominal lowest temperatures is about 45 K when cooling with liquid He and about 110 K when cooling with liquid Nitrogen. The cryostat for cooling is a flow cryostat which can be coupled to the STM head via a moveable Au-cold-finger. The STM head itself is mounted on a very effective eddy-current damping stage for vibration isolation. Additionally, the whole STM chamber is mounted on a passive damping system (Newport). Sample heating is possible by counter-heating the cryostat upon cooling.

The measurements have been performed mainly on two Cu(110) crystals. The mis-cut angle of the Cu(110) crystals was smaller than 0.1° , which allowed terrace widths of up to 200 nm. Electrochemically etched tungsten tips were used for all STM measurements, which were stored also in the carousel. As tips can easily be re-prepared on a metal surface by “dipping” them into the surface [51], overall only 5 different tips were used for the measurements presented here.

Scanning Conditions STM measurements were performed in the constant current mode. Typical tunneling current and sample bias voltages were $I = 0.9$ nA and $V = -0.9$ V for molecular imaging and $I = 0.7$ nA and $V = -0.3$ V for measuring the Cu surface with atomic resolution

2.3.2 Sample preparation

The Cu(110) sample was cleaned by cycles of Ar^+ sputtering (15 minutes with a kinetic energy of 900 eV and a current density of about $1 \mu\text{A}/\text{nm}^2$) and flash annealing to 750 - 820 K. Argon gas was used as supplied in metal bottles (nominal purity 5.0) and was inserted into the chamber through a fine-dosing valve. The connection of the gas bottles to the fine dosing valves was formed by stainless steel tubes (delivered electrochemically purified) which were regularly cleaned by baking and cycles of flushing and pumping to $5 \cdot 10^{-6}$ mbar using a turbo pump.

2.3.3 Molecular deposition

Organic Molecular Beam Epitaxy²(OMBE) is a thin film deposition technique for epitaxial growth of thin organic films in ultrahigh vacuum (UHV). Epitaxial growth is performed by deposition of the material from molecular beams of the constituent molecules with at a crystalline substrate surface held at a suitable temperature. The ultra clean UHV atmosphere allows the growth of layers free of contaminants. On a microscopic scale, the source molecules arrive randomly on the surface. At first these molecules migrate and finally assemble into a configuration determined by the kinetic and thermodynamic properties of the system. The growth mode is a complicated balance of many competing process, as aggregation, nucleation, dissociation and diffusion. The dominant processes are characterized by an activation energy and a prefactor and can be described mathematically by Arrhenius-type exponential laws. The film morphology, as the outcome of the competitive processes, is strongly affected by the experimental conditions, i.e., the flux of molecules impinging on the surface (deposition rate), the substrate temperature symmetry and chemistry.

²Epitaxy: the growth of a thin layer on the surface of a crystal so that the layer has the same crystallographic structure as the underlying crystal

Operating Principle of the K-Cell

Knudsen cells are often used for generating molecular beams in OMBE. The Knudsen cell utilizes the principle of molecular effusion (demonstrated by Knudsen in 1909). The Knudsen effusion method involves placing a condensed sample in a Knudsen cell, a small enclosure, that is uniformly heated and held until equilibrium is attained between the condensed and vapor phases. The vapor is continuously sampled by effusion through a small orifice in the cell into vacuum and a molecular beam is formed. The molecular evaporation has been checked in situ with by a quadrupole mass spectrometry analysis (QMS) system. The molecules were dried in a desiccator prior to insertion in the OMBE cells. All molecules were thoroughly degassed prior to sublimation. No significant pressure raise in the UHV chambers was observed during deposition. Table 2.1 lists the treatment procedures for the molecules.

Molecule	Supplier	Purity	Degassing in UHV	Evap. T.
L-Phe	Bachem	99%	\approx 10 h, up to 380 K	400 K
L-Tyr	Bachem	99%	\approx 10 h, up to 450 K	466 K
L-Phe-L-Phe	Bachem	99%	\approx 10 h, up to 445 K	455 K
D-Phe-D-Phe	Bachem	99%	\approx 10 h, up to 445 K	455 K
D-Phe-L-Phe	Bachem	99%	\approx 10 h, up to 440 K	450 K
L-Phe-D-Phe	Bachem	99%	\approx 10 h, up to 440 K	450 K

Table 2.1: Organic molecules: purity, cleaning, and sublimation temperature.

Chapter 3

Supramolecular Organization of Amino acids on Cu(110)

Understanding the basic requirements for chiral templation and enantioselectivity is crucial to the development of more effective separation methods and reactions used to achieve enantiopurity. Amino acids and peptides appear as good candidates for the creation of enantioselective surfaces, since they present a variety of functional groups that can be chosen to achieve specific reactions. They all share a general formula $\text{NH}_2\text{C}^*\text{HRCOOH}$. In the α -amino acids, the amino and carboxylate groups are attached to the same chiral C^* , which is called the α -carbon. The various α -amino acids differ in which side chain (R group) is attached to their alpha carbon. Although the enantioselectivity of metal surfaces templated with organic modifiers has been demonstrated by a couple of experiments over the past years, the requirements for the design of enantioselective surfaces are not yet clear. In particular, local characterization of the supramolecular structures formed by the chiral modifiers and systematic studies on the effects of specific molecular adsorption and ‘chiral footprints’¹ of the same molecule on the templating effect are very rarely found in literature [5]. One proposition is that for a surface to show enantioselectivity, the template molecule should be rigidly bonded to the surface in order to prevent azimuthal rotation of the chiral center [3]. This lack of freedom would allow the adsorption mode of the chirally modified organic reactant

¹the adsorption geometry determined by the preferential interaction of specific functional groups in close proximity to the surface

to be more strictly controlled, enabling the enantioselective response to survive under a variety of conditions [52]. More recent studies on amino acids seem to support this hypothesis, suggesting that two anchoring adsorption points are needed for chiral templating to work.

To get an insight into the basic requirements for bestowing chirality to achiral metal surfaces, we have studied the chiral templation of the amino acid L-Phe (Figure 3.1b) on the Cu (110) substrate. As a first step, Reflection-Absorption Infrared Spectroscopy (RAIRS) and Temperature Programmed Desorption (TPD) have been combined to determine the chemical states, orientations, molecular arrangements and bonding interactions of the molecules at the copper surface. Information on the local level was then obtained by STM. The interpretation of the adsorption geometries is aided by molecular dynamics simulations. The studies show that L-Phe is present on different chemical states going from acidic to zwitterionic to anionic depending on the adsorption temperature in the 85 K-400 K range. We concentrate on the phase at 400 K to discuss the interplay of inherent molecular chirality and the expression of chiral motifs induced by the preferential adsorption geometry of two anchoring points to the surface in terms of conformational flexibility and optimized molecule-surface interactions (footprint chirality). Moreover, we study the effect of a third anchoring point molecule-surface by comparative adsorption of L-Tyr (Figure 3.1c) on Cu(110). Our results show that preventing the conformational flexibility for rotation of the functional groups around the chiral center is of crucial importance for the expression of only one chiral footprint on the surface. This is likely to play an important role for potential enantioselective reaction paths on the templated surface.

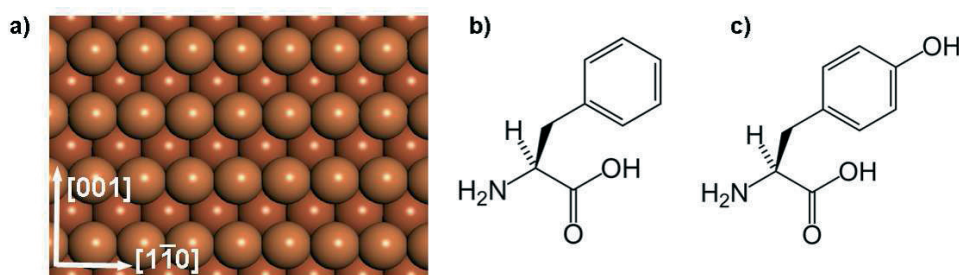


Figure 3.1: Schematic representation of a) Cu (110) b) L-Phe c) L-Tyr

3.1 Sample Preparation

For the deposition of L-Phe on Cu(110) we have used the parameters listed in section 2.3.2. The measurements were carried out in the Surface Science Center, Liverpool, UK in the group of Dr. S. Haq.

3.2 Reflection-Absorption Infrared Spectroscopy measurements

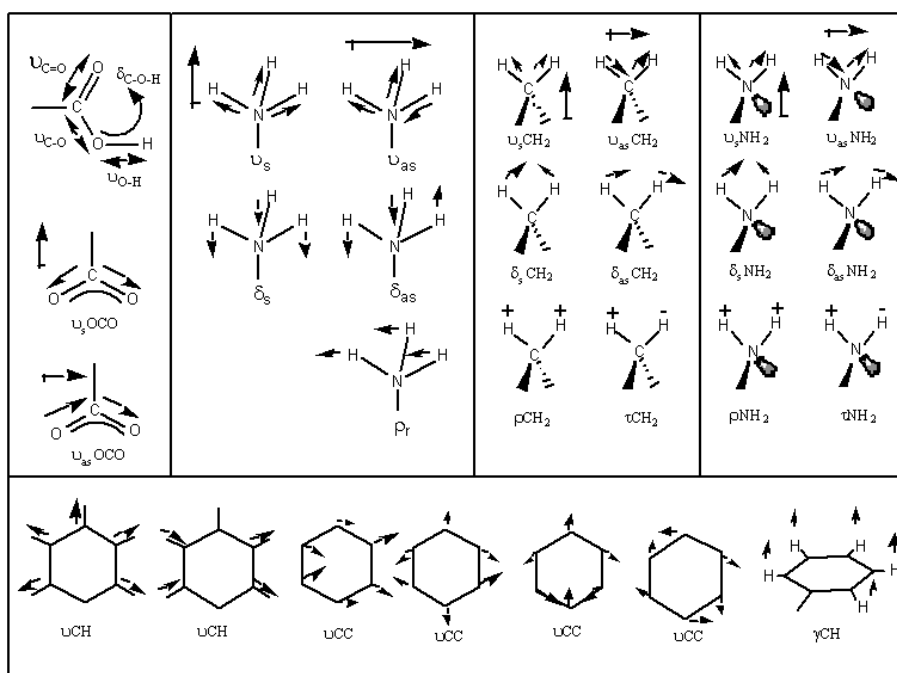


Figure 3.2: Principal vibrational modes associated with the functional groups of L-Phe. ν =stretch, τ =torsion, δ =deformation, ρ =wagging, γ =bend, s = symmetric, as =asymmetric.

As introduced in Section (2.2.3), the chemical identity of the functional groups can in principle be determined from their vibrational spectra. The selection rules inherent with this particular technique also allow one to gauge the relative orientation of the main functional groups with respect to the surface plane, as only those vibrations with a component of the dynamic dipole moment perpendicular to the surface are infrared

active. However, it must be stressed that the adsorption symmetry of the molecule formally dictates whether a vibrational mode is IR active. Therefore, for low adsorption symmetries vibrational modes polarized parallel to the surface become formally allowed, however, the intensity of an IR band is governed by the strength of the dynamic dipole which would be very weak for vibrations parallel to the surface and hence have very small IR absorption strengths. The main vibrational modes expected for the functional groups of the amino acids analyzed in this chapter are schematically shown in Figure 3.2. Each functional group has a characteristic set of absorption bands, referred to as group frequencies, which can be used to establish their identity. An important aspect of amino acids is that their chemical form varies from acidic (NH_2RCOOH), to anionic (NH_2RCOO^-), to zwitterionic ($\text{NH}_3^+\text{RCOO}^-$), or to cationic ($\text{NH}_3^+\text{RCOOH}$), according to their environment. Thus, a critical point to address when studying their behaviour at a metal surface is ‘What is their chemical form on adsorption?’. In the gas phase, most amino acids are present in their acidic form whereas in the solid phase they are usually zwitterionic. Therefore, the IR spectra from each of these forms needs to be considered for a detailed analysis. In the case of Phe, these states can be created in aqueous solution at different pH’s and therefore their IR spectra are useful for comparison [53]. In addition, Phenylalanine in the solid zwitterionic state [54, 55, 56, 57], Cu[Phe]_2 inorganic complexes and related complexes [56, 57, 58], as well as the IR spectra of related amino acids adsorbed on Cu(110) [59] can also be used as reference material. The main vibrational modes have been collated and listed in Table 3.1.

A brief inspection of this table shows that there is considerable overlap of the frequencies of the different functional groups, which makes unambiguous identification difficult. Further complications arise due to the mixing of mode, i.e. the vibrations are not localized to particular bonds but instead contain contributions from several of these. When adsorbed on a metal surface, the adsorption temperature can be used as a parameter to create the different chemical states. Therefore, a complete analysis at different adsorption temperatures is needed in order to facilitate the identification of the final chemical state and adsorption geometry of the 400 K phase investigated by STM in the next section.

Mode	Description	Direction	Frequency cm^{-1}
Carboxylic group			
$\nu(OH)$	O-H stretch (free)	in-plane	3000
$\nu(OH)$	O-H stretch (H-bonded)	in-plane	3000-3300 v.b.
$\nu(C=O)$	C=O stretch	in-plane	1700-1750
$\nu(C-O)$	C-O stretch	in-plane	1200-1340
$\delta(COH)$	C-O-H bend	in-plane	1300-1400
$\nu(X-COOH)$	C-C stretch	in-plane	1150-1200
Carboxylate group			
$\nu_{as}(OCO)$	asym. OCO stretch	in-plane	1500-1650
$\nu_s(OCO)$	sym. OCO stretch	in-plane	1350-1450
Phenyl group			
$\gamma_{as}(C-H)$	asym. C-H bend	o.o.p	900-1000
$\gamma(C-H)$	C-H bend	o.o.p	702, 746-756
$\nu(C-H)$	C-H stretches	in-plane	3000, 3030, 3060
$\nu(CC)$	C-C stretches	in-plane	1454, 1497, 1605, 1035
Amino group			
$\nu(NH)$	N-H stretches	in-plane	3200-3400
$\delta(NH)$	N-H scissoring	in-plane	1560-1630
$\omega(NH_2)$	H-N-H wagging	o.o.p.	1100-1150
Ammonium group			
$\nu(NH)$	asym.+sym. N-H stretches		3020-3100
$\delta_s(NH_3^+)$	deformation	in-plane	1480-1500
$\delta_{as}(NH_3^+)$	deformation	o.o.p.	1630-1650
$\rho(NH_3^+)$	rocking	o.o.p.	980-1150
CH ₂ group			
$\delta(CH_2)$	CH ₂ deformation	in-plane	1300-1340
$\rho(CH_2)$	CH ₂ rocking	o.o.p.	750
Molecular skeleton			
$\nu(CH_2)$	H-C-H	in plane	2870
$\nu(CCN)$	C-C-N stretch	o.o.p.	1000-1200
$\nu(CC)$	C-C stretch	in-plane	1055
$\nu(CCN)$	C-C-N stretch	in-plane.	900-1000

Table 3.1: Assignment of the main absorption bands experimentally observed. o.o.p = out-of-plane, asym. = asymmetric, sym. = symmetric, v.b. = very broad. NB: For non-planar groups the orientation is defined with respect to the local axis of symmetry

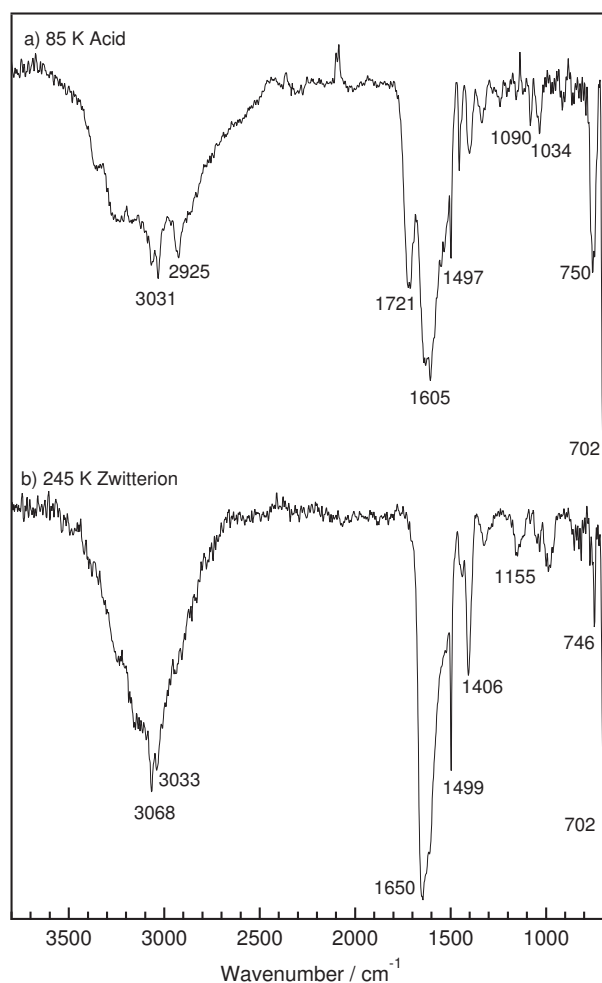


Figure 3.3: RAIRS of L-Phe on Cu(110). Reference multilayer adsorbed at a) 85 K and b) 245 K.

Acid Phase at 85 K

In order to characterize the acid form, it is useful to measure the IR spectra of the vapor deposited amino acids at low temperature (Figure 3.3a). The IR spectra measured at 85 K does indeed show the presence of intact carboxylic acid groups characterized by absorption bands at 3000 (very broad), 1720, 1400 and 1335 cm^{-1} corresponding to the $\nu(\text{OH})$, $\nu(\text{C}=\text{O})$, $\delta(\text{COH})$ and $\nu(\text{C}-\text{O})$ vibrations, respectively. The broad signal

of the OH stretch is indicative of extensive hydrogen bonding of hydroxyl groups. The NH_2 groups also show the tendency to form intermolecular hydrogen bonding which is clearly evident in the IR spectra as this leads to a considerable broadening of the IR bands particularly the symmetric and asymmetric NH stretches between 3200 and 3400 cm^{-1} and the scissoring mode at 1600 cm^{-1} . In contrast, the vibrational modes of the phenyl group are relatively sharp, since this group generally shows little hydrogen bonding, as evidenced by the C-H stretches at 3000 and 3060 cm^{-1} , C-C stretches at 1454 and 1497 cm^{-1} and the out-of-plane C-H bending modes at 702 and 756 cm^{-1} . The CH_2 and the C-C-N skeletal vibrations are also important part of the infrared fingerprint and are listed in Table 3.1. At this temperature there is no significant variation of the intensity of the absorption bands, therefore one can assume that the molecule aggregates randomly on the surface without any preferential orientation.

Zwitterionic Phase at 245 K

The adsorption of L-Phe at 245 K shows a significant difference in the IR spectra (Figure 3.3b), with the complete absence of the 1720 cm^{-1} mode associated with the $\nu(\text{C=O})$ vibration of the acid group. This signifies the conversion of the acid into the zwitterion form, with the transfer of the proton from an acid (COOH) to an NH_2 group, and thus producing carboxylate (COO^-) and ammonium (NH_3^+) groups. These latter groups have their own distinct IR signatures, which are characterized by absorption bands listed in Table 3.1. The IR signature of anionic carboxylate group is a pair of relatively strong absorption bands for the symmetric and asymmetric (OCO) stretches at around 1406 and 1600-1650 cm^{-1} . The NH_3^+ group is identified by a strong broad band at about 3100 cm^{-1} for the symmetric and asymmetric N-H stretches, strong symmetric and asymmetric deformation mode at 1500 and 1650 cm^{-1} respectively and rocking mode at 1150 cm^{-1} .

Room temperature and 400 K phase

The IR spectra measured as a function of increasing coverage at 300 K clearly shows a significantly different vibrational structure of the monolayer phase in comparison to that of the multilayer (Figure 3.4). For the lowest coverage shown the bands at 1055 and 1100 cm^{-1} are in the range expected for the C-C and C-N stretches of the molecular

skeleton. With increasing coverage the appearance and disappearance of some of the absorption bands indicates that there is a coverage dependent conformational change of the molecules, presumably driven by steric interaction between neighboring molecules. Despite its complexity, this can be simplified by considering the vibrational modes of each group, and thus deriving an adsorption geometry. Therefore starting with the acid group, the appearance of a band at 1402 cm^{-1} ($\nu_s(\text{OCO})$) and the absence of modes between $1500\text{--}1600\text{ cm}^{-1}$ ($\nu_{as}(\text{OCO})$) indicate firstly that the acid group is deprotonated and secondly that it is symmetrical bound to the surface in a bidentate fashion. Generally, for simple carboxylic acids this mode shows very strong IR absorption bands on surfaces, the weak intensity of this modes initially relative to the other modes (spectra a and b in Figure 3.4) indicates that the carboxylate group has a large inclination angle. At higher coverages a mode appears at 1607 cm^{-1} which can be associated with the $\nu_{as}(\text{OCO})$ vibration, which indicates a symmetry change of this group. However, as the dynamic dipoles of the ν_s and $\nu_{as}(\text{OCO})$ vibrations are orthogonal this would result in a decrease in intensity of the former, which is not seen. There the appearance of this asymmetric mode indicating a monodentate configuration for the carboxylate group is most probably due to some molecules near saturation coverage which cannot bind symmetrically. Support for this comes from warming the saturated overlayer to 400 K which results in the attenuation of this latter mode with very little change to the rest of the IR spectrum, Figure 3.4.

The phenyl group has a large number of vibrational modes, the IR bands associated with these modes have a relatively narrow line width and so are readily identifiable. Furthermore, as the vibrations are polarized in three orthogonal directions the relative orientation of this group with respect to the surface can be determined. For instance if the molecular plane of this group was parallel to the surface then due to the dipole selection rule, the out-of-plane mode would be the most intense, on the other hand for a perpendicular geometry only the in-plane modes would be observed. For the data shown in Figure 3.4, an out-of-plane C-H bending mode at 756 cm^{-1} is observed for low coverages (spectra a and b) with the absence of in-plane modes. However, with increasing coverage this mode attenuates as the in-plane modes at 3066 , 3033 and 1497 cm^{-1} appear. This is indicative of a reorientation of the phenyl group towards a more upright geometry, which is possible through the rotation of this side group, presumably to reduce the steric interaction with neighbours as the coverage increases.

The rotation/reorientation of this side group is further supported by the accompanying changes in the absorption bands of the CH_2 group. For low coverages these are seen at 2870 and 1451 cm^{-1} for the $\nu_{as}(\text{CH}_2)$ and $\delta(\text{CH}_2)$ vibrations, respectively. However, these attenuate as this side chain rotates and the phenyl modes become IR active. To

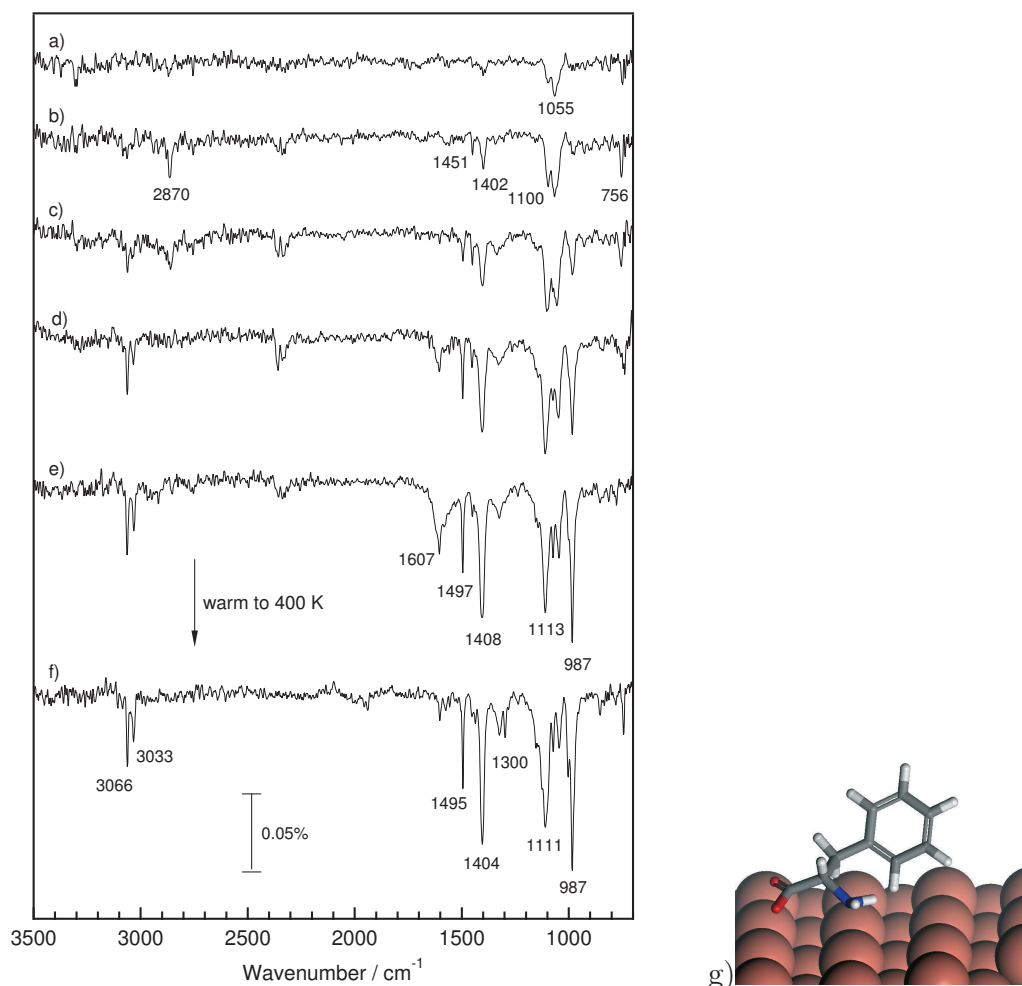


Figure 3.4: RAIRS of increasing coverages of L-Phe on Cu(110) adsorbed at a), e) 300 K and f) after annealing at 400 K . g) schematic adsorption geometry at 400 K.

define the chemical state of the molecules one has to determine the fate of the original NH_2 group, i.e. if it remains as it was or it reacts with the acid proton to produce a

NH_3^+ group, as observed at 245 K. This is rather more difficult to ascertain than it would appear, as the geometry of this group determines which modes are observed. However, as no modes are observed in the NH stretching region, to establish its identity one has to use the deformation modes. For a NH_3^+ species the δ_s and $\delta_{as}(\text{NH}_3^+)$ vibrations are to be found around 1500 and 1650 cm^{-1} respectively, whereas for the NH_2 species the $\delta(\text{NH}_2)$ vibration is around 1600 cm^{-1} . These values together with the fact that the $\nu_{as}(\text{OCO})$ vibration also occurs in this range makes it difficult to use this region to determine the identity of the group. However, the NH_3^+ rocking and NH_2 wagging modes are located at 1150 and 1105 cm^{-1} respectively, and indeed we do see a band around the 1113 cm^{-1} range which can be associated with a NH_2 group. If this group binds to the surface via its lone pair of electrons then the only dipole active mode would be the out-of-plane wag as the other would have their dipoles parallel to the surface. Support for this assignment comes from TPD data measuring H_2 evolution after adsorption at 240 K, Figure 3.5. The data clearly shows recombinative desorption of H_2 starting at 290 K and maximizing at 330 K, which is the range expected for this process [60]. The

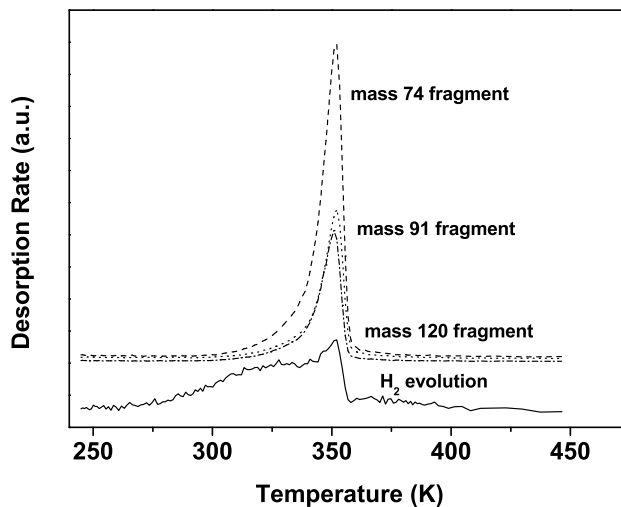


Figure 3.5: TPD spectra showing the recombinative desorption of H_2 after adsorption of L-Phe on Cu(110). The fragments 74, 91, 120 indicate molecular desorption (cracking pattern)

proposed adsorption model for the final configuration at 400 K is shown schematically

in Figure 3.4g. The orientation and adsorption geometry result in a chiral footprint, in which two different chemical groups (carboxylate and amino) are in close proximity to the surface, as also observed for Glycine [61] and Alanine [59] on Cu (110). Local characterization and further support for this model is obtained by STM measurements and molecular dynamics simulations discussed in the following section.

3.3 STM measurements and footprint chirality

When L-Phe is deposited onto Cu(110) at room temperature and annealed at 400 K for 5 minutes, STM imaging reveals supramolecular organization in the form of double chains (Figure 3.6). Each single molecule is characterized by a bright protrusion associated with the electron rich phenyl ring. The supramolecular chains are present in two different growing directions, rotated by $(69 \pm 2)^\circ$ clockwise (CW) and counter clockwise (CCW) from the $[1\bar{1}0]$ substrate direction, respectively. Since the inherent chirality of the molecule forbids the creation of its mirror image with all random adsorption events, no mirror chiral motifs can be conceived by flipping the molecular chirality to create the opposite enantiomer. Therefore, the presence of mirror symmetric growing directions for the double chains is better described by different configurations of the functional groups around the chiral atom. In order to get a first insight into the most stable molecular configurations in gas phase we have performed molecular dynamics simulations, briefly described here.

Classical MD simulations

Classical MD simulations were performed by Giulia Tomba from the King's College London (UK) on series of up to 8 L-Phe molecules in order to investigate the bonding schemes which could lead to the observed supramolecular structures. The Generalized Amber Force Field (GAFF), as provided in AMBER 8 [62], was used throughout the simulations (see Section 2.2.5). No restraints were applied on the molecules. Since AMBER does not allow to model metal surfaces, we introduced in first approximation a fictitious surface consisting of benzene molecules. Obviously, this molecular 'carpet' is not able to reproduce neither the chemical effects, nor the binding specificity of the real surface. However, it provides a sterical hindrance to the molecular mo-

tion in 3D. A series of simulations finally lead to a bonding scheme that resembles the double chains observed experimentally (Figure 3.6). Each L-Phe molecule is able to interact with an opposite, antiparallel molecule through both the carboxylate and amino functionalities, while equivalent lateral interactions are established with nearby, parallel molecules at each of its sides. Four H bonds at a $\text{NH}_2 \cdots \text{OOC}$ distance of 1.7\AA are encountered for each molecule in the chained structure. This intermolecular $\text{NH}_2 \cdots \text{OOC}$ distance is in agreement with the H-bond length of aminoacids in the solid state [63]. The model of the molecular chains obtained for gas phase was then superimposed on a modeled Cu(110) surface taking into consideration the adsorption conformation obtained by RAIRS and the geometrical parameters measured by STM, Figure 3.6b. Importantly, we assume preferential on-top bonding to the Cu surface by both oxygens and the nitrogen (Figure 3.7 g). This adsorption geometry with two anchoring points is generally found for amino acids on Cu(110) [6, 61], as reproduced schematically here for Glycine (Figure 3.7 a, b) and Alanine (Figure 3.7 c-f). The final model of the double chains is in full agreement with the adsorption geometry found by RAIRS measurements (Figure 3.4g). We note that although the bonding scheme obtained for gas phase could be conserved on the metal surface, the condition of preferential on-top binding of the carboxylate and the amino groups causes an increase in the intermolecular H-bonds lengths ($\text{NH}_2 \cdots \text{OOC}$: 2.1\AA between two antiparallel molecules and $\text{NH}_2 \cdots \text{OOC}$: 3.4\AA for molecules interacting laterally along the growing direction, see Figure 3.6b, c). Considering that H-bonds are expected to be strong for H-acceptor distances, $\text{H} \cdots \text{A} < 2.2\text{\AA}$ [63], the $\text{NH}_2 \cdots \text{OOC}$ interaction at a distance of about 3.4\AA found for molecules along the growing direction is likely to be too weak to determine the lateral interaction and orientation of the chains. However, for the superposition on the STM data, molecules in an unrelaxed configuration were used under the condition that functional moieties reside on high-symmetry positions. A possible conformational adaptation could reduce the bond length significantly. On the other hand, it is feasible that under the influence of the surface the H bond is stretched to allow commensurability with the substrate atomic lattice [64]. On the other hand, Cu(110) is an ‘open’ surface with a high density of adatoms that are expected to play a central role in the deprotonation of organic molecules and also in complexation reactions [65]. Therefore, in an alternative model (not shown) we have tried to incorporate such possible adatoms coordinating the molecular chains. The distances and geometry resulting from this

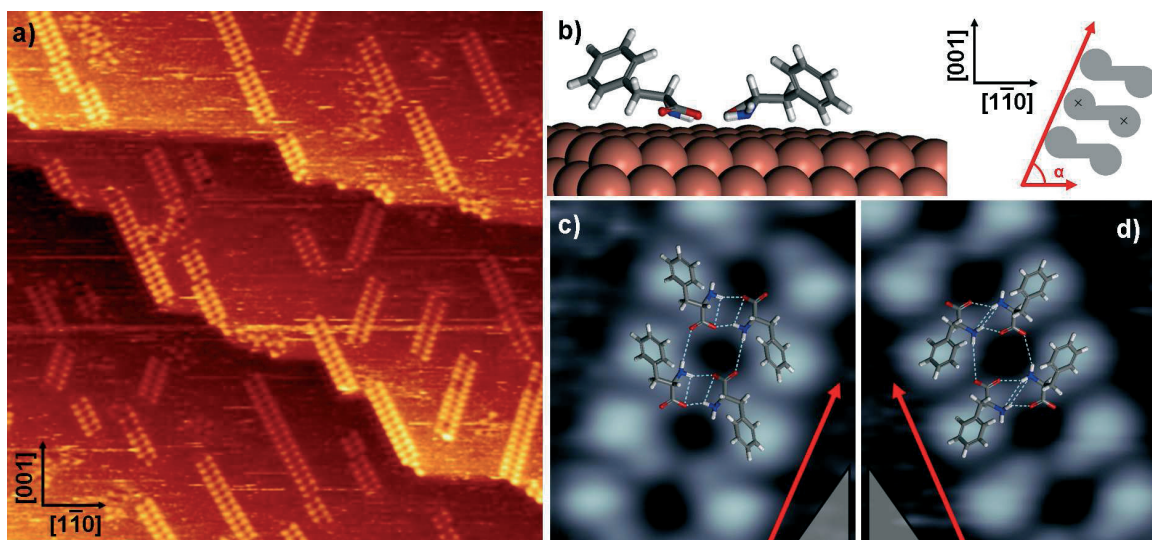


Figure 3.6: Supramolecular chains of L-Phe on Cu(110) . a) STM image of the double chains observed after annealing to 400 K (50×50 nm), c), d) High resolution STM image (4×3 nm) of the different adsorption motifs and superimposed schematic model. The model c) is based on MD simulations, $\alpha = 69^\circ$ CCW, the model in d) results from c) plus a rotation of the amino group around the carbon atom $\alpha = 69^\circ$ CW. b) lateral view of the model proposed in c). The dashed lines in c and d indicate potential H-bonding. The triangles indicate mirror-imaged footprints.

model were not compatible with the metal-organic coordination bonds for carboxylic acids on Cu(110) [65]. Moreover, the fact that in the STM images only few molecules seem to attach to the step edges provides an indirect proof of the absence of metal organic coordination. Interestingly, the phenyl rings are observed to align in a parallel staggered configuration during the MD simulation. This configuration is also conserved in the tentative model superimposed on the STM picture (Figure 3.6c) where the center to center distance of neighboring Phe rings (associated with the brightest center in the protrusions in the STM pictures) amounts 7.1Å. Therefore, in our model, $\pi - \pi$ interactions are likely to contribute to the alignment of the supramolecular structures along the growing directions, as normally found for biological systems containing aromatic substituents, like proteins and medicinal agents [66].²

²For the parallel staggered configuration, $\pi - \pi$ interactions are optimized if the center to center distance R_{cen} is in the range 3.5-7.5Å along the off normal angle θ , maximized for $\theta=30^\circ$ [66]. In our model θ is about 40° and $R_{cen}=7.1\text{\AA}$

Molecular chirality vs. Footprint chirality

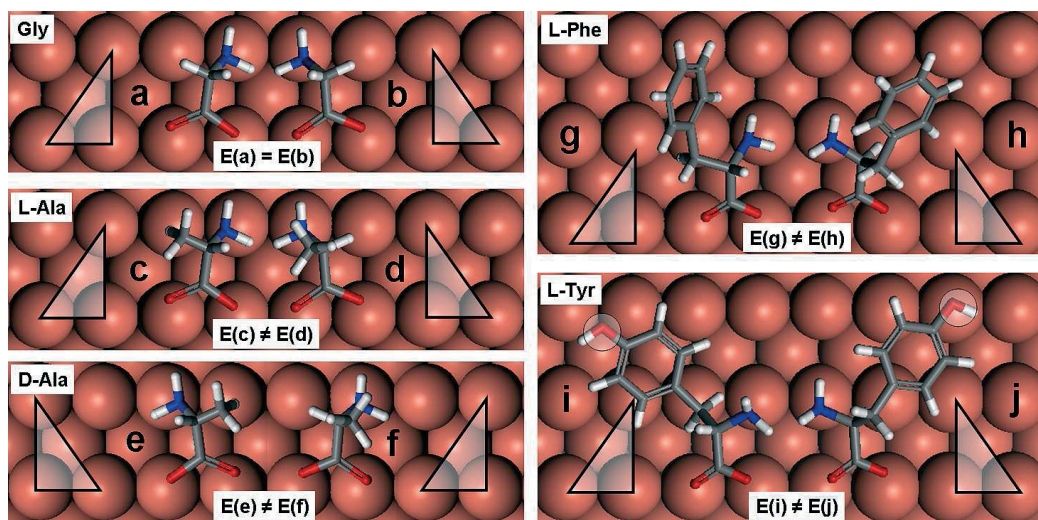


Figure 3.7: Molecular Chirality and footprint chirality, adapted from [59]. a), b) Chiral adsorption motifs for Glycine. c) and d) Chiral adsorption motifs for L-Alanine created by rotation around the chiral carbon. Note that the molecular chirality is the same for c), d) but the footprint chirality of c) is the mirror image of d). Thus, the presence of the methyl group causes the two motifs to be energetically inequivalent with the energy of adsorption $E(c) \neq E(d)$. e), f) Chiral adsorption motifs for D-Alanine created by rotation around the chiral carbon. Note that the molecular chirality is the same for e) and f) but the footprint chirality of e) is the mirror image of f). Thus, the presence of the methyl group causes the two motifs to be energetically inequivalent with the energy of adsorption $E(e) \neq E(f)$. The symmetry of the chiral adsorption motifs of L- and D-Alanine are such that $E(c) = E(e)$ and $E(d) = E(f)$. g), h) Chiral adsorption motifs for L-Phe created by rotation around the chiral carbon. Note that the molecular chirality is the same for g) and h) but the footprint chirality of g) is the mirror image of h). i), j) Chiral adsorption motifs for L-Tyr created by rotation around the chiral carbon. Note that the molecular chirality is the same for i) and j) but the footprint chirality of i) is the mirror image of j). Only j) is experimentally observed.

Two main chiral aspects can be identified for adsorbed motifs on metal surfaces: the chirality of the adsorbate (molecular chirality) and the chirality of the footprint delineating the bonding positions at the surface (footprint chirality) [6]. In the case of the amino acids Glycine, Alanine and Phenylalanine on Cu(110), the preference for on-top bonding by both oxygens and the nitrogen leads the molecules to adopt chiral triangular footprints at the surface (Figure 3.7a, b). Although DFT calculations for this systems (Alanine [6] and glycine [61]) show that some displacement away from the

on-top sites can occur, the bridge-site is never occupied by any of the bonding atoms, thus eliminating the possibility of projecting a symmetric triangular footprint at the surface. For the only achiral amino acid, Glycine, the two interchangeable hydrogens on the central carbon cause either motif to be equally likely. Note that both the molecular chirality and footprint chirality of (a) are the mirror image of (b). Thus, the two motifs are energetically equivalent with the energy of adsorption $E(a) = E(b)$. For Alanine (Figure 3.7c-f) and Phe (Figure 3.7g, h), the inherent chiral centre is preserved upon adsorption and there is no way of flipping the molecular chirality to create the opposite enantiomer, so adsorption of pure enantiomers will always result in an adlayer that is molecularly homochiral. However, the footprint chirality can potentially be reversed, either by rotation of functional groups around the chiral atom, or by rotation of the adsorbate on the surface so that the N atom occupies the adjacent on-top site. In the case of L-Alanine (Figure 3.7c, d) it should be noted that either footprint can be adsorbed with the methyl carbon still held away from the surface, as expected from steric considerations. The non-equivalence of the methyl and hydrogen groups on the asymmetric carbon means that the different chiral footprints shown for a single enantiomer of L-Alanine (Figure 3.7c, d) or D-Alanine, (Figure 3.7e, f) are non-degenerate. However, the energy differences may be small as Alanine shows a polymorphic behavior where certain phases lead to the creation of a single preferred chiral footprint, i.e., there is direct chirality transfer from the molecule into the footprint of the adsorbed species (i.e., the phase possesses molecular homochirality and footprint homochirality), while other phases involve co-existence of both footprints (i.e., the phase possesses molecular homochirality but footprint heterochirality) [59]. Note that the symmetry of the chiral adsorption motifs of L- and D-Alanine are such that $E(c) = E(e)$ and $E(d) = E(f)$.

The same considerations may apply to the observed double-row motifs of L-Phe. In fact, the molecular double rows shown in Figure 3.6 d can be explained after a rotation of the amino group around the chiral center of the model shown in Figure 3.6 c and 3.7 g. A good agreement with the geometrical parameters measured by STM is obtained. Moreover, the same type of H-bonding described for the model shown in Figure 3.6 c is obtained for the model shown in Figure 3.6 d. However, more rigorous DFT calculations are needed to support the adsorption models shown in Figure 3.7g, h. Both triangular footprints are expected to have similar probability of formation, as their coexistence at

400 K would explain the mirror symmetric double rows observed by STM (Figure 3.6c, d). Note that the C_{2v} point-group symmetry of Cu(110) allows a 180° rotation in the plane around the $[1\bar{1}0]$ direction. Therefore, the molecules in antiparallel configuration forming the 69° CCW double chains present the same triangular footprint rotated by 180° (Figures 3.6c, 3.7g), while the 69° CW double chains are formed by the opposite triangular footprint, related to the previous one by a rotation around the chiral center (Figures 3.6d, 3.7h).

Following this considerations, it becomes clear that although any chiral molecule presenting two anchoring points to the surface will show chiral templation, footprint homochirality is reached only when the chiral center is prevented for azimuthal rotation. Hence, we can envisage that the introduction of a third anchoring point of the molecule to the surface would drive the expression of global footprint homochirality on the surface, as energetically similar chiral footprints would be forbidden by sterical reasons. In order to test this hypothesis, we have studied the adsorption of L-tyrosine (L-Tyr) by STM under comparable experimental conditions. The only structural difference between Phe and Tyr is the presence of the *para*-OH on tyrosine. After adsorption of L-Tyr on Cu(110) and annealing at 400 K, STM imaging indeed reveals supramolecular double chains growing only in one direction, rotated by $(33 \pm 2)^\circ$ clockwise (CW) from the $[1\bar{1}0]$ substrate direction (Figure 3.8). Further MD simulations in gas phase indicate that the same bonding scheme found for L-Phe seems to be valid also for L-Tyr molecules. When superimposing the model on a Cu(110) surface and applying the restrictions for preferential on-top bonding of the functional groups, we found that only one footprint would be favored on the surface (Figure 3.8b and 3.7i) since a rotation around the chiral carbon would necessary change the adsorption sites of the functional groups to configurations that are expected to be less stable (Figure 3.7 j). In particular, here the difference with the L-Phe case is given by the extra oxygen atom which also has a preference for an on-top binding site on the Cu substrate (Figure 3.7i). Consistently, the seek for on-top interaction of the *para*-OH group induce an increased intermolecular distance in the molecular backbone direction (Figure 3.8b) of the L-Tyr chains in comparison to the L-Phe chains (Figure 3.6c). Finally, for L-Tyr the main driving force for the approach on the growing direction is most likely H-bond $NH_2 \cdots OOC$ at a distance of about 2.3 \AA and also here, $\pi - \pi$ interactions (final distance from the centers of neighboring Phe rings: 6.3 \AA , Figure 3.8b) are likely to play an important role on the

directionality of the supramolecular structures .

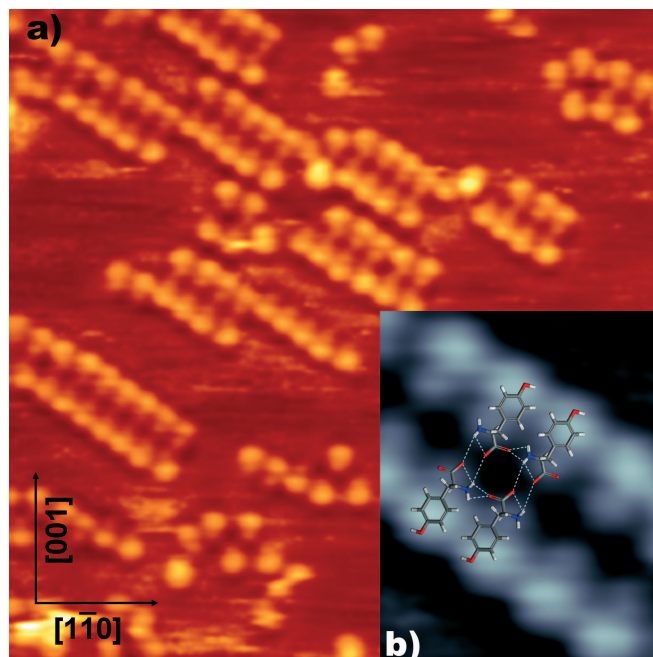


Figure 3.8: Supramolecular chains of L-Tyr on Cu(110). a) STM image of the double chains observed after annealing at 400 K (19×19 nm). b) High resolution STM image (4×3 nm) of the different adsorption motifs and superimposed schematic model based on MD simulations. The dashed lines indicate potential H-bonding.

Concluding remarks

In conclusion, our results show that the aminoacids L-Phe and L-Tyr adsorb on Cu(110) forming double chains at 400 K at sub-monolayer coverages. The structures are associated to adsorption models where the molecules bind to the copper surface in an anionic form, via the oxygen atoms of the carboxylate (COO^-) functionality and the nitrogen of the amino (NH_2) group. Both carboxylate oxygen atoms are found to be equidistant from the surface (RAIRS measurements, Section 3.2). It is shown that while L-Phe presents two different chiral footprints at 400 K (as also informed for Glycine and Alanine [59]), only one adsorption footprint is favored for L-Tyr, leading to the expression of footprint homochirality. This difference in behavior for L-Tyr is attributed to the

structural rigidity of the molecular motif created after adsorption that foreclose rotation around the chiral center. We note that a similar behavior was found for the amino acid Proline, in which intrinsic structural rigidity due to the presence of a pyrrolidine ring force the molecule to adopt the same footprint at the copper surface, even at different coverages and adsorption temperatures [52]. Finally, we note that a defined mode of interaction with the metal surface must play an important role in the use of amino acids as chiral modifiers in, for example, heterogeneous diastereoselective catalysis, where its attachment to an organic molecule determines the adsorption and orientation adopted by the latter at a surface, thus creating a strong inequality in the probability of hydrogen addition at the two prochiral faces of the reactant [6]. We emphasise that this is just the first stage towards a fundamental understanding of templating effect of aminoacids that could be potentially used for enantioselective catalytic processes. A more complete picture requires a step-by-step elucidation of how molecule-molecule and molecule-surface interactions and conformational changes are affected by the chemistry and the symmetry of the surface and the molecule.

Chapter 4

On the Mechanism of Chiral Recognition

Specific molecular recognition depends on the precisely defined arrangement of atoms in complementary structures interacting by short range forces [67, 68]. Fifty years of crystallographic and Nuclear Magnetic Resonance (NMR) data on the active site of several enzymes show that the unbound ‘initial’ state and the bound ‘final’ state (after interaction with a substrate¹ molecule) present a different structural shape. This demonstrated that the mutual interactions between complementary molecules can result in their recognition even if their static molecular structure is not optimized for specific binding [68, 69, 70]. On this basis, the mechanism of dynamic *induced fit* originally introduced by Pauling in 1948 [68] and developed by Koshland for enzymatic activity [71] is today the generally accepted picture in biomolecular recognition processes [72].

Dynamic mutual conformational adjustments should also be important in chiral recognition, i.e. the discrimination of stereoisomeric molecules. However, no experimental studies have so far addressed the issue of tracking the conformational dynamics of interacting enantiomers at the single-molecule-level, and chiral recognition is mainly discussed within the static three-point-model [10] adapted from Fischer’s lock-and-key picture [67, 8].

¹Substrate is used in biology to define the target molecule that interacts with the enzyme and should not be confused with the term ‘substrate’ that we use in surface science to refer to metallic and semiconductor surfaces.

In the previous chapters we have presented a description of the adsorption motifs of L-Phe and L-Tyr on Cu(110). Those structures can be considered to be ‘final states’ at a given temperature, being therefore 2D analogous of the 3D crystal structures. In the present chapter we finally explore the mechanism of chiral recognition, tracking all the way from the ‘initial state’ (one isolated adsorbed molecule) to the ‘final state’ (the supramolecular structure) by means of state-of-the-art experimental and theoretical analysis. The interaction among individual di-D-Phe (D-Phe-D-Phe) molecules and the discrimination of D-Phe-D-Phe from its enantiomer L-Phe-L-Phe on Cu(110) is followed by STM and rationalized using first principles and classical molecular dynamics calculations. We find that the stereoselective assembly of adsorbed D-Phe enantiomers into molecule pairs and chains takes place through mutually induced conformational changes, thereby illustrating at the single molecule level the more than half a century old prediction of Pauling.

Chiral recognition of adsorbed Di-phenylalanine on Cu(110)

4.1 The molecule-substrate system

The Phe-Phe dipeptide constitutes a key motif in molecular recognition for many biological processes. It is present in the cytosolic tail of several proteins of putative cargo receptors, being involved in the recognition of cargo molecules for transport between cellular organelles [73]. Furthermore, it constitutes the core of the beta amyloid polypeptide having a central role in amyloid fibril formation that leads to many diseases, as Parkinson, Alzheimer, prion, etc. [74]. Reches and Gazit recently succeeded in demonstrating that this dipeptide contains all the molecular information needed to mediate the self-assembly of well-ordered peptide nanotubes [74].

From the functional point of view, the D-Phe contains two chiral centers (asymmetric carbons) linked through a central amide bond (Figure 4.1a). The two electron-rich phenyl rings make it possible to visualize the single molecules by STM. As discussed in the previous chapter, the carboxylic and amino functional groups are well known for intermolecular recognition and self assembly and for the adsorption onto the Cu(110) surface [6, 75].

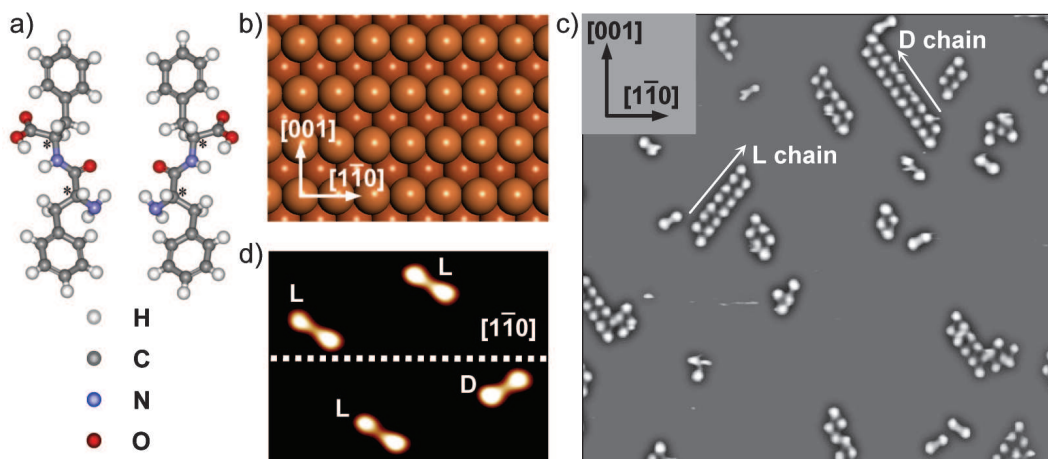


Figure 4.1: a) Schematic drawing of L-Phe-L-Phe(right) and D-Phe-D-Phe(left) molecules. The asterisks show the asymmetric carbons. b) Ball model of the Cu(110) surface. c) STM image (36 x 34 nm) of co-adsorbed L-Phe-L-Phe and D-Phe-D-Phe on Cu(110) at room temperature. The arrows indicate the growth direction of the homochiral chains. L corresponds to L-Phe-L-Phe and D to D-Phe-D-Phe. d) STM image (8.3 x 6.4 nm) of individual D-Phe molecules showing that the two enantiomers are mutual mirror reflections with respect to a plane perpendicular to the surface through the $[1\bar{1}0]$ axis.

4.2 Integrated Experimental and Theoretical analysis

4.2.1 STM measurements

The samples have been prepared as described in Section 2.3.2. All the STM measurements presented in this chapter were performed at room temperature.

After co-depositing L-Phe-L-Phe and D-Phe-D-Phe on the Cu(110) surface (Figure 4.1b) at room temperature and low coverage, STM imaging reveals both single molecule adsorption and supramolecular organization in the form of homochiral chains. Each single molecule is characterized by two bright protrusions corresponding to the electron-rich phenyl rings and by a central dimmer part associated with the peptide backbone (high-resolution STM image Figure 4.1d).

As also observed on enantiopure-covered surfaces, the main axis through the center of the two phenyl rings of single L-Phe-L-Phe molecules is rotated 34° clockwise from the substrate direction, while for D-Phe-D-Phe it is rotated 34° counter clockwise (Figure

4.1d). The two enantiomers are mirror images with respect to planes perpendicular to the surface through the $[1\bar{1}0]$ axis and cannot be superimposed onto each other by rotation or translation.

The *molecular* chirality of the adsorbed molecules evident in Figure 4.1d indicates that their stereogenic centers are involved in the molecule-surface interaction [76, 77, 78, 79, 4, 11, 80, 81, 82]. The system shows also *supramolecular* chirality which results from the stereoselective self-assembly of two or more dipeptides in homochiral chains (Figure 4.1c).

The main molecular axis of the single molecules rotates by further 40° upon assembly, and is thus oriented at -74° from the $[1\bar{1}0]$ direction for the L-Phe-L-Phe chains and at $+74^\circ$ for the D-Phe-D-Phe ones. Stable heterochiral chains are never observed, indicating a highly stereoselective supramolecular process. Further insight into the molecular configurations and binding modes is obtained via the first principles (FP) and classical molecular dynamics (MD) modeling discussed in the next section.

4.2.2 Computational methods

All the theoretical modeling was done in collaboration with Giulia Tomba from the King's College London (UK), the Center of Excellence for Nanostructured Materials (CENMAT) and INFM-DEMOCRITOS National Simulation Center in Trieste (Italy).

The modeling of a peptide system is challenging due to the presence of several functional groups with many degrees of conformational flexibility. The Cu(110) substrate is known to interact quite strongly with the carboxylic and amino moieties of organic molecules, and a similar interaction can be expected for the peptide oxygen. The same functional groups, though, are fundamental in establishing intermolecular bonds, which means that the stability of the final structures is ruled by a subtle equilibrium among competing interactions. The delicacy of the system calls for information at the atomistic level which can only be accessed by a combination of experimental methods and computer simulations. We addressed the problem by a set of molecular dynamics techniques up to the quantum accuracy level, focusing on both the fundamental binding modes between molecule and substrate, and the molecule-molecule interactions.

In the following, we summarize the many steps of the calculation scheme (for the molecule in gas phase and on the metal substrate) that was implemented to obtain

the final model. The classical force field simulations are much less expensive from a computational point of view and allow to span the configurational possibilities of a system quite quickly and easily: they are often successful when the investigations only require an accurate description of van der Waals and electrostatic interactions, including hydrogen-bonds. This kind of approach was used at the beginning of this study in order to obtain a model for the possible molecular configuration. The model was then refined through quantum mechanical techniques (FPMD, First Principles Molecular Dynamics). *Ab initio* simulations become mandatory to investigate the role of the surface and to get the necessary energetic details. A very punctual description of the calculations can be found in [44].

Preliminary study : Molecules in the gas phase

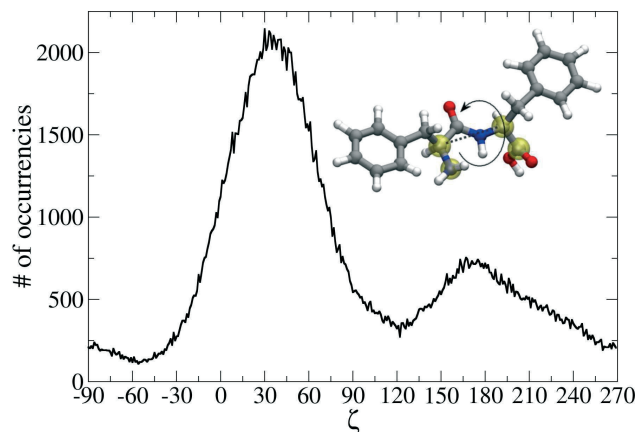


Figure 4.2: Distribution analysis for the torsional angle ζ , defined by the 4 atoms highlighted in yellow in the sample C conformation (upper right corner). Data refer to a classical MD simulation in gas phase at 400K.

As described in the previous chapter for amino acids, also the charge state of peptides strongly depends on the surrounding environment. Solvated molecules exist in neutral, ionic or zwitterionic form, depending on the pH of the solution, whereas neutral groups are energetically favoured in gas phase. To sample extensively the phase space of the

molecular conformations accessible to Phe-Phe in vacuum, we followed the dynamics of a neutral molecule during a 5 ns classical MD simulation at 400 K. The high flexibility of the molecule, which is limited only by the inherent planarity of the peptide core, (i.e., the central CONH group) allows it to access a wide range of conformations. These can be discriminated according to the relative position of the two most important interaction sites, i.e. the -COOH and NH₂ groups, as quantified by the torsional angle ζ (see insert in Figure 4.2). The distribution of ζ during the dynamics presents two peaks, centred at about 35° and 170° and separated by two minima at about -50° and 125° (Figure 4.2). Within the first peak, both the carboxyl and the amino groups are located on the same side with respect to the molecular backbone. Elsewhere each side of the molecule hosts only one reactive functionality. We will refer to the two conformations as ‘C’ and ‘S’, respectively. As highlighted by the distribution profile in Figure 4.2, the molecule preferentially adopts the C conformation (66% of the total simulated time).

First principles molecular dynamics

The calculations were performed in the DFT theoretical framework. In most cases it was used the GGA (Generalized Gradient Approximation) form for the exchange-correlation energy term of the functional. This kind of approximation has been observed to account better for interactions among molecules such as hydrogen bonds, but it tends to underestimate the interactions with surfaces. The LDA (Local Density Approximation) form, on the opposite side, tends to overestimate this contribution. The GGA approach, though, is known to give a more realistic account of energy barriers and adsorption behavior of molecules on metal or semiconductor surfaces, hence it is overall a better choice for our system.

During the simulation, the isolated dipeptide in the C conformation binds to the Cu(110) surface via the nitrogen atom of the amino group, one oxygen of the carboxyl group, and the oxygen of the carbonyl group (Figures 4.3a and 4.3c). These bonds are estimated to contribute by 47%, 23% and 30%, respectively, to the 1.57eV calculated molecule-surface interaction energy. This three-point binding mode is frequently observed in analogous systems [83, 84]. In the optimized molecular geometry the angle between the molecular axis and the direction $[1\bar{1}0]$ is about 32°, in good agreement with the measured value (Figure 4.3e).

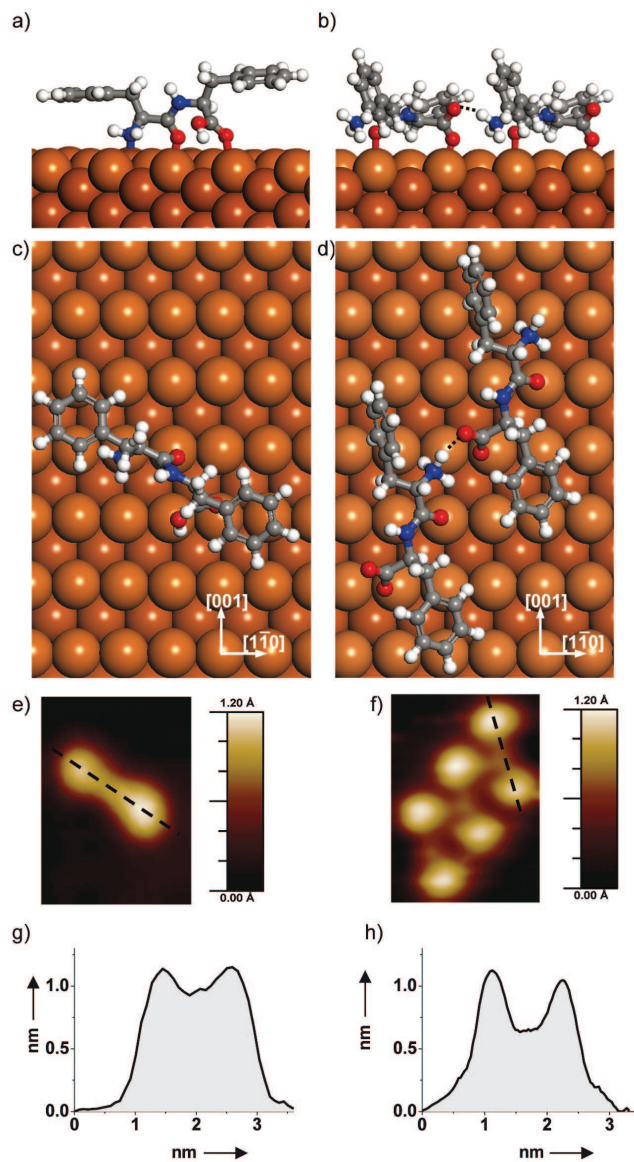


Figure 4.3: a), c) Minimum energy structures of an isolated L-Phe-L-Phe dipeptide adsorbed on Cu(110) obtained in DFT simulations. The carboxylic and the amino groups are located on the same side with respect to the molecular main axis (conformer C). b), d) Adsorption geometry of L-Phe-L-Phe dipeptides organized in homochiral chains by formation of strong intermolecular hydrogen bonds and proton transfer between the molecules. The carboxylic and the amino groups are located on opposite sides with respect to the molecular axis (conformer S). e), f) representative high resolution STM images of an isolated L-Phe-L-Phe molecule and of L-Phe-L-Phe molecules in a chain, respectively. The main molecular axes are indicated by black dashed lines. g), h) corresponding height line scans through the main molecular axes.

By contrast, calculations on the adsorbed isolated molecule in the S conformation predict a 0.5 eV lower interaction energy at an orientation of about -14° (Figure 4.4c), which is never observed in the STM images. This difference in energy is mainly due to the substrate contribution, since the surface needs to be far more strained in order to adapt to the molecule in S conformation.

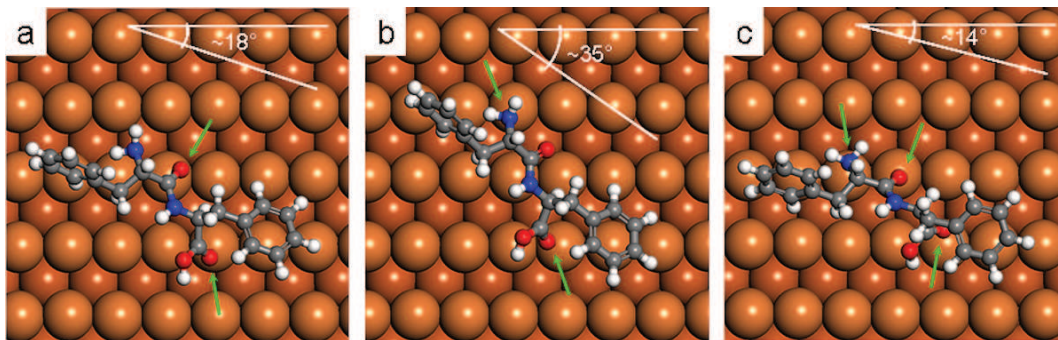


Figure 4.4: (a,b) Input models for two separate FPMD simulations of an isolated Di-L-Phe molecule adsorbed on Cu(110) in the S conformation. In either case the molecule was initially placed on the surface so that at least two favorable ‘on top’ adsorption sites could be preserved (green arrows). Both simulations led to the same relaxed structure (c) after the molecule reoriented itself in order to reach a 3-point adsorption configuration. Although the sites of adsorption are exactly the same as for the isolated molecule in C conformation (Figure 4.3c), the calculated adsorption energy for the S conformer is $\sim 0.5\text{eV}$ lower than for the C conformer due to an increased surface strain. Moreover, the molecular orientation with respect to the substrate does not match the experimental value of about 34° .

The formation of hydrogen bonds between the carboxyl and the amino groups of different Phe-Phe molecules may lead to several kinds of supramolecular assemblies depending on the relative molecular conformations. In particular, two molecules with C conformation would saturate their functionalities by forming a closely bound molecular pair, while molecules with S conformation could assemble in linear structures of arbitrary length. Indeed, in a classical gas-phase MD simulation, we observed a series of nine L-Phe-L-Phe molecules bound to each other through the carboxylic and amino moieties forming a stable, open-ended chain. We thus performed an *ab-initio* gas-phase MD simulation placing a single S molecule in a periodically repeated cell with the translational symmetry of the Cu(110) lattice. A stable hydrogen bond between the carboxyl group of the molecule and the amino group of its adjacent periodic image forms during

a 590 fs damped dynamics simulation. This bond ensures the stability of the ‘infinite’ periodic chain of neutral molecules. The calculated bond energy is -0.43 eV with respect to a relaxed isolated molecule.

In order to confirm this classical results and to get more information about the influence of the surface on the final supramolecular structure, we performed a new *ab-initio* simulation where the relaxed gas-phase chain structure was positioned on the surface. Consistent with the adsorption mode of single molecules described above, we initially assigned to the oxygen atoms of the carboxyl and carbonyl groups nearly ‘atop’ positions with respect to surface Cu atoms, which resulted in an initial adsorption angle tilted by -58° with respect to the $[1\bar{1}0]$ surface direction. From the initial to the final configuration the molecule undergoes a substantial rearrangement characterized by a shift of the adsorption angle to -74° (Figure 4.3d), in agreement with the value $(-74 \pm 4)^\circ$ measured with STM, Figure 4.3f. Interestingly, during the dynamics the peptide carbonyl oxygen is observed to slide from one surface adsorption site to the next along the crystallographic direction, suggesting a smooth potential energy surface for diffusion along this direction. At the same time, the amino group approaches the substrate, while maintaining the hydrogen bond with the nearby carboxylic group throughout the trajectory. Furthermore, we observed spontaneous proton transfer from the carboxylic group of the molecule to the amino moiety of its neighbor along the chain, yielding a chain of zwitterions. Forcing the H atom back to the carboxyl group resulted in a 0.45 eV increase of the total energy of the system, suggesting that the stable chemical state of Phe-Phe molecules forming supramolecular chains is indeed zwitterionic (the DFT simulation showing the spontaneous proton transfer between the carboxyl and the amino groups of adsorbed Phe-Phe can be found in the video V1 in Supporting Information). In the final chain structure, the adsorption energy per molecule is 1.16 eV, i.e. 0.41 eV less than in the stably adsorbed isolated C molecules. Since the calculated energy gain associated with the formation of a chain of neutral molecules is only 0.43 eV (see above), the observed proton transfer event may be essential to provide a net thermodynamic driving force for the formation of stable molecular chains (Figures 4.3b and 4.3d).

To gain further experimental evidence that support this model we have performed XPS and NEXAFS measurements. As it will be discussed in the next Chapter, XPS data are consistent with a zwitterionic charge state of the assembled Phe-Phe molecules. The NEXAFS and XPS data were taken at the HE-SGM beamline at BESSY II in Berlin

in collaboration with Thomas Strunskus and Christof Wööl from the Ruhr-Universität Bochum, Germany.

NEXAFS

The structural details of the supramolecular chains were investigated by NEXAFS spectroscopy after deposition of Phe-Phe at a coverage of about 1 ML, at which most of the molecules are assembled into chain structures. For the NEXAFS measurements the partial electron yield mode with a retarding voltage at the carbon K edge of 150 eV and at the nitrogen K edge of 300 V was used. All spectra were recorded at room temperature and referenced against a characteristic peak in simultaneously recorded spectra of a contaminated Au grid. For each incidence angle an average of two spectra is presented. The spectra of the C1s edge (Figure 4.5 a) show two π^* resonances (A and B) and two broad σ^* features. The first one (peak A in Figure 4.5a) is attributed to the lowest lying phenyl resonance [85, 86] while the second one (peak B in Fig. 6a) consists of a mixture of higher lying phenyl resonances and will therefore not be taken into account in the analysis below. The N1s edge features a single π^* resonance (labeled A in Figure 4.5b) stemming from the amide subunit (CONH) [87]. The spectra for both C and N show a distinct dependence on the radiation incidence angle β (see Figure 4.5, inset), which in our experiments was set to 30°, 55° and 90°. The intensity variations measured by NEXAFS are directly related to the geometrical features of the system, since each molecular resonance scales with the angle between the corresponding transition dipole moment and the radiation incidence direction. Starting from a known structure, the relationship between these values can also be used to derive a corresponding expected trend for $I(\beta)$ [37]. We applied a similar procedure to our DFT-derived adsorption geometry in order to check the consistency of our model with the experimental data. The averaged intensity curves corresponding to the two phenyl rings are reported in Figure 4.5 c, while the intensity curve for the amide group is shown in Figure 4.5d (solid lines). In order to investigate the angular sensitivity of the method, two further theoretical curves (dotted lines) were calculated for adsorption angles which differ by 10° with respect to the equilibrium geometry. The normalized experimental intensities (crosses) are in good agreement with the data derived from the equilibrium structure, clearly providing the best fit among the three curves.

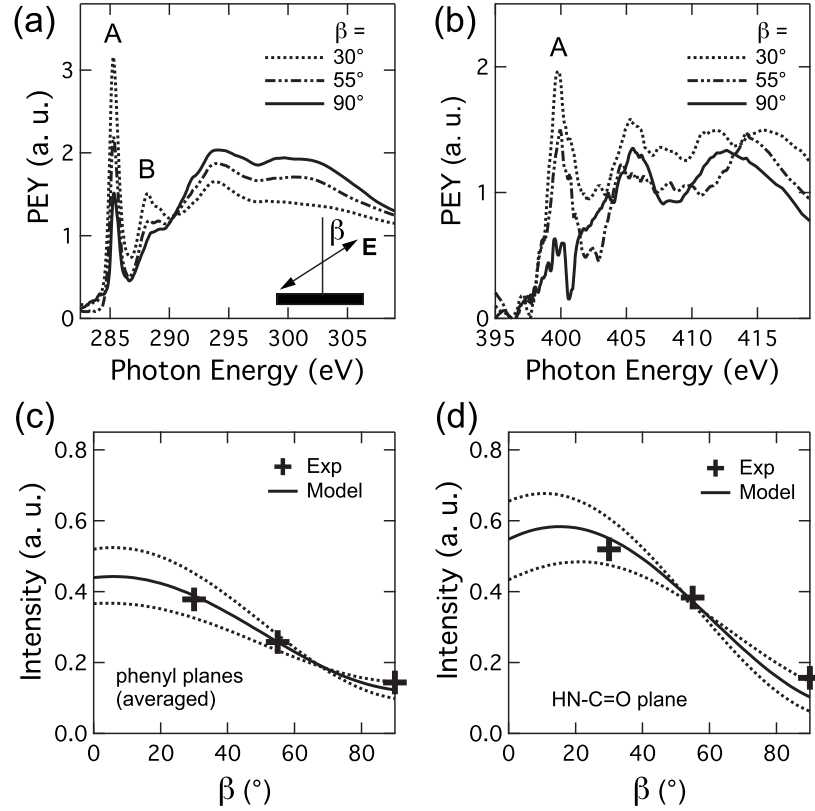


Figure 4.5: NEXAFS spectra of the C1s edge (a) and of the N1s edge (b) of chains of D-Phe-D-Phe and the comparison between the theoretical prediction (solid line) and the experimental intensities (crosses) for the average of the phenyl planes (c) and the amide plane (d). The two further theoretical curves (dotted lines) were calculated for adsorption angles which differ by 10° with respect to the equilibrium geometry. The higher level of noise in the nitrogen data is due to an unstable detector background.

The induced fit mechanism at the single molecule level

A detailed analysis of the structural models also reveals that the rotation of the molecular axis observed by STM after the assembly is only the most evident consequence of a more complex conformational rearrangement of the dipeptide molecules. Namely, to form supramolecular chains the monomers need to switch from the C to the S conformation while the oxygen atoms of the adsorbed functional groups change their relative positions along the direction (cf. Figure 4.3c and 4.3d). At the same time, the process involves a rotation of the inherently planar peptide backbone, so that the initially upright NH group (Figure 4.3a) flattens down towards the substrate. A direct experimental evidence of this conformational change is given by high-resolution STM images. A statistics over more than 100 molecules shows that the peptide backbone of isolated molecules appears almost twice as high (height = 96 ± 8 pm, Figure 4.3e and 4.3g) as the backbone of molecules arranged in chains (height = 55 ± 6 pm, Figure 4.3f and 4.3h).

The switch between molecular conformations described above implies that the process of chain formation does not result from a mere juxtaposition of molecules, as expected within the static ‘lock and key’ [10] picture of the three-point model [79, 11]. To attain a more detailed dynamic description of the chiral recognition phenomenon we have tracked with STM the conformation and orientation changes that two D-Phe-D-Phe molecules undergo while they approach and attempt to assemble (video V2 in Supporting Information). Eight snapshots from this video, corresponding to the observed formation path of a homochiral pair are displayed in Figure 4.6.1a to h. A quantitative representation of the relative molecular motion is obtained by plotting the distance between the uppermost phenyl rings of each molecule as a function of the elapsed time (graph in Figure 4.6.1)².

The STM video V2 starts with two isolated molecules of D chirality (Figure 4.6.1a). After meeting, they experience a first change in the adsorption geometry forming an initial pair (Figure 4.6.1b). This complex is not in the optimal configuration, and undergoes several further rearrangements (Figures 4.6.1b to g) until the final state corresponding to the stable pair is reached (Figures 4.6.1g and h). The molecular arrangement within this structure is identical to that observed in longer homochiral

²We have used a self-written maximum location algorithm in order to eliminate arbitrariness in the distance measurements. The estimated error in reproducibility of the measured distance is 1%.

chains (Figure 4.1c), implying that stable pairs and not isolated monomers provide the basic structural unit which determines the supramolecular geometry. A careful analysis of the STM videos reveals that the central core becomes dimmer whenever the molecules adopt the $+74^\circ$ orientation. This suggests that the rotation of the main molecular axis is always associated with a C to S conformational switch of the adsorbed monomers, as previously described. A further analysis of the full video sequence confirms that these conformational changes are induced by the mutual intermolecular interaction since they occur only when two molecules are close enough to each other.

4.2.3 Stereoselectivity

To investigate the stereoselectivity of the recognition process, the dynamics of the interaction between two molecules with opposite chirality (a L-Phe-L-Phe and a D-Phe-D-Phe molecule) has been recorded in the video V3 and is shown in Figure 4.6.2. The distance between the two enantiomers is, on average, much larger than in the case of homochiral molecules and undergoes more pronounced oscillations (graph in Figure 4.6.2). Moreover, no stable pair structure is reached but only metastable heterochiral pairs form temporarily (Figures 4.6.2a', c' and d'). In these structures the two molecules assume the -74° and $+74^\circ$ orientations (for L-Phe-L-Phe and D-Phe-D-Phe, respectively) and the dimmer appearance of the peptide backbone indicates once again a C to S conformational switch between the two conformers as the result of their mutual intermolecular interactions. However, the different chirality of the two stereoisomers prevents their functional groups from reaching the optimal position for forming a stable electrostatic bond (Figure 4.7).

Metastable molecular pairs

As mentioned above, the process of molecular assembling is strictly stereoselective. Occasionally, heterochiral pairs can also be found in the STM images but their life-time is much shorter than for homochiral pairs. In addition, metastable homochiral pairs are also observed, mainly during the process of mutual recognition and assembling of two individual molecules. Examples of such metastable pair structures are reported in the insets of Figure 4.7. Their adsorption geometries are indicative of different intermolecular interactions, which reflect the presence of several functionalities in Phe-Phe. *Ab*

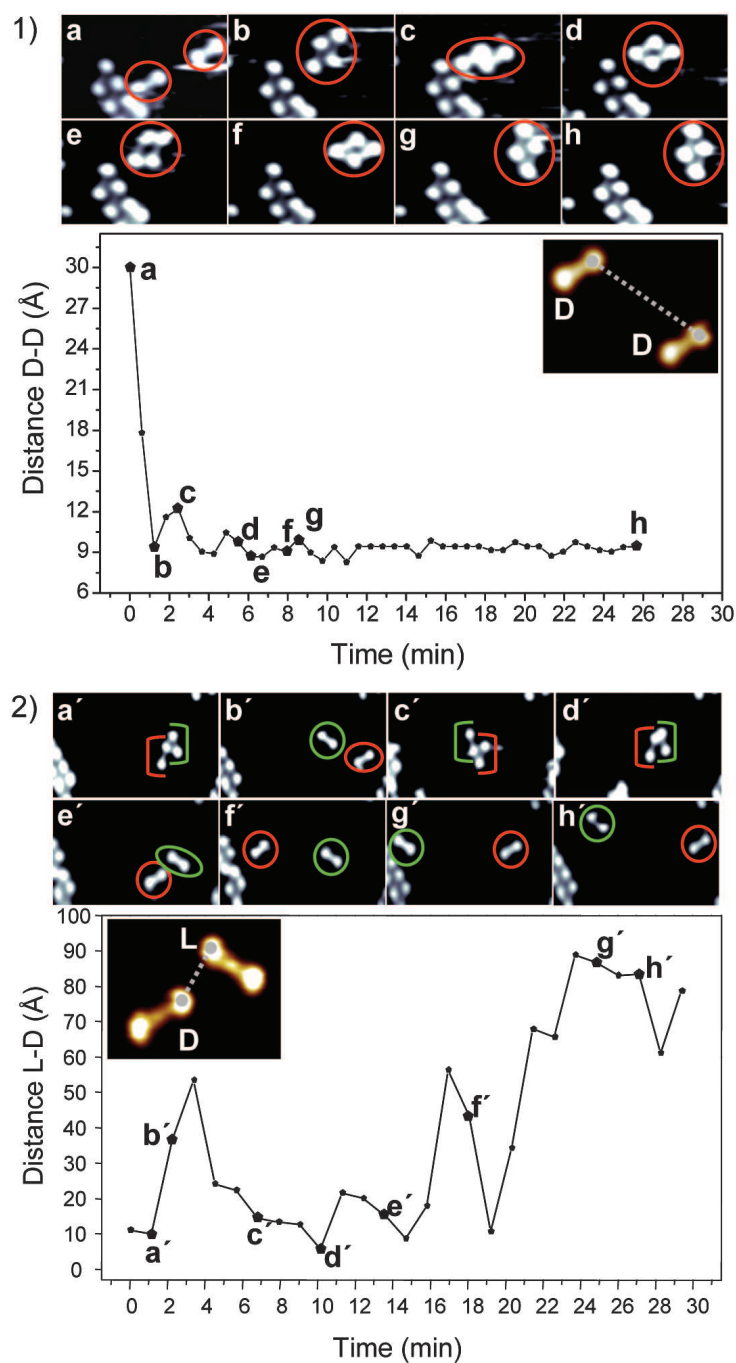


Figure 4.6: 1) Selected frames (a-h) of the STM video V2 (see the Supporting Information) showing the formation path of a homochiral pair of D molecules (in red circles). The final pair stays stable without further breaking or reorganization (from frame g to h). 2) Selected frames (a'-h') of the STM video V3 (see the Supporting Information) showing the evolution of the interacting heterochiral L-D pair (L in green circles, D in red circles). The full color scale corresponds to 1.33 Å. The corresponding graphs illustrate the relative molecular motion of the full videos.

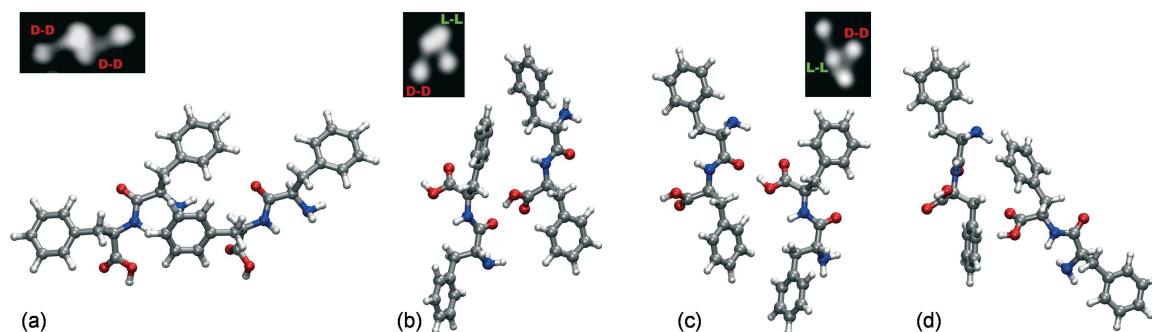


Figure 4.7: Pair structures obtained from classical MD simulations. Similar pairs observed in STM images are represented as insets. A range of molecule-molecule interactions is observed, from $\text{-NH}_2/\text{phenyl}$ or $\text{-COOH}/\text{phenyl}$ interactions (homochiral pair (a), heterochiral pair (d)) to hydrogen bonds between the carboxylic and carbonyl groups (b,c). MD classical simulations of both homochiral and heterochiral pairs were performed at temperatures up to 200 K, each for about 200 ps, after which the structures were relaxed to their 0 K equilibrium geometry.

initio simulations of such adsorbed structures would be computationally too demanding, but valuable insight into the binding modes can be provided by gas-phase classical MD simulations incorporating the information obtained with the DFT simulations described in the previous sections. Namely, relaxed *ab initio* configurations of adsorbed molecules were used as initial structures, and harmonic restraints were applied on the oxygen or nitrogen atoms in order to mimic the effect of the covalent bond to the surface adsorption sites. The initial relative distance and mutual orientation of the molecules were set to be commensurate with the Cu(110) substrate at the calculated stable adsorption angles. Since the presence of zwitterions is presumably associated with stable dimers or chains, only neutral molecules were considered here to simulate metastable pairs. The obtained molecular pair structures contain hydrogen bonds either between carboxyl and peptide carbonyl groups (Figure 4.7) or between peptide carbonyl and amino groups. Moreover, we repeatedly observe interactions between the amino or carboxylic groups and the phenyl rings, especially in the case of homochiral pairs. We note that cation- π interactions are known to promote inter- and intramolecular stabilization in biological macromolecules [88, 63].

4.2.4 Further growth of the supramolecular chains

In the previous sections, we have described the key steps for the chiral recognition between a pair of adsorbed dipeptides. Here, we follow the formation, growth and dissociation dynamics of several Phe-Phe chains by acquiring consecutive STM images on the same surface region (videos V4-V5 in Supplementary Information). Starting from a pre-existing pair (red circle in Figure 4.8.1a), the interaction with a third molecule (indicated by a red arrow in Figure 4.8.1) takes place initially with formation of a metastable trimer structure (Figure 4.8.1d-h). Later, stabilization of the interaction between the new molecule and its neighbor causes the temporary disruption of the initial pair (Figure 4.8.1i-j), eventually followed by the formation of a stable trimer (Figure 4.8.1k-l). A similar disruption event was also observed during the formation of a tetramer (Figure 4.8.2a-h). In this case, a fourth molecule approaches a pre-existing trimer and binds to one of its end molecules. This initially leads to separation into two dimers which only later join again to form a tetramer. Interestingly, the tendency of a newly approaching molecule to induce the breaking-up of the last bond in a chain is less frequently observed with increasing chain length. Namely, we never observed such an event for chains composed by nine or more molecules (Figure 4.8.3a-d), although we could sometimes observe that a longer chain loses spontaneously its last molecule. However, the spontaneous dissociation of homochiral dimers into separated molecules was never recorded in our experiments, pointing towards a very high stability of molecular pairs.

4.3 Discussion

On the basis of the presented results we can conclude that isolated neutral molecules adsorb from the gas phase on the Cu surface in the C conformation with the amino and carboxyl functional groups located on the same side with respect to the molecular axis. As shown by STM imaging, diffusion processes occur at room temperature, and lead to mutual interactions between single molecules. This results in their initial assembly into pairs and in the subsequent growth of longer chains by addition of single molecules to existing chains (see Figure 4.8.3). A conformation change in which the two functional groups move to opposite sides of the molecular axis (S conformation), accompanied

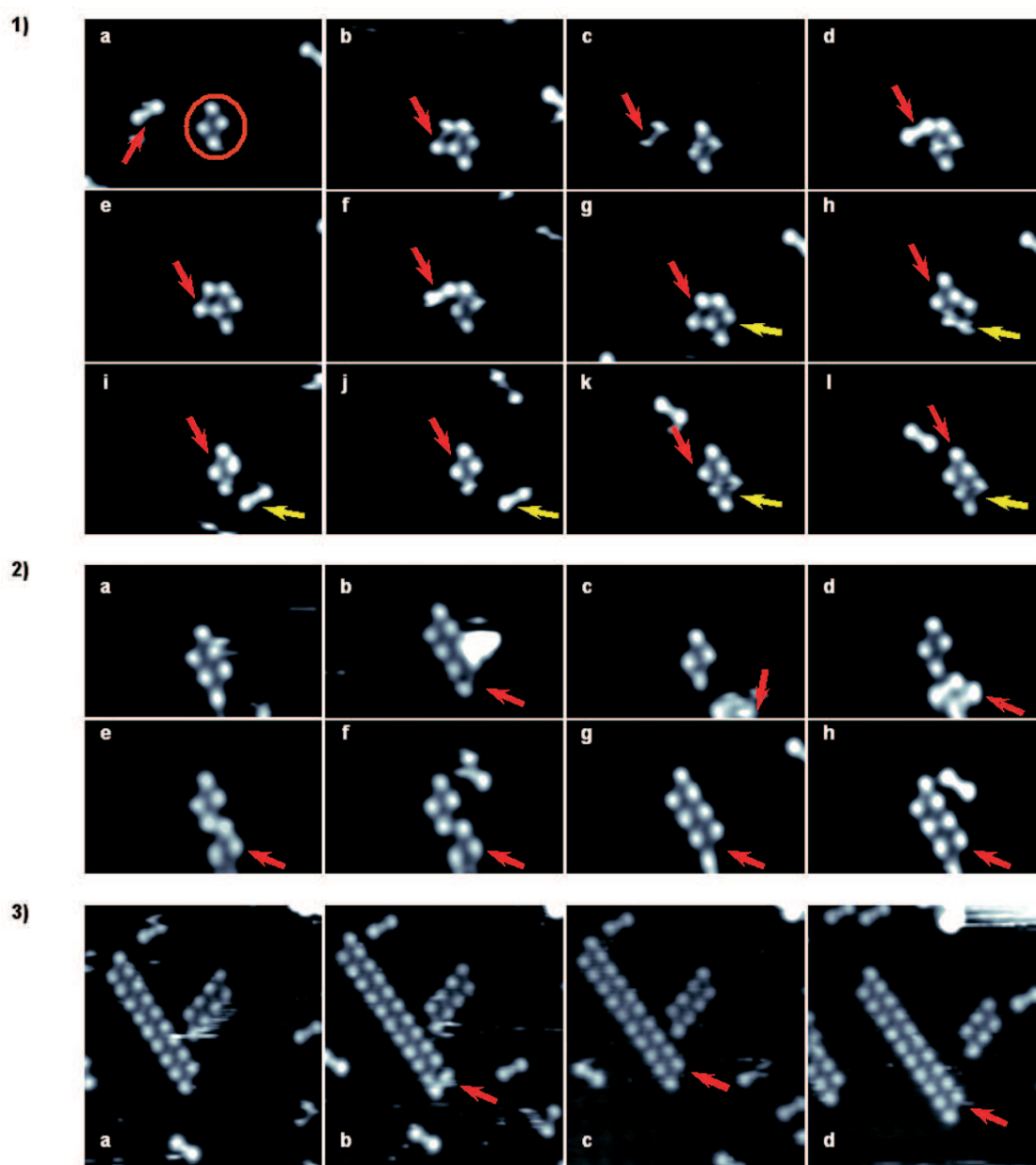


Figure 4.8: 1) Selected frames (a-h) of the STM videos V4 and V5 (see the Supporting Information) showing the formation path of a homochiral chain of D molecules as a third molecule approaches the initial pair (in red circles). Timescale (a=0, b=68s, c=136s, d=204s, e=340s, f=408s, g=680s, h=748s, i=816s, j=952s, k=1292s) 2) Selected frames showing the growth of a chain of 3 to 4 molecules. Timescale (a=0, b=68s, c=136s, d=408s, e=476s, f=1020s, g=1360s, h=1496s). 3) Selected frames showing the growth of a chain of 9 to 10 molecules. Timescale (a=0, b=68s, c=136s, d=3060s).

by a rotation of the molecular axis with respect to the surface, takes place during the formation of molecular pairs and chain growth. In this process, the CONH peptide core of the molecule moves from an orientation nearly perpendicular to one nearly parallel to the Cu surface. This is visible in the relaxed DFT models of adsorbed molecules and in the STM images, which show a higher STM signal intensity in the central backbone region of C molecules than in S molecules, Figure 4.3.

When single molecules assemble into chains, the hydrogen bond formation between the amino group of one molecule and the carboxyl group of the next molecule is accompanied by proton transfer, leading to a chain of zwitterions. In the chain geometry the molecular amino groups are no more covalently bound to the metal substrate, so that each molecule in the chain is significantly less bound to the surface than an isolated molecule. At the same time, a comparable energy gain is associated with the formation of the hydrogen bond between molecules inside the chain. If we assume that the chained molecules still bear neutral functional groups, the calculated values of these two energy contributions are 0.41 eV and 0.43 eV per molecule, respectively, virtually indistinguishable within an expected DFT error of about 0.1 eV. However, our results suggest that proton transfer can stabilize the chain structure by a further calculated 0.45 eV per molecule, thus providing the necessary driving force to form chains. From the energy results above, a lower limit to the energy barrier for the dissociation of a molecule from a chain can be estimated to be 0.47 eV. However, as described above, dissociation events are observed when a new molecule approaches a pre-existing dimer or trimer and interacts with one of their end molecules. The two molecules at the ends of each zwitterionic chain are expected to be in different chemical states than those located inside the chain. Namely, they can be in either a positively charged state (containing a NH_3^+ and a COOH group) or in a basic, negatively charged state (containing a NH_2 and COO^- group). When a terminal molecule of a chain binds to a newly added molecule, the proton transfer process changes its state from charged to zwitterionic. Its back bonding to the chain is expected to get weakened in this process, so that a temporary spontaneous breaking off of a dimer at a growing end of a chain is expected to occur, at least for short chain segments where the relatively low number of aligned molecular dipoles is not sufficient to electrostatically stabilize any further joining molecule directly upon addition [89].

During the assembling process, a reorientation of the molecules from a C to an S

conformation occurs as a result of mutually induced molecule-molecule interactions. For instance, during the formation of a homochiral dimer, a set of STM images taken in rapid succession on the same sample at room temperature shows that the two interacting molecules switch back and forth from the C to the S conformation (changing their adsorption angle from 34° to 74° and back) 3 times in about 8 minutes before reaching their final stable dimer configuration. Although very limited in time, this experiment provides us with a rough estimate of the rate k_f of the conformational change necessary for the assembly. This rate is related to the energy barrier E associated with the conformational change by the Arrhenius equation $k_f = k_0 e^{-E/k_B T}$, where k_B is the Boltzmann constant. Assuming a value of 10^{11} – 10^{12}s^{-1} for the prefactor k_0 ³, the energy barrier E can be estimated to be about 0.8 eV. This value is possibly overestimated due to undersampling, as some more switching events may have been missed due to our limited image acquisition rate.

The energy barrier associated to the C to S transition of two Phe-Phe molecule interacting but not yet irreversibly bound to each other can be also roughly estimated as twice the adsorption energy difference between isolated C and S molecules in orientations similar to the ones observed during the assembling process. This gives a value for E of 0.78 eV. This is again only an indicative value as a small kinetic barrier could accompany the reverse S to C transition, while the concerted transition energy cost will be reduced by the interaction between the two molecules (as indeed expected since these transitions are only observed during such interaction). While these two estimates are consistent and broadly comparable, we note that the theoretical estimate mostly originates from the weakening of the molecule-surface interaction during the C to S transition. Indeed, it appears likely that breaking the bonds with the substrate could be the bottleneck event associated with the switching from a C to an S conformation and the change of the adsorption angle from 34° to 74° . Other energy barriers could be involved in the conformation switch. These include the barriers associated with the torsional angle change in the molecular backbone and those encountered during the sliding of the peptide oxygen along the compact $[1\bar{1}0]$ Cu atoms row to allow the adsorption angle change. However, both sets of barriers are expected to be low as transitions between C and S conformations are readily observed in our gas-phase simulations, while the peptide group sliding also occurs spontaneously in our DFT simulations on adsorbed

³Consistent with the attempt frequency associated with a relatively soft phonon mode [90].

molecules well below room temperature.

Conclusions

Our results suggest that stably adsorbed C Phe-Phe conformers undergo a change of conformation and adsorption bonding geometry if and only if they meet and interact. Thus, our results provide evidence that the free energy landscape associated to each molecule is significantly modified by the interaction, and in particular the energy barrier associated with the conformation change is expected to decrease significantly if a Phe-Phe adsorbed molecule meets and binds with another similar molecule of same chirality. In this case, the interaction eventually stabilises both molecules in the S conformation, which provides a better mutual binding geometry. Finally, our results show at the single molecule level that chiral recognition is a dynamic process, which involves mutually induced conformational adjustments. A general theory of biological specificity based on the conformational flexibility of interacting molecules for the expression of molecular complementarity was formulated by Pauling in the 30's and 40's of the last century [70]. Koshland later coined the term “induced fit” [71] to describe the dynamic recognition process in enzymatic reactions. Chiral recognition, on the other hand, is usually discussed in the context of the static three-point-model [10, 91]. Only recently attempts were made to implement a dynamic picture of enantioselective molecular interactions to account for possible mutual conformational adjustments [10, 92]. Our experiments constitute the first single molecule confirmation of this dynamic recognition picture, following the steps proposed by Booth, Wahnou and Wainer in 1997 [10]:

- (i) formation of the selectand-selector complex (tethering, Figures 4.6.1b/4.6.2a’);
- (ii) positioning of the selectand-selector to optimize interactions (conformational adjustments, Figures 4.6.1c-f/4.6.2c’-d’);
- (iii) formation of secondary interactions and expression of the molecular fit (chiral recognition, Figure 4.6.1h).

In general, the dynamic picture of enantioselective molecular interactions is not only important for chiral recognition and discrimination but is also relevant for the hierar-

chical transfer of molecular chirality to a higher level of complexity in supramolecular structures and materials [93].

Chapter 5

Adsorption Phase Diagram of Phe-Phe on Cu (110)

Increasing effort is currently being devoted to tailoring the structural and chemical properties of metal and semiconductor surfaces. Applications in a number of emerging technological fields, from heterogeneous catalysis to electronics and sensor development, pose novel specific requirements in terms of surface geometry and reactivity, which may be bestowed to bare surfaces via appropriate functionalization with organic molecules. The spontaneous assembly of molecular components with specifically designed functional groups is one of the most promising ways to achieve this goal [64]. Among the most successful applications to date are self-assembled monolayers (SAMs) of alkanethiols on gold [94, 95, 96]. In order to widen the range of patterns and available reactive sites, several polyfunctional building blocks are being put to trial, including peptides among the most promising candidates. Understanding the adsorption behaviour of peptides onto bare or oxidized substrates is of particular relevance in the fields of biosensors and biomaterials, since the interactions of a biocompatible material with the physiological environment is normally mediated by specific peptide sequences. Although a detailed knowledge of the adsorption scenario is essential to develop controlled and reproducible functionalization techniques, the atomic-scale features and mechanisms of dynamical supramolecular assembly processes of peptides on inorganic surfaces is still a relatively young field of research. In the previous chapters we have studied the basic requirements for the expression of footprint homochirality and the importance of

conformational flexibility in chiral recognition and supramolecular assembly. It was already pointed out in Chapter 3 that most aminoacids (with the exception of those that present conformational rigidity, as proline) show different conformational motifs at different adsorption temperatures on Cu(110). More recently, similar investigations have been extended to di- and tripeptides [84], which represent a further step towards complex and realistic systems of biological relevance. This chapter aims to the investigation of the adsorption phase diagram of enantiopure covered surfaces of L-Phe-L-Phe and D-Phe-D-Phe on Cu(110). The system was tract in a temperature range from 90K to 600K and six different adsorption geometries were identified. The structures were mainly studied by STM. To get more detailed information about the charging state of the carboxylic and amino groups in the different phases XPS data were taken at the HE-SGM beamline at BESSY II in Berlin, in collaboration with Dr. Thomas Strunkus and Prof. C. Wöll. Furthermore, we have also studied the overall geometrical properties of the phases by LEED and the chemical changes involved in the phase transitions by thermally programmed desorption (TPD), in collaboration with Dr. Sam Haq from the Surface Science center, Liverpool, UK. Since a mapping of the complete phase adsorption diagram by means of *ab-initio* DFT simulations would be too expensive from the computational point of view, we have restricted the theoretical analysis to classical molecular dynamics simulations. The structures obtained in gas phase where the interaction with the substrate is neglected should only be considered as a first approximation to propose feasible adsorption motifs. As already stated in section 3.3 the interaction with the surface could dramatically change the conformation of the molecule and therefore the overall geometry with respect to the structures in gas phase. On the other hand, the bonding schemes found in the simulations in gas phase are normally valid with some restrictions concerning the preferential on-top binding that is usually found for interactions of N and O with the underlying Cu atoms. Based on this considerations, different adsorption motifs are proposed to describe the adsorption phase diagram.

5.1 L-Phe-L-Phe deposition at low substrate temperatures

5.1.1 C and S pairs at 90-290K

When L-Phe-L-Phe is deposited onto the Cu (110) surface at 90K and analyzed by STM at 40K we observe mostly compact agglomerates of molecules (structures that cannot be clearly imaged by STM, where single molecules are not recognized in within) and only a few sparse single adsorbed molecules and pairs on the terraces. As confirmed by LEED, no long-range structural order is detected which is attributed to restricted surface diffusion at low substrate temperatures. After 15 hs with the substrate temperature held at 40K, we observe that the agglomerates start to dissolve and more pairs evolve. An analog scenario is observed when the molecules are deposited and measured after 1 hour at 150K, where about $\sim 40\%$ of the total number of molecular structures present on the surface are pairs (not shown here). The complete dissolution of the agglomerates is reached at 280K where a few supramolecular chains (equal to the room temperature chains described in the previous chapter) grow and mainly single molecules (about 40% of the total number of molecular structures on the surface) and molecular pairs (about 50% of the total number of molecular structures on the surface) are found on the terraces, see Figure 5.1a.

Interestingly, there are two kinds of molecular pairs at low temperatures. One type of pairs have the same structure as the molecular chains observed at room temperature (see Figure 4.3 and Figure 5.1c). As described in the previous chapter, these pairs are formed by molecules in the “S” conformation interacting by ionic H-bond. They show an enhanced stability when compared to longer chains caused by the charging state of their constituents (see Discussion in the previous chapter). The second type of pairs are constituted by adsorbed molecules with the molecular backbone oriented at an angle $\alpha_1 = (32 \pm 2)^\circ$ CCW from the substrate $[1\bar{1}0]$ direction (white circles in Figure 5.1a, d). The intermolecular distance measured from the brightest point of the protrusions associated with the phenyl rings in the growth direction (oriented at an angle $\alpha_2 = (85 \pm 4)^\circ$ from the $[1\bar{1}0]$ direction) amounts $(7.8 \pm 0.5)\text{\AA}$. These pairs are only observed at low temperatures, and disappear completely at about 330K. We have never observed longer supramolecular chains growing with this geometry, nor new

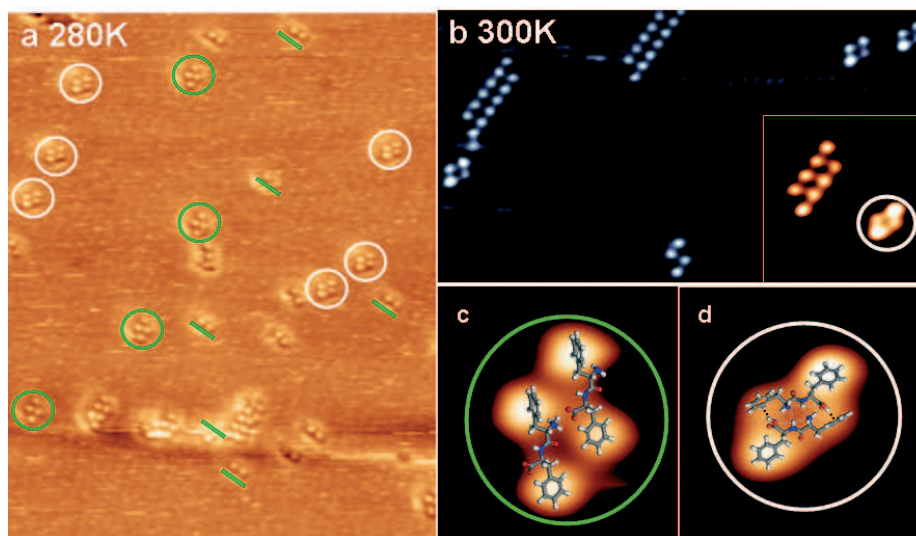


Figure 5.1: STM images of L-Phe-L-Phe on Cu(110) after annealing to 280 and 300K. a) STM image (41×50 nm) of the structures present at 280K: single adsorbed molecules (green lines), "S" pairs (described in section 4.2.1) in green circles and "C" pairs in white circles. b) Structures after annealing at 300K (31×17 nm), note that more supramolecular chains evolve. c) high resolution STM image (2.8×3.2 nm) of "S" pairs with superimposed DFT model (described in section 4.2.2). d) high resolution STM image (3.4×3.6 nm) of "C" pairs with superimposed MD gas phase model from Amber simulations.

structures that could be associated with a rotation of the former pairs. This might imply that it is simply not possible for these structures to growth by interaction with further approaching molecules, indicating that they do not present the "head to tail" bonding necessary to form longer chains. Therefore, the experimental evidence pointed to a "closed" structure where the functional groups are all located in the inner part of the pair. In other words, these might be pairs of molecules in the "C" configuration. Based on these considerations, a structural model based on AMBER simulations in gas phase (c.f. Section 4.2.2) is proposed in Figure 5.1d. In this model the molecule interacts with the surface by the carboxylic and amide oxygens by the same atop interaction described in the previous chapters. Moreover, the structures are stabilized by four weak hydrogen bonds. Namely, $\text{NH} \cdots \text{NH}_2$ and $\text{COOH} \cdots \text{Phe}$ hydrogen bonds. This type of H-bonds are commonly found in biological structures [63]. The STM images show that these second type of pairs present always a phenyl group that appears much brighter than the other one within the same molecule. This agrees with the model where one phenyl

group per molecule is rotated to maximize the interaction with the carboxylic group of the neighboring molecule, Figure 5.1d.

The closed pairs are already observed at 90K, while the S pairs only start to evolve at 280K. This observation is consistent with the fact that the “closed pairs” involve molecules in the neutral C conformation where no intermolecular hydrogen transfer has taken place. We note that although 4 H-bonds are expected to stabilize the pairs in the C configuration, it is likely that this type of bonds are weaker than an ionic H-bond, as described for the S pairs 4.2 [63], this observation would agree with the fact that this closed pairs dissociate at temperatures above room temperature. However, a more detailed discussion of this issue requires further theoretical analysis.

Between 290K and 315K the percentage of supramolecular chains composed by molecules in the S configuration increases and 3 hs after deposition is about 25% of the total of supramolecular structures on the surface (see Figure 5.1b). Accordingly, the number of single molecules and the number of S pairs decreases while the number of C pairs remains constant.

5.2 Phe-Phe deposition at high substrate temperatures

5.2.1 Phase I: 315-360K

In the temperature range from about 330 to 360K, no C pairs are observed and the only structures that are present on the surface are either single adsorbed molecules or chains constituted by two or more molecules in the S configuration. The precise atomistic structure and the molecular mechanisms that control the formation of these chains have been already discussed in the previous chapter. Here we discuss the enantiopure phases formed by a single enantiomer of Phe-Phe and present further experimental evidence of the models proposed in the previous chapter. The full understanding of the room temperature phase allow us to draw some conclusions about the adsorption phase diagram of Phe-Phe on Cu(110) at different temperatures.

LEED and STM characterization

By increasing the coverage of Phe-Phe at room temperature, the length and the number of chains increases monotonically [65]. The LEED pattern of L-Phe-L-Phe and D-Phe-D-Phe films at room temperature are characterized by streaky diffraction lines at 55° CW and CCW from the short reciprocal unit vector respectively (see red lines in Figure 5.2 a,b). These diffraction lines correspond to periodic supramolecular chains oriented at 55° from the $[1\bar{1}0]$ crystal axis in the real space (Figures 5.2 c, d). The STM and LEED patterns of L-Phe-L-Phe and D-Phe-D-Phe are related by mirror inversion, evidencing the global supramolecular chirality of this phase. The inter-line distance as obtained from the LEED pattern is equivalent to $|\mathbf{a}_s^*|/2.48$, where \mathbf{a}_s^* is the short reciprocal unit vector. The corresponding real space periodicity along the chain is thus equal to $|\mathbf{a}_0| \times 2.48 = 8.97\text{\AA}$, where $|\mathbf{a}_0|=3.615\text{\AA}$ is the long unit vector of the surface cell. This geometrical parameter obtained by LEED is in good agreement with the model discussed in the previous chapter and with the $(9.3\pm 0.5)\text{\AA}$ distance measured by STM between the centers of two phenyl rings in neighboring molecules. Still no perpendicular periodicity can be seen, as indicated by the absence of diffraction spots in the LEED patterns. Even at saturation coverage of one monolayer no periodic order is observed in any other direction. This is consistent with the STM images where no periodicity is encountered across the chains.

XPS

Sample preparation and experimental details

The XPS data were obtained at room temperature. All spectra were referenced against the Cu 3p_{3/2} line at 75.1 eV. The raw data represent an average of 100 measurements. The presented XPS data were taken of a sample obtained by cleaning the Cu crystal with cycles of sputtering and annealing to 800 K and then sublimation of D-Phe-D-Phe from a Quartz crucible held at 450K. By XPS the adlayer coverage was determined to be about two third of a close-packed monolayer. The fitting for deconvolution and determination of the peaks positions was made with a combination of gaussian-lorentzians curves after Shirley type background subtraction. Within a given element, the full width at the half maximum (FWHM) parameter was fixed for the fit curves, taken a well resolved

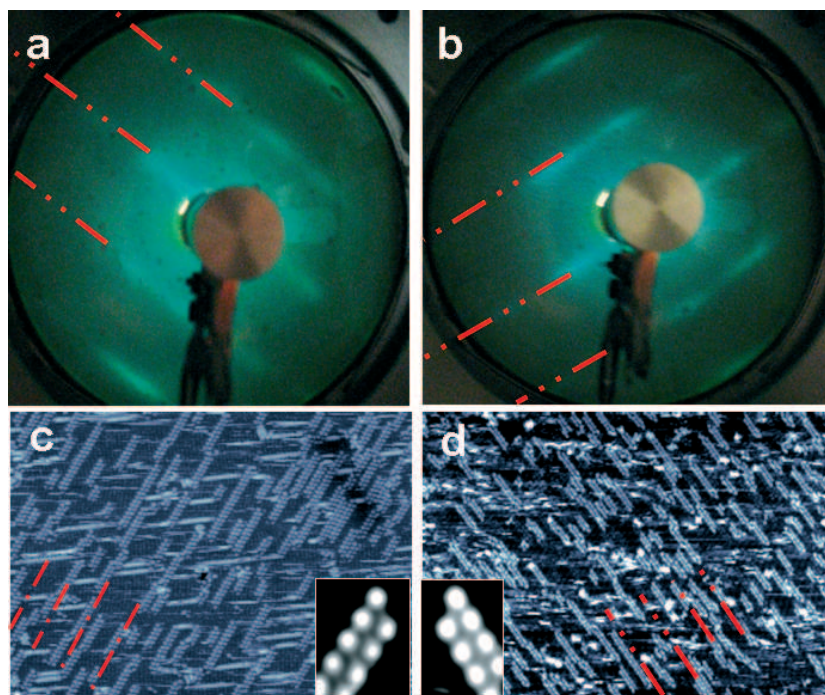


Figure 5.2: LEED and STM of (a,c) L-Phe-L-Phe (b,d) D-Phe-D-Phe at room temperature ($100 \times 70 \text{ nm}$). The red lines indicate the periodicity along the chains. The fuzzy lines in the STM images are related to single molecules that diffuse under the STM tip while scanning. High resolution STM images are shown in the insets.

component of the multilayer as a reference value.

XPS and TPD measurements

XPS measurements allow us to get an insight on the chemical state of the adsorbed molecules. TPD measurements identify the molecules that are being desorbed from the adsorbed layers. By collecting the information obtained by both techniques, it is possible to describe the key reactions involved in the phase transitions. As described in the previous chapter, the appearance of supramolecular chains is accompanied by a chemical change of the adsorbed molecules. The XPS measurements in Figure 5.3 confirm that deposition of about two third of a monolayer results in a zwitterionic phase. For comparison, the peaks expected from the literature for the neutral and the zwitterionic scenario in related aminoacids and peptides are summarized in Table 5.1.

C1s	Number of elements and Corresponding Chemical State
284.7–285.3 eV	14 C phenyl rings and CH ₂ –Zwitterionic, Anionic, Neutral
286.0–287.3 eV	2C asymmetric (chiral centers) –Zwitterionic, Anionic, Neutral
287.5–288.4 eV	1C carboxylate, 1C peptide bond– Zwitterionic, Anionic 1C from peptide bond–Neutral
289.5 eV	1C carboxylic acid –Neutral
up to 290 eV	Shake up–Zwitterionic, Anionic, Neutral
O1s	
531.1–531.5 eV	2 resonant carboxylate O and 1 carbonyl O of peptide bond –Zwitterionic, Anionic 1 carbonyl O of peptide bond –Neutral
532.3 and 533.6 eV	2O protonated carboxylic group (C=O and C-OH , respectively)– Neutral
N1s	
401.1–401.7 eV	1N NH ₃ ⁺ –Zwitterionic
399.5–400.5eV	1N NH of peptide bond–Zwitterionic, Anionic, Neutral 1N NH ₂ –Anionic, Neutral

Table 5.1: XPS assignments expected for Phe-Phe on Cu(110) by comparison with literature [97, 98, 99, 100, 101, 102, 103, 104, 105].

The C1s core level emission of adsorbed Phe-Phe shows four peaks (Figure 5.3a) . The broad signal at around 292 eV is related to $\pi-\pi$ shake up. The 12 carbons from the phenyl rings and the 2 CH₂ carbons appear together under the same peak at 285.2 eV, as also observed for solid state phenylalanine and tyrosine [106]. The two asymmetric carbons have a similar chemical environment and appear at 286.7 eV. The component at 288.3 eV corresponds to one carbon from the amide group and one carbon for the carboxylate group. Within the experimental error, no relevant emission intensity could be detected at binding energies around 289.5 eV characteristic of the neutral form of the carboxylic group. The absence of this peak allows us to exclude the presence of significant amounts of neutral species on the surface. This is further confirmed by the O1s spectra (Figure 5.3b) that is dominated by the component at around 531 eV, typical of carboxylate moieties, instead of the two evenly intense components at 532.3 and 533.6 eV that are expected for a neutral carboxylic group [107]. The binding asymmetry of the O1s component is probably due to slightly different chemical environments of the oxygen atoms, i.e. due to closely lying unresolved 1s binding energies [108].

The C1s and O1s spectra described above are only compatible with either a zwitterionic or an anionic phase of Phe-Phe. The TPD spectra show in Figure 5.5 shows that a molecular phase adsorbed at 80K and gradually heated till the decomposition of the monolayer at about 550K shows only two distinct losses of H between 400 K

and 450K. No significant H loss is observed in the room temperature range where the supramolecular chains evolve, therefore the TPD data also point to a zwitterionic phase at room temperature. Note that TPD data is further discussed in the next section. This interpretation is further supported by the analysis of the the N1s core level signal. For the case of a neutral or anionic molecule, only one peak at about 399.5 eV which corresponds to both the amino and the amide nitrogens is expected. For a zwitterion, two peaks with a binding energy difference of about 2 eV are expected, one for the amide and the other one corresponding to the protonated ammonium group. The N1s shown in Figure 5.3c shows two components at room temperature with a binding energy difference of 1.9eV. The peak at higher binding energy is assigned to the protonated NH_3^+ ammonium group. The lower binding energy component is mainly assigned to NH of the amide group ¹

We notice that the energy shift for the NH_3^+ signal is about 0.5 eV lower to what informed in literature for related aminoacids on Cu(110) and peptides on gold [6]. We attribute this difference to a strong molecule-molecule and molecule-substrate interaction, as proposed in the model obtained by DFT calculations discussed in the previous chapter.

5.2.2 Phase II: 400K

LEED and STM measurements

After annealing of the room temperature phase I to 360K, a few molecules start to rotate and form a new adsorbate registry on the surface. The evolution of this phase is completed after annealing to 400K where phase I supramolecular chains are no longer observed. The 400K phase is also chained and shows global organizational chirality, being the L-Phe-L-Phe chains rotated 69° CW (see Figure 5.4) and the D-Phe-D-Phe chains rotated 69° CCW from the substrate $[1\bar{1}0]$ direction. Phase II evolves always, independently of starting coverage and after annealing to 400K.

The LEED pattern shows periodic streaky diffraction lines at 70° from the short reciprocal unit vector (see blue lines in Figure 5.4) which correspond to a direction that is rotated by 70° from the $[1\bar{1}0]$ crystal axis in the real space. The inter-line distance

¹ a low percentage of either neutral NH_2 groups or decomposed fragments caused by beam damaged cannot be totally neglected [6, 108].

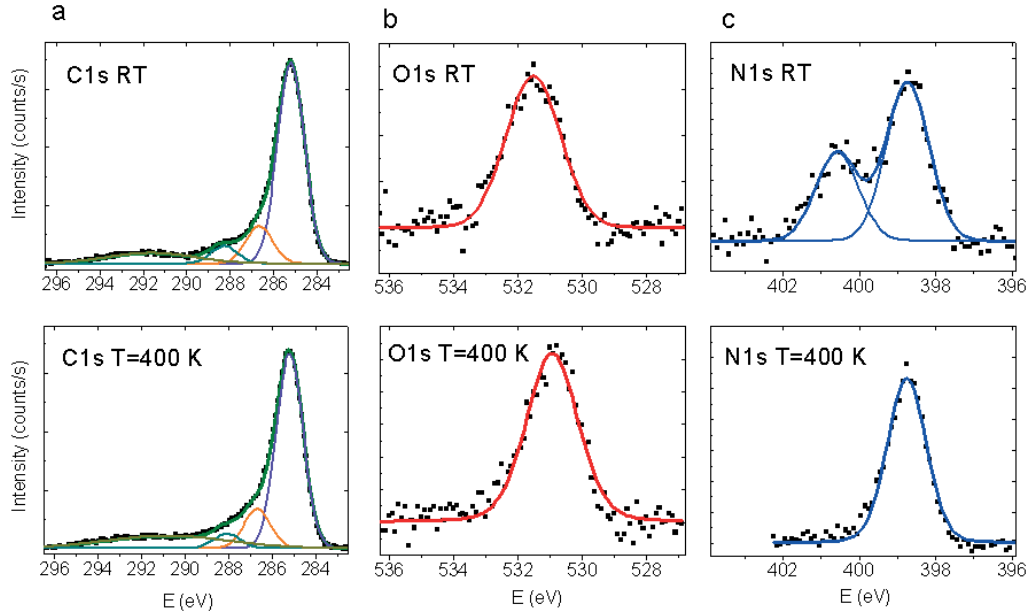


Figure 5.3: XPS spectra of D-Phe-D-Phe on Cu(110). a) C1s signal after adsoption at room temperature (upper spectrum) and after annealing to 400 K (lower spectrum). b) O1s signal after adsoption at room temperature (upper spectrum) and after annealing to 400 K (lower spectrum). c) N1s signal after adsoption at room temperature (upper spectrum) and after annealing to 400 K (lower spectrum)

as obtained from the LEED pattern is equivalent to $|\mathbf{a}_S^*|/2.22$, where \mathbf{a}_S^* is the shorth reciprocal unit vector. The corresponding real space periodicity along the chain is thus equal to $|\mathbf{a}_0| \times 2.22 = 8.02\text{\AA}$, where $|\mathbf{a}_0| = 3.615\text{\AA}$ is the long unit vector of the surface cell. This value is related to the distance between the centers of two phenyl rings in neighboring molecules measured from the STM images (Figures 5.4c, d) that amounts $(7.5 \pm 0.4)\text{\AA}$. Still no perpendicular periodicity can be seen at any coverage. Even if the interchain distance has no periodicity, it is smaller in respect to what generally observed for phase I. On the other hand, the chains themselves present more kink defects at 400K (see discussion of the model after XPS subsection).

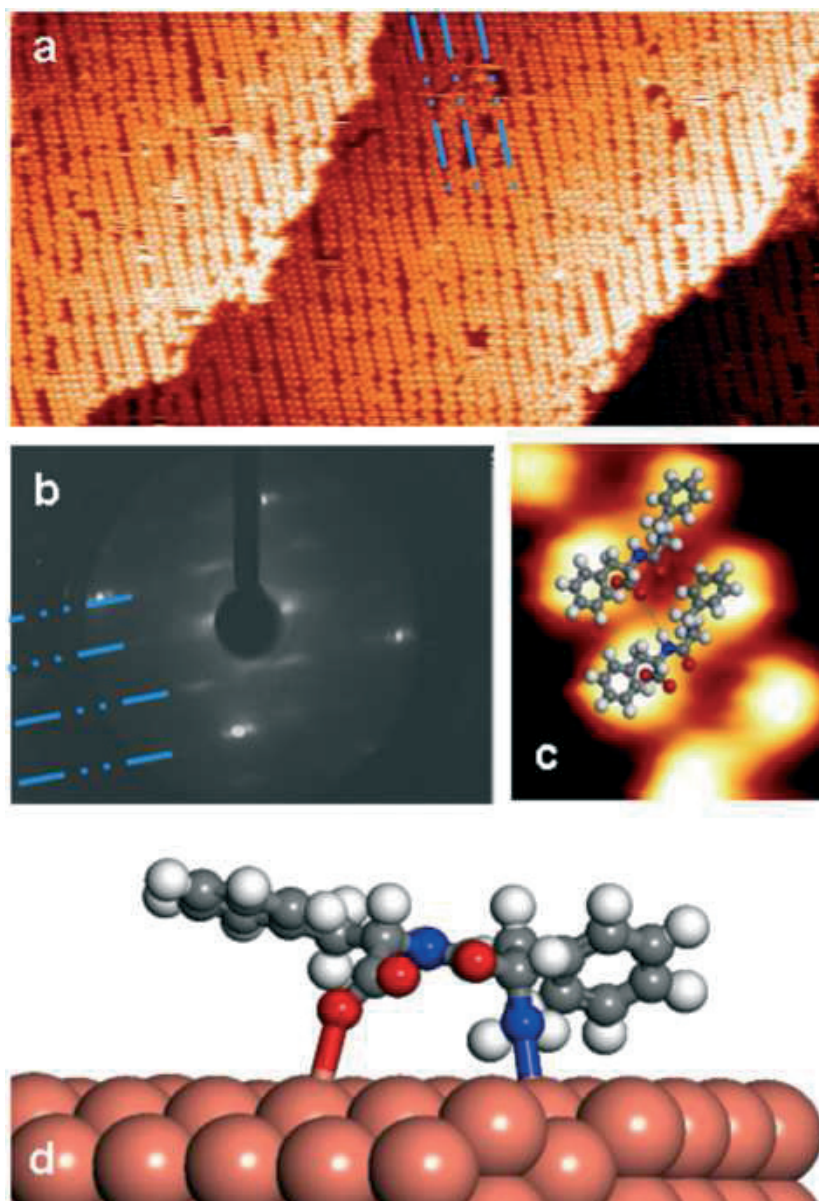


Figure 5.4: L-Phe-L-Phe adsorbed on Cu(110) and annealed to 400K (Phase II). a) STM image. b) LEED pattern. c) High resolution STM picture with superimposed schematic model ($2.0 \times 2.5 \text{ nm}$). d) lateral view of the model shown in c).

XPS

The C1s and O1s XPS spectra of the phase II supramolecular chains does not significantly differ from the spectra of the room temperature phase I and can therefore be assigned to the same chemical states, i.e either zwitterionic or anionic (Figure 5.3 a, b). On the other hand, the N1s spectra shows only one emission peak at 398.8 eV while the high binding energy peak associated with the ammonium group has completely disappeared (Figure 5.3 d). This indicates that the amino group is not protonated and therefore that the molecule is globally anionic. This is further confirmed by a significant H loss peak in the TPD spectra at around 400K (Figure 5.5), described in the next section.

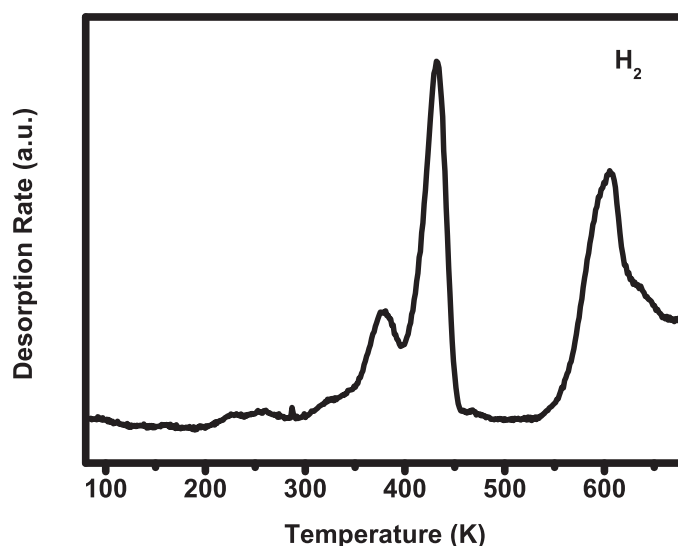


Figure 5.5: TPD taken after adsorption of Phe-Phe on Cu(110) at 85K.

TPD

The thermal desorption of hydrogen was measured by a quadrupole mass spectrometer as the temperature of the sample was increased at a rate of 1 K/s. The H₂ desorption is characterized by two main features with peak maxima at 399 K and 438 K, Figure 5.6.

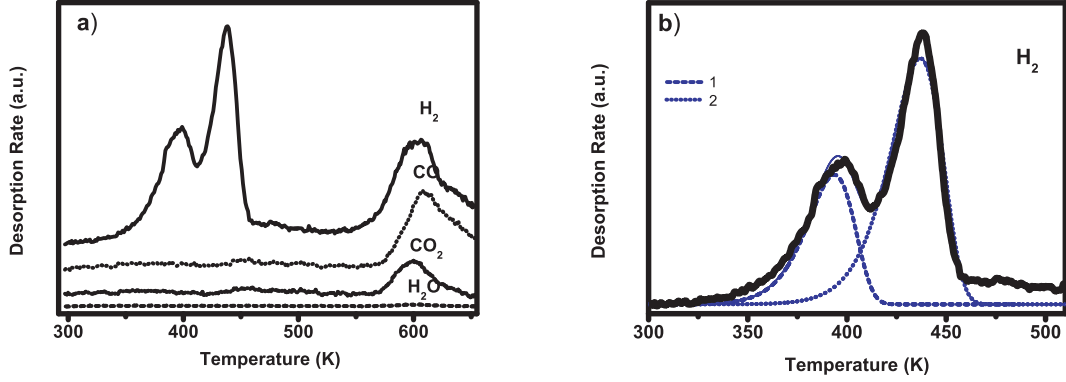


Figure 5.6: a) TPD spectrum following the desorption of hydrogen, carbon monoxide, carbon dioxide, and water. b) spectral fit with two components [109].

The spectrum is fit very well by a two-component model, where in each component the desorption rate of hydrogen is taken to be first-order in the concentration of the adsorbed hydrogen. The desorption rate r is then given as

$$r(\theta_i, T) = -\frac{d\theta_i}{dt}(\theta_i, T) = \nu\theta_i e^{-E_i/k_B T} \quad (5.1)$$

where θ_i is the concentration of the hydrogen atom, t is time, ν is the pre-exponential rate factor taken to be the conventional value of $10^{13} s^{-1}$, T is the sample temperature, and k_B is Boltzmann's constant. In the present case, the recombination of the hydrogen and the subsequent desorption of the molecular hydrogen from the surface are expected to proceed very fast at the temperature where the desorption peaks are observed since hydrogen desorption from Cu(110) has been previously observed to occur at 290-340 K [60]. In this case the observed desorption kinetics are therefore limited by the dissociation of the hydrogen atom from the molecule. We interpret the two peak TPD spectrum as being related to the dissociation of two or more different hydrogen atoms, H1 and H2, from each of the molecules. Therefore the concentration or coverage, θ_i ($i=1$ or 2), should be interpreted as the concentration of Phe-Phe molecules which have the H1 or H2 atom still attached. The two-peak model can be expressed as

$$r(\theta_1, \theta_2, T) = \nu\theta_1 e^{-E_1/k_B T} + \nu\theta_2 e^{-E_2/k_B T} \quad (5.2)$$

The initial coverage values for θ_1 and θ_2 , as well as the binding energies E_1 and E_2 for the two desorbing species of hydrogen were treated as variational parameters in a fitting routine which minimized the RMS error between eqn. 5.1 and the experimental data. The result of the fitting was that the initial coverage of the higher temperature peak was approximately two times (exactly: 2.10) larger than the other peak and the resulting energies were 106.1 and 118.2 kJ/mol. We interpret the difference in the initial coverages (also equivalent to the integrated peak area) as being due to the higher temperature peak comprising the desorption of two hydrogen atoms from each molecule, i.e., a coordinated two hydrogen dissociation.

By this combined XPS-TPD analysis we determine that the desorbed hydrogen observed in the first peak of the TPD spectrum arises from the ammonium group that is deprotonated by interaction with the copper substrate, because no significant chemical shift is evidenced in the XPS spectra of the other elements after annealing to 400K. The H atoms could diffuse on the surface after deprotonation and recombine to form H_2 , as seen for other molecules on Cu (110) [6]. Here, we emphasize that no other desorption accompanies the H_2 desorption, implying that the reaction is limited to deprotonation. In particular, the desorption peaks are unlikely to be related to the formation of amide or imine bonds by condensation reactions, since no H_2O peak is observed at any temperature before molecular desorption (Figure 5.6a).

The combined analysis allows us to propose a model where the amino group gets closer to the underlying Cu atoms and is deprotonated. This interaction could provoke the disruption of the hydrogen bond with the carboxylic group and induce the rotation of the whole molecule what will now mainly be stabilized in a new position by the on-top interaction of one oxygen of the carboxylate group, the nitrogen of the amino group and the intermolecular H bond $COO^- \cdots HN$. Further weak $\pi \cdots \pi$ interactions could contribute to hold the molecules in this preferred configurations. The proposed model is shown in Figure 5.4c,d. It is important to notice that this represents just a speculative picture that puts together all the information obtained by the different experimental techniques. A more precise model requires further theoretical calculations.

5.2.3 Phase III: 450K

LEED, STM and TPD measurements

If the phase II is further annealed to 450K, a 2D phase evolve. LEED measurements show that the unit cell in the real space can be described by the

$$\begin{bmatrix} 4 & -2 \\ 0 & 3 \end{bmatrix}$$

matrix (Figure 5.7 b). A second H₂ desorption peak at about 440K is shown in Figure 5.6. The TPD spectra shows that the surface is stable until about 600K when coincident desorption peaks for amu 2 (H₂), 28 (CO) and 44 (CO₂) are observed (Figure 5.6a).

The peptide core of the molecule in phase III is more clearly resolved than in phase I and II and is imaged as two asymmetric protrusions (white circles in Figure 5.7a, c). As shown in the previous section, the TPD spectrum indicates that the second desorption peak is most likely associated with the desorption of two H atoms from each molecule. A number of chemical processes are possible, but we propose that dehydrogenation of the nitrogen of the amino group and the asymmetric carbon to form a C=N double bond could have taken place. We speculate that this process could be energetically favorable since the final state would correspond to more conjugated molecule, but we do not have calculations to support this tentative model. Further XPS measurements are planned to get a better understanding on this issue. An interesting experiment to explore the mechanism of H-loss could be the adsorption of a molecule that is deuterated in the H positions that are believed to be involved in the deprotonation/dehydrogenation processes.

Schematic model of phase III

Based on the LEED, STM and TPD data we propose a model that has the $\begin{bmatrix} 4 & -2 \\ 0 & 3 \end{bmatrix}$ unit cell described by LEED and STM (Figure 5.7c,d). The molecule is interacting to the Cu surface essentially by the same N-Cu and O-Cu atop interactions described for phase II. Despite no clear statement could be made on the exact orientation of the phenyl rings, taking into account that a variety of different conformations would lead

to π -stacking it is likely that at the phenyl-phenyl distance of 5.7\AA that is found in the schematic model (Figure 5.7 c) π - π interactions could contribute to the overall ordering. Furthermore, we propose that the $\text{N-H}\cdots\pi$ bond is the main responsible of the intermolecular structures schematized in Figure 5.7 d. Exactly this kind of intermolecular interaction is found to stabilize secondary structures of several proteins [63].

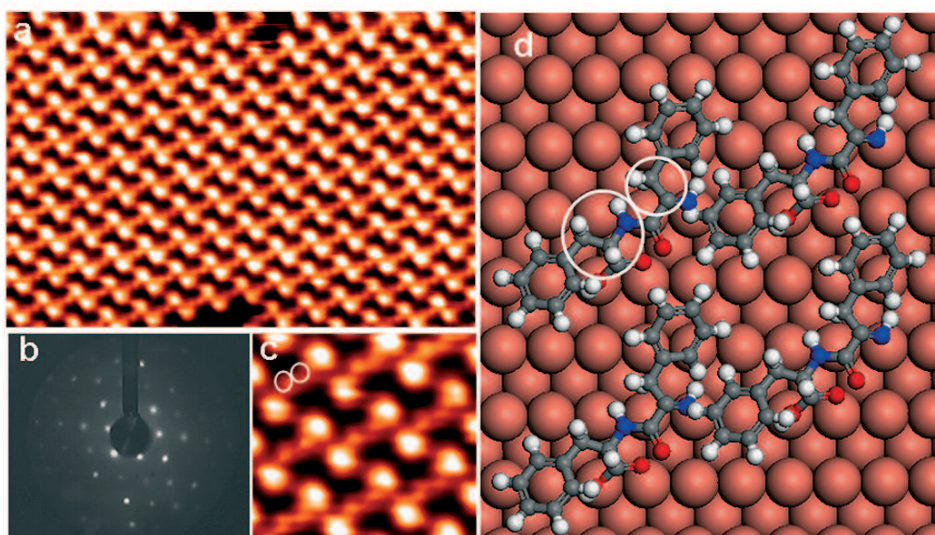


Figure 5.7: L-Phe-L-Phe adsorbed on Cu(110) and annealed to 450K (Phase III). a) STM image (15×10.4 nm). b) LEED pattern. c) High resolution STM picture (5×4 nm). d) proposed model for the structure shown in c).

Intermezzo : Peptide Nanostructures

Two branches of supramolecular biochemistry are investigating the formation of nanoscale objects by the self-assembly of various polypeptide molecules as Phe-Phe into highly ordered structures. One branch is dealing with the pathological phenomenon of amyloid fibril formation and is driven by a medical motivation to prevent the formation of these toxic assemblies. The other branch is focused on the development of novel materials and devices as part of the emerging nanotechnology field. Apparently, these two branches have no common root. However, similar building blocks are used and comparable nanostructures are formed. It appears that common general principles of geometrically restricted interactions, and specific and coordinated assemblies, are being

shared by both groups. A key theme is the hypothesis regarding the role of π -stacking interactions in amyloid fibril formation, which has led to the production of peptide nanotubes and nanospheres [74]. Peptide nanostructures represent an intriguing example of an interdisciplinary research characteristic of recent modern science. Applications, methodologies and theories that were applied to the study of carbon and inorganic nanostructures should be of great importance for future exploration and utilization of the peptide nanostructures. The properties of the peptide nanostructures, taken together with their biological compatibility and remarkable thermal and chemical stability, may provide very important tools for future nanotechnology applications [110].

Outlook : Chiral cavities

Many processes, including heterogeneous catalysis and chromatographic separations, are commonly performed using solid surfaces. An interesting task in surface science nowadays is to prepare surfaces that can make such processes enantioselective. During the recent years, we have successfully demonstrated the absorption capabilities of metal-organic networks that expose achiral nanocavities for the size-selective adsorption of several guest molecules, including Phe-Phe [111, 112]. The coating of surfaces with

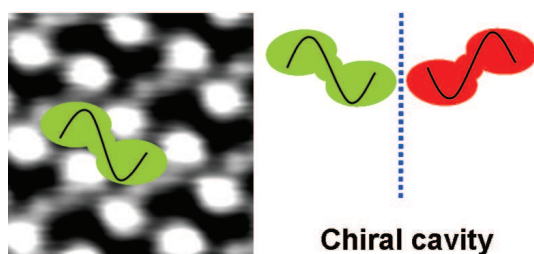


Figure 5.8: High resolution STM image highlighting the chiral cavities exposed by Phase III of Phe-Phe on Cu(110).

2D open void structures allows guest molecules to bind only to the substrate exposed by the cavities of the molecular layer that are believed to be responsible for imparting enantioselectivity, by forcing the orientation of reactant molecules docking onto catalytically active metal sites [5]. We note that phase III expose chiral cavities (Figure 5.8). In order to use the enantiomerically pure phases of Phe-Phe as model systems to study chiral separation processes, we plan to explore the adsorption properties of the chiral

cavities in phase III for the separation of racemic mixtures of guest molecules. We plan to test the conformational and size-selectivity of the structures discussed in this chapter in order to design supramolecular modified surfaces for heterogeneous catalysis.

5.3 Conclusions

In the present chapter we have discussed the different surface organizations of Phe-Phe on Cu (110) occurring over the temperature range 90-600K. The different adsorption motifs vary in molecular orientation, molecule-metal bonding and adsorbate footprints. A summary of the phase diagram is presented in Figure 5.9. Single adsorbed molecules are always present in the “C” neutral conformation that is the most stable in gas phase. These single adsorbed molecules presents always the same molecular footprint from 90K to room temperature.

Molecular pairs are present in two different molecular orientations and adsorbate footprints. “C” pairs evolve from single adsorbate molecules at temperatures below 330K and are formed by “C” neutral molecules. “S” pairs evolve at 280K and are the basic structural unit that determines the global supramolecular chained ordering. For temperatures of 400K and 450K two distinct H losses are most likely driving the structural changes that determine the appearance of phase II and phase III. The different molecular footprints found in the adsorption phase diagram are mainly determined by the interaction of the functional groups with the surface. In particular, the amino group is likely to play the most important role in determining the interaction with the underlying Cu atoms. Furthermore, its protonation state influences significantly the overall supramolecular order.

The interplay between molecule-surface and molecule-molecule interactions determines the chemical state and the conformational shape of the modifiers that will lately determine the overall supramolecular arrangement. Hydrogen bonds and π -stacking that are ubiquitous in biological systems and play a central role in determining the secondary structures of proteins, are also fundamental in establishing the directionality and global chirality of the adsorbed phases described in this chapter.

Finally, we find that at least one strong interaction (e.g. phase I) or a combination of weak interactions (e.g. Phase II and III) should exist among the molecules to have

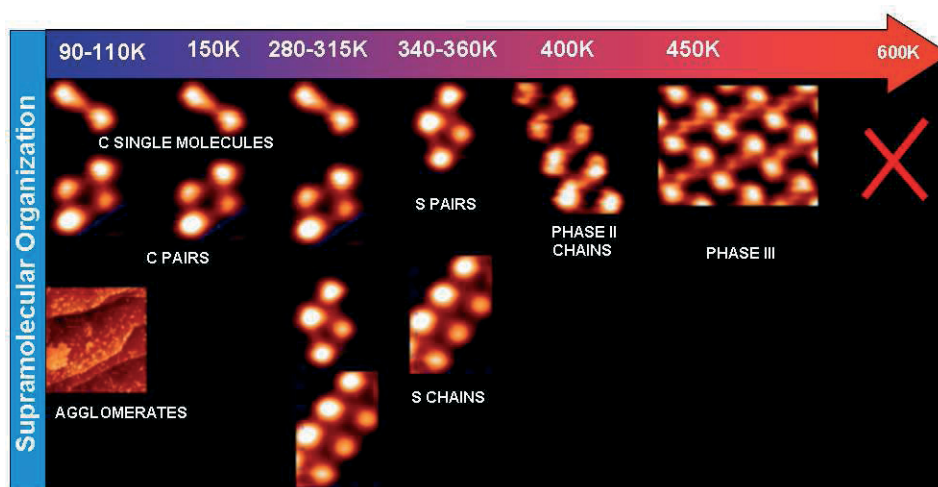


Figure 5.9: Schematic Adsorption Phase Diagram of Phe-Phe on Cu(110)

an overall supramolecular chiral system. Furthermore, we provide evidence that the interacting locations (molecule-molecule or molecule-substrate) can dynamically change under different temperature conditions.

Abbreviations and Common Symbols

Abbreviations

0D, 1D, 2D, 3D	Zero-, One-, Two-, Three-Dimensional
DFT	Density Functional Theory
GGA	Generalized Gradient Approximation
HOMO	Highest Occupied Molecular Orbital
HOPG	Highly Oriented Pyrolytic Graphite
IR	Infra Red
LEED	Low Energy Electron Diffraction
LUMO	Lowest Unoccupied Molecular Orbital
ML	Monolayer
NEXAFS	Near Edge Photoelectron Absorption Fine-Structure
OMBE	Organic Molecular Beam Epitaxy
TPD	Temperature Programmed Desorption
RAIRS	Reflection Absorption Infrared Spectroscopy
STM	Scanning Tunneling Microscopy
Phe	Phenylalanine
Tyr	Tyrosine
Phe-Phe	Di-phenylalanine
UHV	Ultra-High Vacuum
XPS	X-ray Photoelectron Spectroscopy

Common Symbols

a_0	lattice constant of Cu, $a_0=3,615\text{\AA}$
dI/dV	differential conductance
E	energy with respect to the Fermi energy
e	electronic charge, $e = -1.6 \cdot 10^{-19} \text{ C}$
E_F	equilibrium Fermi energy
$f(E, T)$	equilibrium Fermi function
k_B	Boltzmann constant, $k_B = 0.0862 \text{ meV/K} = 1 \text{ eV}/11604 \text{ K}$
m_e	free electron mass, $m_e = 9.1 \cdot 10^{-31} \text{ kg}$
m^*	effective electron mass
n	electron density
d	tip-sample distance
T	temperature
U	external potential energy
V	electric potential of sample with respect to tip
Φ	work function
z	tip height

Non-SI-units

<i>torr</i>	pressure unit (mm Hg), $1 \text{ torr} = 133,322 \text{ Pa} = 1,33322 \text{ mbar}$
-------------	---

Bibliography

- [1] V. I. Goldanskii, Doklady Akademii Nauk **347**, 117 (1996), 0869-5652.
- [2] Dekker, *Dekker Encyclopedia of Nanoscience and Nanotechnology* (VCH, Eds. James A.Schwartz-Christian Contescu-Karol Putyera, 2004).
- [3] D. Stacchiola *et al.*, Journal of Physical Chemistry B **109**, 851 (2005).
- [4] M. O. Lorenzo, C. J. Baddeley, C. Muryn, and R. Raval, Nature **404**, 376 (2000).
- [5] Z. Ma and F. Zaera, Surface Science Reports **61**, 229 (2006).
- [6] S. M. Barlow and R. Raval, Surf. Sci. Rep. **50**, 201 (2003).
- [7] M. Sarikaya *et al.*, Nature Materials **2**, 577 (2003), 1476-1122.
- [8] L. H. Easson and E. Stedman, Biochemical Journal **27**, 1257 (1933), part 2.
- [9] A. G. Ogston, Nature **162**, 963 (1948).
- [10] T. D. Booth, D. Wahnon, and I. W. Wainer, Chirality **9**, 96 (1997).
- [11] A. Kuehnle, T. R. Linderoth, B. Hammer, and F. Besenbacher, Nature **415**, 891 (2002).
- [12] G. Binning and H. Rohrer, Nobel lecture (1986).
- [13] G. Binning, H. Rohrer, C. Gerber, and E. Weibel, Phys. Rev. Lett. **49**, 57 (1982).
- [14] F. Besenbacher, Rep. Prog. Phys. **59**, 1737 (1996).
- [15] W. Ho, J.Chem. Phys. **117**, 11033 (2002).

- [16] N. J. DiNardo, *Nanoscale Characterization of Surfaces and Interfaces* (VCH, Weinheim, 1994).
- [17] R. Edstrom, X. Yang, G. Lee, and D. Evans, *FASEB* **4**, 3144 (1990).
- [18] F. Besenbacher, E. Lægsgaard, and I. Stensgaard, *Materials today* **8**, 26 (2005).
- [19] J. Bardeen, *Phys. Rev. Lett* **6**, 57 (1961).
- [20] J. Tersoff and D. R. Hamann, *Phys. Rev. Lett.* **50**, 1998 (1983).
- [21] N. D. Lang, *Phys. Rev. B* **34**, 5947 (1986).
- [22] N. D. Lang, *Phys. Rev. Lett.* **55**, 230 (1985).
- [23] N. D. Lang, *Phys. Rev. Lett.* **56**, 1164 (1986).
- [24] N. D. Lang, *Phys. Rev. B* **34**, 5947 (1986).
- [25] N. D. Lang, *Phys. Rev. Lett.* **58**, 45 (1987).
- [26] N. D. Lang, *Phys. Rev. B* **36**, 8173 (1987).
- [27] T. M, K. K, I. N, and Kageshima, *Surf. Sci. Rep.* **13**, 265 (1991).
- [28] T. M *et al.*, *Japan J. Appl. Phys.* **32**, 1352 (1993).
- [29] G. Doyen, D. Drakova, and M. Scheffler, *Phys. Rev. B* **47**, 9778 (1993).
- [30] P. Sautet and C. Joachim, *Chem. Phys.* **135**, 99 (1989).
- [31] G. Doyen *et al.*, *Phys. Rev. B* **48**, 1738 (1993).
- [32] C. J. Chen, *Phys. Rev. Lett.* **69**, 1656 (1992).
- [33] C. J. Chen, *J. Vac. Sci. Technol. B* **12**, 2193 (1994).
- [34] J. V. Barth, H. Brune, and G. Ertl, *Phys. Rev. B* **42**, 9307 (1990).
- [35] W. Ho, *J. Chem. Phys.* **117**, 11033 (2002).

- [36] J. Nieminen, S. Lahti, S. Paavilainen, and K. Morgenstern, Phys. Rev. B **66**, 165421 (2002).
- [37] J. Stoehr, *Nexafs Spectroscopy* (Springer Series in Surface Sciences, Berlin, 1992).
- [38] M. Polanyi and E. Wigner, Zeitschrift Fur Physikalische Chemie–Stoichiometrie Und Verwandtschaftslehre **139**, 439 (1928), 0372-8501.
- [39] S. Haq, private communication, 2007.
- [40] N. Sheppard and Erkelens, Appl. Spectrosc. **38**, 471 (1984).
- [41] K. W. Kolasinsky, *Surface Science: foundation of catalysis and nanoscience* (Wiley, New York, 2002).
- [42] *International Tables for Crystallography*, edited by J. S. Kasper and K. Lonsdale (Kynoch Press, Birmingham, 1959).
- [43] E. Lewars and I. NetLibrary, Computational chemistry introduction to the theory and applications of molecular and quantum mechanics.
- [44] G. Tomba *et al.*, J.Phys.Chem.B submitted .
- [45] D. Pearlman *et al.*, Computer Physics Communications **91**, (1995).
- [46] Y. Duan *et al.*, J. Comput. Chem. **24**, 1999 (2003).
- [47] J. Wang *et al.*, J. Comput. Chem. **25**, 1157 (2004).
- [48] B. M. Rode *et al.*, Theoretical Chemistry Accounts **115**, 77 (2006), 1432-881X.
- [49] H. Hellmann, *Einführung in die Quantenchemie* (Deuticke, Leipzig, 1937).
- [50] R. P. Feynman, Phys. Rev. **56**, 340 (1939).
- [51] L. Bürgi, Ph.D. thesis, EPF Lausanne, 1999.
- [52] E. M. Marti, S. M. Barlow, S. Haq, and R. Raval, Surface Science **501**, 191 (2002), 0039-6028.

- [53] S. Olsztynska, M. Komorowska, L. Vrielynck, and N. Dupuy, *Applied Spectroscopy* **55**, 901 (2001).
- [54] Y. Inomata, T. Inomata, T. Moriwaki, and J. L. Walter, *Spectrochimica Acta* **29**, 1933 (1973).
- [55] R. Mahalakshmi, S. X. Jesuraja, and S. J. Das, *Crystal Research And Technology* **41**, 780 (2006), 0232-1300.
- [56] B. J. M. Rajkumar and V. Ramakrishnan, *Spectrochimica Acta A* **58**, 1923 (2002).
- [57] X. Cao and G. Fischer, *Journal Of Molecular Structure* **519**, 153 (2000), 0022-2860.
- [58] N. Polfer *et al.*, *J Am Chem Soc* **128**, 517 (2006).
- [59] S. M. Barlow *et al.*, *Surface Science* **590**, 243 (2005), 0039-6028.
- [60] T. Genger, O. Hinrichsen, and M. Muhler, *Catalysis Letters* **59**, 137 (1999), 1011-372X.
- [61] M. Nyberg, M. Odellius, A. Nilsson, and L. G. M. Pettersson, *J. Chem. Phys.* **119**, 12577 (2003).
- [62] D. A. Case *et al.*, *AMBER 8*, 2004.
- [63] T. Steiner, *Angew. Chem. Int. Ed.* **41**, 48 (2002).
- [64] J. V. Barth, *Annual Review Of Physical Chemistry* **58**, 375 (2007), 0066-426X.
- [65] T. Classen, *PhD thesis Self-Organised Growth of Ordered Functional Nanostructures on Templates* (EPFL, Lausanne, 2006).
- [66] S. Sun and E. Bernstein, *Journal of Physical Chemistry* **100**, 13348 (1996).
- [67] E. Fischer, *Ber. Dtsch. Chem. Ges.* **27**, 2985 (1894).
- [68] L. Pauling, *Chem. Ind. (Suppl.)* **1**, 1 (1948).

- [69] J. Haldane, *Enzymes* (Longmans Green & Co. Ltd., Great Britain, 1930, reprinted by MIT press, Cambridge, 1965).
- [70] L. Pauling, *Nature* **248**, 769 (1974).
- [71] D. E. Koshland, *Proceedings Of The National Academy Of Sciences Of The United States Of America* **44**, 98 (1958).
- [72] T. J. L. . S. L. Berg, J. M., *Biochemistry*, 5th ed. (W.H. Freeman, New York, 2002).
- [73] T. Kirchhausen, *Nature Reviews Molecular Cell Biology* **1**, 187 (2000), 1471-0072.
- [74] M. Reches and E. Gazit, *Science* **300**, 625 (2003).
- [75] F. Rosei *et al.*, *Progr. Surf. Sci.* **71**, 95 (2003).
- [76] H. B. Fang, L. C. Giancarlo, and G. W. Flynn, *Journal of Physical Chemistry B* **102**, 7311 (1998).
- [77] G. P. Lopinski, D. J. Moffatt, D. D. Wayner, and R. A. Wolkow, *Nature* **392**, 909 (1998).
- [78] J. Kuntze, X. Ge, and R. Berndt, *Nanotechnology* **15**, S337 (2004), sp. Iss. SI.
- [79] F. Vonau *et al.*, *Physical Review Letters* **94**, (2005), 066103.
- [80] M. Boehringer *et al.*, *Phys. Rev. Lett.* **83**, 324 (1999).
- [81] M. Boehringer, K. Morgenstern, W. D. Schneider, and R. Berndt, *Angewandte Chemie, International Edition in English* **38**, 821 (1999).
- [82] J. Weckesser *et al.*, *Phys. Rev. Lett.* **87**, 096101 (2001).
- [83] I. Stensgaard, *Surface Science* **545**, L747 (2003).
- [84] S. M. Barlow, S. Haq, and R. Raval, *Langmuir* **17**, 3292 (2001).
- [85] M. E. Canas-Ventura *et al.*, *Journal Of Chemical Physics* **125**, (2006), 0021-9606 184710.

- [86] D. Kafer, L. Ruppel, G. Witte, and C. Woll, Physical Review Letters **95**, (2005), 0031-9007 166602.
- [87] F. Klappenberger *et al.*, Chem. Phys. Chem. **in press**, (2007).
- [88] D. A. Dougherty, Science **271**, 163 (1996).
- [89] J. Ireta, J. Neugebauer, and M. Scheffler, Journal Of Physical Chemistry A **108**, 5692 (2004), 1089-5639.
- [90] S. Weigelt *et al.*, Nature Materials **5**, 112 (2006), 1476-1122.
- [91] V. Sundaresan and R. Abrol, Chirality **17**, S30 (2005), suppl. S.
- [92] K. Harata, Chemical Reviews **98**, 1803 (1998).
- [93] M. Lingenfelder, G. Tomba, G. Costantini, and L. Colombi, Ang. Chem. **18**, 951 (2007).
- [94] N. Camillone, C. E. D. Chidsey, G. Y. Liu, and G. Scoles, Journal Of Chemical Physics **98**, 3503 (1993), 0021-9606.
- [95] D. J. Lavrich, S. M. Wetterer, S. L. Bernasek, and G. Scoles, Journal Of Physical Chemistry B **102**, 3456 (1998), 1089-5647.
- [96] J. Liang and G. Scoles, Langmuir **23**, 6142 (2007), 0743-7463.
- [97] R. M. Petoral, F. Bjorefors, and K. Uvdal, Journal Of Physical Chemistry B **110**, 23410 (2006), 1520-6106.
- [98] R. Petoral and K. Uvdal, J. Electron Spectrosc. Relat. Phenom. **128**, 159 (2003).
- [99] J. F. Cardenas and G. Grobner, Journal Of Electron Spectroscopy And Related Phenomena **152**, 87 (2006), 0368-2048.
- [100] M. Furukawa *et al.*, Surface Science **532**, 261 (2003), 0039-6028.
- [101] G. Gonella *et al.*, Journal Of Physical Chemistry B **109**, 18003 (2005), 1520-6106.
- [102] A. Cossaro *et al.*, Langmuir **22**, 11193 (2006), 0743-7463.

- [103] J. Hasselstrom *et al.*, Surface Science **407**, 221 (1998), 0039-6028.
- [104] X. Y. Zhao and J. Rodriguez, Surface Science **600**, 2113 (2006), 0039-6028.
- [105] O. Cavalleri *et al.*, Physical Chemistry Chemical Physics **6**, 4042 (2004), 1463-9076.
- [106] Y. Zubavichus *et al.*, Journal Of Physical Chemistry A **108**, 4557 (2004), 1089-5639.
- [107] S. Stepanow *et al.*, Journal Of Physical Chemistry B **108**, 19392 (2004).
- [108] P. Lofgren, A. Krozer, J. Lausmaa, and B. Kasemo, Surface Science **370**, 277 (1997), 0039-6028.
- [109] S. Tait, private communication, 2007.
- [110] S. Gilead and E. Gazit, Supramolecular Chemistry **17**, 87 (2005), 1061-0278.
- [111] S. Stepanow *et al.*, Nat. Mater. **3**, 229 (2004).
- [112] S. Stepanow, N. Lin, J. Barth, and K. Kern, *subm.* (2005).

Supporting Information

Video Legends

Video V1. DFT simulation showing the spontaneous proton transfer between the carboxyl and the amino groups of adsorbed Phe-Phe.

[<www.fkf.mpg.de/kern/videos/videoV1.mpg>](http://www.fkf.mpg.de/kern/videos/videoV1.mpg)

Video V2. Formation of a homochiral pair. STM movie showing the conformation and orientation changes that two adsorbed D-Phe-D-Phe molecules undergo while they approach and attempt to assemble.

[<www.fkf.mpg.de/kern/videos/videoV2.AVI>](http://www.fkf.mpg.de/kern/videos/videoV2.AVI)

Video V3. Formation of a heterochiral pair. STM movie showing the conformation and orientation changes that one adsorbed D-Phe-D-Phe and one adsorbed L-Phe-L-Phe molecules undergo while they approach and attempt to assemble.

[<www.fkf.mpg.de/kern/videos/videoV3.AVI>](http://www.fkf.mpg.de/kern/videos/videoV3.AVI)

Video V4. Formation of a homochiral trimer. STM movie showing the disruptions events that an initial pair of D-Phe-D-Phe molecules undergoes when a third molecule approaches the structure.

[<www.fkf.mpg.de/kern/videos/videoV4.AVI>](http://www.fkf.mpg.de/kern/videos/videoV4.AVI)

Video V5. Formation of a homochiral tetramer. STM movie showing the disruptions events that an initial trimer of D-Phe-D-Phe molecules undergoes when a fourth molecule approaches the structure.

[<www.fkf.mpg.de/kern/videos/videoV5.AVI>](http://www.fkf.mpg.de/kern/videos/videoV5.AVI)

Publications

N. Lin, A. Dmitriev, H. Spillmann, P. Messina, M. Lingenfelder, S. Stepanow, J.V. Barth, and K. Kern, "Supramolecular engineering of metal-organic networks at surfaces", AIP Conference Proceedings 696, **144** (2003).

M. Lingenfelder, H. Spillmann, A. Dmitriev, S. Stepanow, N. Lin, J.V. Barth, and K. Kern, "Towards surface-supported supramolecular architectures: Tailored coordination assembly of 1,4-benzenedicarboxylate and Fe on Cu(100)", Chem. Eur. J. **10**, 1913 (2004).

S. Stepanow, M. Lingenfelder, A. Dmitriev, N. Lin, T. Strunskus, C. Wöll, J.V. Barth, and K. Kern, "Bottom-up nanotechnology: Molecular engineering at surfaces", BESSY - Highlights 2003, 20 (2004).

S. Stepanow, M. Lingenfelder, A. Dmitriev, H. Spillmann, E. Delvigne, N. Lin, X. Deng, C. Cai, J.V. Barth, and K. Kern, "Steering molecular organization and host-guest interactions using two-dimensional nanoporous coordination systems", Nature Materials **3**, 229 (2004).

S. Stepanow, T. Strunskus, M. Lingenfelder, A. Dmitriev, H. Spillmann, N. Lin, J.V. Barth, and K. Kern, "Deprotonation-driven phase transformation in terephthalic acid self-assembly on Cu(100)", J. Phys. Chem. B **108**, 19392 (2004).

A. Dmitriev, H. Spillmann, M. Lingenfelder, N. Lin, J.V. Barth, and K. Kern, "Design of extended surface-supported chiral metal-organic arrays comprising mononuclear iron centers", Langmuir **20**, 4799 (2004).

A.P. Seitsonen, M. Lingenfelder, H. Spillmann, A. Dmitriev, S. Stepanow, N. Lin, K. Kern, and J.V. Barth, "Density functional theory analysis of carboxylate-bridged di-iron units in two-dimensional metal organic grids", J. Am. Chem. Soc. **128**, 5634 (2006).

A. Dmitriev, H. Spillmann, S. Stepanow, T. Strunskus, C. Wöll, A.P. Seitsonen, M. Lingenfelder, N. Lin, J.V. Barth, and K. Kern, "Asymmetry induction by cooperative intermolecular hydrogen bonds in surface-anchored layers of achiral molecules", Chem. Phys. Chem. **7**, 2197 (2006).

M. Lingenfelder, G. Tomba, G. Costantini, L. Colombi Ciacchi, A. De Vita, and K. Kern, "Tracking the chiral recognition of adsorbed dipeptides at the single molecule level", Angew. Chem. Int. Ed. **18**, 951 (2007).

P. Gambardella, S. Stepanow, A. Dmitriev, S. Sen Gupta, J. Honolka, S. Clair, S. Pons, M. Lingenfelder, P. Bencok, S. Stanescu, D.D. Sarma, N. Lin, H. Brune, J.V. Barth, and K. Kern, "Electronic and magnetic properties of Fe centers in metallosupramolecular arrays on Cu(100)", *submitted* 2007.

T. Classen, M. Lingenfelder, Y. Wang, R. Chopra, C. Virojanadara, U. Starke, G. Costantini, G. Fratesi, S. Fabris, S. de Gironcoli, S. Baroni, S. Haq, R. Raval, and K. Kern, "Hydrogen and coordination bonding supramolecular structures of trimesic acid on Cu(110)", J. Phys. Chem. B, *accepted for publication*, 2007.

G. Tomba, M. Lingenfelder, G. Costantini, K. Kern, F. Klappenberger, J.V. Barth, L. Colombi Ciacchi, A. De Vita, "Structure and energetics of diphenylalanine selfassembling on Cu(110)", J. Phys. Chem. B, *accepted for publication*, 2007.

Y. Wang, M. Lingenfelder, T. Classen, G. Costantini, and K. Kern, "Ordering of dipeptide chains on Cu surfaces through 2D co-crystallization", *submitted* 2007.

M. Lingenfelder, G. Tomba, S. Haq, G. Costantini, Y. Wang, R. Raval,

A. De Vita and K. Kern, "Tuning the expression of supramolecular chirality by molecular footprint engineering on metal surfaces", *in preparation*.

T. Classen, M. Lingenfelder, S. Stepanow, G. Costantini, N. Lin, and K. Kern, "Chiral chains of Phe-Phe on Cu (110) and Cu(100)", *in preparation*.

M. Lingenfelder, Y. Wang, T. Classen, G. Costantini and K. Kern, "Chiral cavities for heterogeneous asymmetric reactions", *in preparation*.

M. Lingenfelder, G. Tomba, Y. Wang, T. Classen, G. Costantini, A. De Vita and K. Kern, "Supramolecular organization of Phe-Phe on Cu(110)", *in preparation*.

Y. Wang, M. Lingenfelder, T. Classen, G. Costantini, and K. Kern, "An achiral organic catalyst for a chiral peptidic assembly: The role of terephthalic acid in Phe-Phe deprotonation reactions", *in preparation*.

PeRSoNaL NoTES

A PhD is only possible by the work of many people and the support and understanding of many others. I would like to express my gratitude in first place to the person who has contributed the most to this thesis, my thesis director, Professor Klaus Kern, for his expert guidance, for always having key ideas for improving our research and for his support during this time. Wherever I will go in the future, I will miss the nice atmosphere we have in our group. Thank you all for that!

I would also like to thank Prof. R. Schaller, Prof. H. Vogel, Prof. H. Zandvliet and Prof. I. Pascual. I really appreciate that you have taken the time to be part of the jury. Thanks a lot!

I cannot do other than say thank you! right now! to the people that are here after a whole night in the institute helping me to finish this thesis: Eduardo, Liza and Robin.

I have no enough words to express my gratitude to Eduardo, Alicia and Noelia, they have been my guardian angels during the most difficult times. This work is dedicated to you three, because without your love and support it would have never been possible.

Giovanni, my supervisor and my Italian *uncle*: thank you for your advice and the time you have spend talking with me, standing how *testarda* I am, teaching me the important words in *lombardo* and having fun by reading this thesis :o)...

My thanks to Prof. A. De Vita for starting a collaboration also with Giulia and Lucio, who privileged me with a wonderful mixture of pro-

fessional competence and nice friendship. I have to say that this is not actually *my* thesis but *our* thesis, Giulia! working with you and having your friendship is an invaluable gift.

My friends in the lab: Thomas Classen, for this extraordinary pedagogic competence to teach this chemist that not all the screw-shaped objects are phenyl rings :o). Yeliang Wang, for his enthusiasm, his companionship and support! and Sebastian for his great collaboration in many projects.

I also acknowledge Nian Lin, Hannes Spillmann and Sascha Dmitriev for introducing me to the magic world of STM. Your enthusiasm and your way of searching for the *beauty* in science resulted in extraordinary help for my formation.

Our wonderful secretary Sabine, for all the instances in which her assistance helped me along the way! I am also extremely thankful to Frau King. I do not know people more efficient and kind than Sabine and Frau King! Vielen Dank!

Dr. Sam Haq and Professor Rasmita Raval for giving me the possibility to perform LEED, RAIRS and TPD measurements in their lab at Liverpool, UK. I thank Sam for the extremely fruitful discussions, for correcting my thesis, for his always friendly way to help all the students. How much I have learned from you in only a couple of weeks!

I acknowledge Dr. Thomas Strunskus and Prof. Christof Wöll from the Ruhr-Universität Bochum, for the possibility to acquire NEXAFS and XPS data at the HE-SGM beamline at BESSY

II in Berlin.

Gracias to Steve Tait for helping me to interpret the TPD data and for many fruitful discussions. It is nice to have you in our office!

And now my genuine acknowledgment to the *cronopios*...

Ahora pasa que las tortugas son grandes admiradoras de la velocidad, como es natural. Las esperanzas lo saben, y no se preocupan. Los famas lo saben, y se burlan. Los cronopios lo saben, y cada vez que encuentran una tortuga, sacan la caja de tizas de colores y sobre la redonda pizarra de la tortuga dibujan una golondrina.

Julio Cortázar, *Historias de cronopios y de famas*.

My friends that can *draw swallows upon the turtle's round blackboard* : Kannan (*you have been my brother since my first day in Germany, I would need thousands of pages just to acknowledge you!*) Esther, Alena, Gaspar,

Pepe, Marcos, Jorge (*y por regalarme un refugio lleno de soles cuando no había luz al otro lado del mundo*), Ajo, Dimas, Silvina (*por tantas cosas, sobretudo por tu cariño y apoyo*), David (*por Marie Uguay and for helping me when I am lost in translation*), Alberto, Irene, Jan, Marina, Milan, Paola, Lucia, Violetta, Andrés, Orencio, Andrea (*por enseñarme tantos colores de la amistad*) and Sol, for sharing with me so many nice moments!

Claudio, because there is no thing on earth terrible enough for you not to be able to make me smile. Qué lindo es tenerte, compañero!

Maxor, por llevarme *a jugar a tirarle pedazos de pan a los patos desde el puente* ...

To my family: a mi padre por tantas horas de asesoramiento espiritual y también gráfico, a enfermeraaaaaaa! mi hermana preferida y la mejor cineasta del planeta, a mamá chanelini por regalarme una mirada alegre y luminosa sobre todas las cosas: tus máximas guían mi camino y me abrigan el corazón. Gracias por dejar su mano siempre cerca de la mía.

Curriculum vitae

Name: Magalí A. Lingenfelder
Date of Birth: March 25, 1980
Nationality: Argentine

Education

9/2007 Ph.D. Thesis, EPF Laussane: *Chiral Recognition and Supramolecular Self-Assembly of Adsorbed Amino Acids and Dipeptides at the Submolecular Level.*

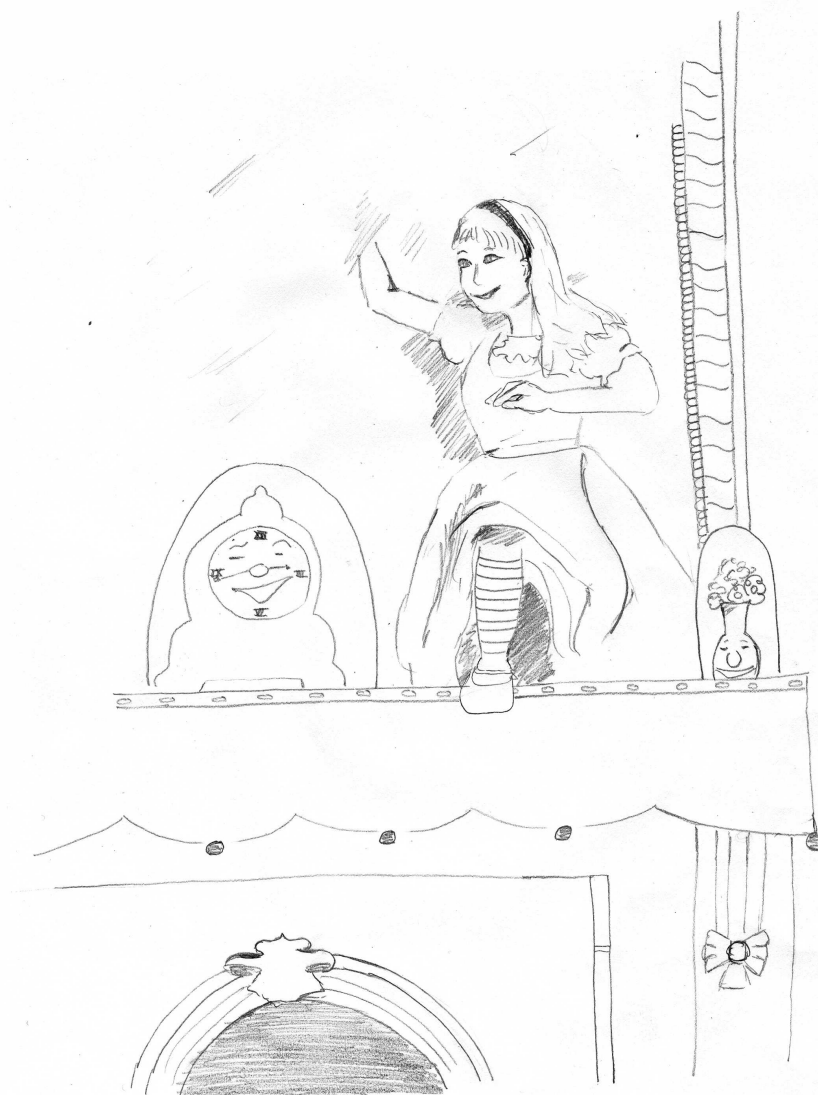
2004–2007 Research Assistant in the group of Prof Dr K. Kern at the Max-Planck-Institute for Solid State Research in Stuttgart, Germany.

2003 Diploma Thesis in the group of Prof Dr K. Kern at the Max-Planck-Institute for Solid State Research in Stuttgart, Germany: *Supramolecular Design of Metal Organic Coordination Systems at Metal Surfaces.*

1998–2003 Diploma studies in Chemistry, Licenciatura en Química, Universidad Nacional de Córdoba, Córdoba, Argentina.

1993–1997 High School at the Escuela Nacional Superior Arturo Capdevila, La Falda, Córdoba, Argentina.

Hope you have enjoyed this trip through the Looking glass...



Illustrations by Alicia Forment Piliaga